PLATELETS, CYTOKINES, AND PROANGIOGENIC FACTORS IN THE MAINTENANCE OF VESSEL INTEGRITY

by

Dallas Shujing Shi

A dissertation submitted to the faculty of
The University of Utah
in partial fulfillment of the requirements for the degree of

Doctor of Philosophy

Department of Human Genetics

The University of Utah

August 2015

The University of Utah Graduate School

STATEMENT OF DISSERTATION APPROVAL

The dissertation of **Dallas Shujing Shi**

has been approved by the following supervisory committee members:

Dean Y. Li	, Chair	**4/8/15** Date Approved
Andrew Weyrich	, Co-Chair	**4/8/15** Date Approved
Charles Murtaugh	, Member	**4/27/15** Date Approved
Gabrielle Kardon	, Member	**4/27/15** Date Approved
Gillian Stanfield	, Member	**4/27/15** Date Approved
Jared Rutter	, Member	**4/27/15**

and by **Lynn Jorde** , Chair/Dean of

the Department/College/School of **Human Genetics**

and by David B. Kieda, Dean of The Graduate School.

ABSTRACT

Almost all vascular diseases are linked to an inflammatory milieu that produces a toxic brew of angiogenic and inflammatory cytokines, which distort tissue architecture and function. These cytokines are produced by a cohort of cells, including endothelial cells, which line blood vessels, and immune cells such as platelets, which are derived from megakaryocytes. Under nonpathological conditions, these cells help to maintain vessel integrity, but when activated by disease states they release cytokines to cause immediate, direct, and disruptive effects on the vascular barrier.

In this dissertation I present the results of studies that examine the molecular signaling required to produce one of these immune cells, the platelet, during vessel maintenance as well as examination of the pathological contribution of cytokines on another immune cell, the endothelial cell. I show that under nonpathological conditions, platelets are required for vessel homeostasis, and it is through inhibition of RhoA signaling by proteasomal degradation that platelets are formed. Under pathological conditions, I demonstrate that pro-inflammatory and proangiogenic cytokines signal through a small GTPase, ARF6, in endothelial cells, and that ARF6 is the proximal convergence point regulating downstream signaling leading to endothelial barrier disruption and vessel permeability. This reveals ARF6 as a therapeutic target in vascular diseases such as arthritis and diabetic retinopathy. These studies fundamentally inform a

mechanism for the genesis of platelets in maintenance of normal barrier function and establish a therapeutic target when vessel homeostasis is disrupted in endothelial cells.

TABLE OF CONTENTS

ABSTRACT iii

ACKNOWLEDGEMENTS vii

CHAPTERS

1. INTRODUCTION 1

    Introduction to Multiple Myeloma and Megakaryocyte Biology 1
    Introduction to VEGF and Receptor Tyrosine Kinase Signaling 3
    References 8

2. PROTEASOME FUNCTION IS REQUIRED FOR PROPLATELET FORMATION 13

    Introduction 14
    Results 14
    Discussion 17
    Materials and Methods 20
    References 22
    Supplementary Materials 24

3. INTERLEUKIN RECEPTOR ACTIVATES A MYD88-ARNO-ARF6 CASCADE TO DISRUPT VASCULAR STABILITY 47

    Introduction 48
    Results 48
    Discussion 50
    Materials and Methods 51
    References 51
    Supplementary Materials 52

4. TARGETING VEGFR ENDOCYTOSIS TO TREAT DIABETIC RETINOPATHY 77

    Introduction 78

Results....79
Discussion....83
Materials and Methods....85
References....91

5. CONCLUDING REMARKS....103

References....105

ACKNOWLEDGEMENTS

I am grateful to the many people who contributed to the success of the work described within this dissertation. This includes: Dean Li, Andrew Weyrich, Nyall London, Matthew Smith, Weiquan Zhu, Chadwick Davis, Jae Hyuk Yoo, Tara Meylenek, Kirk Thomas, Shannon Oldenberg, Jake Winters, Patrick Kamba, Martha Sola-Visnar, Robert Campbell, Jing Ling, Lise Sorenson, Jesse Rowley, Eric Curtis, and Walter Kahr.

CHAPTER 1

INTRODUCTION

This thesis is divided into two parts and because of that, I will be presenting two introductions to the give the reader a better understanding of the background and basis for my research. In this chapter, I will first go over some megakaryocyte and platelet biology. Then I will cover some insights on receptor endocytosis and signal amplification in VEGF signaling.

Introduction to Multiple Myeloma and Megakaryocyte Biology

Multiple myeloma is a cancer of the plasma cells in the bone marrow. Affecting 1 in 100,000 people per year, multiple myeloma can lead to renal failure, anemia, and bone damage[1,2]. Proteasome inhibition has become a first line treatment against multiple myeloma with drugs such as bortezomib inhibiting the proteasome to disrupt NF-κB signaling, leading to cancer cell death[3,4]. However, a dose limiting side-effect of proteasome inhibition is thrombocytopenia[5,6]. This suggests that a further understanding of the role of the proteasome in thrombopoiesis may lead to more efficient and less toxic treatment regimens for patients.

The primary role of megakaryocytes is to make platelets by extending long, branching, cytoplasmic processes, called proplatelets, into blood vessels[7,8]. Platelets aid

in hemostasis and contribute to the formation of blood clots[7]. While the mechanism of platelet production and destruction has been studied, very little is known about what initiates and regulates these processes[8]. Proteasome inhibitors like bortezomib can induce thrombocytopenia via two mechanisms: either through a decrease in platelet production or an increase in platelet destruction[9]. Since multiple myeloma patients on bortezomib experience a refractory spike in platelet counts when the drug is terminated, we hypothesized that bortezomib induces a decrease in platelet production because recovery from platelet destruction is more gradual[3].

Mechanistically, it is clear that proteasome inhibition prevents the degradation of IκB, a protein complex that holds NF-κB in the cytoplasm of cells[10]. This prevents the translocation of NF-κB into the cell nucleus and the activation of downstream transcription factors. In multiple myeloma, there is over-activation of NF-κB signaling and it has been show that a reduction of NF-κB signaling causes apoptosis. This is why proteasome inhibition is beneficial in multiple myeloma because it kills cancer cells by inhibiting degradation of IκB and thus, release and translocation of NF-κB into the nucleus[11]. It is also thought that bortezomib-induced thrombocytopenia is a side-effect of of NF-κB signaling inhibition[12]. However, there is no evidence supporting this hypothesis. Thus, we wished to delineate whether NF-κB signaling is involved in bortezomib-induced thrombocytopenia.

Since the proteasome is known to degrade numerous proteins, it is likely that NF-κB signaling may not be involved in thrombopoiesis at all. Very little is actually known about the specific functions of the proteasome pathway in megakaryocytes and platelets, but even if NF-κB signaling is not involved in bortezomib-induced thrombocytopenia, we

hoped to learn something new about thrombopoiesis by screening for other proteins that are regulated by the proteasome in megakaryocytes. These include pro-alphaIIbeta integrin and the thrombopoietin receptor c-Mpl, which have both been associated with thromobopoiesis in the literature and can be degraded by the proteasome[13,14].

In conjunction with our studies *in vitro*, we developed two megakaryocyte-specific *Psmc1* conditional knockout mice. *Psmc1* is necessary for 26S proteasome function and has been used to study the role of the proteasome in neurons[15]. We mated the *Psmc1* (*floxed/floxed*) mice with two megakarocyte cre drivers, an inducible *Pdgf-cre* and a noninducible *Pf4-cre*. Using these mice, we aimed to test the hypothesis that lack of proteasome function is sufficient to disrupt proplatelet formation. The results of our findings make up the next chapter of this thesis.

Introduction to VEGF and Receptor Tyrosine Kinase Signaling

The second part of my thesis (Chapters 3 and 4) focuses on endothelial cells, which line the blood vessel, and regulate the exchange between intravascular and extravascular compartments. Endothelial cells use tight cell-cell junctions made up of cadherins and catenins to maintain vascular stability and to limit vascular leak. In neovascular and inflammatory diseases like sepsis, influenza, and diabetic retinopathy, the endothelium is destabilized by proinflammatory and/or proangiogenic cues such as interleukin-1beta and vascular endothelial growth factor (VEGF) which signals for cadherin and catenin internalization.

VEGF is essential to the development and maintenance of the vascular endothelium[16]. VEGF binding to its receptor, Vascular Endothelial Growth Factor

Receptor 2 (VEGFR2), promotes endothelial cell growth and migration, which drives vessel development[17]. VEGFR2 is a receptor tyrosine kinase (RTK) that, upon ligand binding, dimerizes, trans-phosphorylates multiple intracellular residues[18], and triggers several downstream pathways including PKC-MARCKS and Raf1-MEK1-ERK [17,19,20]. Signal transduction by VEGFR and other RTKs is highly dependent on receptor internalization and intracellular trafficking, first elucidated to explain how the sis oncogene, encoding platelet-derived growth factor, transformed cells whilst continuous extracellular exposure of growth factors did not [21]. This understanding of internalization and trafficking as a component of growth factor signaling applied not only in patho-physiogical signaling seen in oncogenesis, but also in physiological signaling mediated by RTKs.

RTK signaling is complex, but here, I would like to give a brief overview of the nuances in signaling. Like most proteins, RTKs are synthesized in the endoplasmic reticulum, transported to the Golgi, and then delivered to the plasma membrane. Under homeostatic conditions, RTKs undergo a basal rate of endocytosis and recycling. The rate of constitutive internalization and recycling varies and is both receptor and cell type dependent. For example, for EGFR in carcinoma cells, turnover can take 24 hours while for VEGFR in retinal endothelial cells, turnover is typically less then 1 hour[22].

Ligand binding activates RTKs and eventually leads to the down-regulation of the receptor. It is well know that RTKs are activated by receptor dimerization, trans phosphorylation of multiple intracellular sites, and subsequent signaling to various pathways with the help of adaptor proteins which bind to phosphorylated RTKS as illustrated above in VEGF signaling. However, whether this signaling occurs at the cell

surface or inside the cell is debatable[23,24]. For instance, a pool of RTKs can be held immobile at the cell membrane inside microvilli or caveolae[25]. In EGFR signaling, such a pool can still signal but activation is dampened[26]. It is unclear whether this affect is true of all arms of EGFR signaling but this does suggests that internalization is involved in signaling amplification.

The historic view of RTK endocytosis is that it leads to signal attenuation. Though this is eventually true, a more nuanced understanding of receptor endocytosis has developed in the last decade. Internalized RTKs can activate pathways from endosomes, suggesting distinct signaling pathways exist that require RTK endocytosis[23]. This internalization may or may not be clathrin dependent but it seems that temporal and spatial relationships are key for signal amplification[27,28]. This could be because endosomes proved an attractive environment for facilitating protein-protein interactions and maintenance of signal complexes. This could also be because endosomes travel and can bring together the right adaptor proteins with the activated RTK. Either way, the kinetics and final destination of the RTK seem to be tightly regulated[29].

Besides amplifying signals, internalization of RTKs can lead to signal attenuation. For example, phosphatases on the endoplasmic reticulum can dephosphorylate and inactivate RTKs in late endosome compartments[30]. To focus more on VEGF signaling and specifically VEGFR2 (since not much is known about endocytosis of VEGFR1 and VEGFR3), I want to highlight that VEGF internalization can also lead to receptor dephosphorylation[17]. Yet, like with other RTKs, endocytosis of VEGFR2 seems to increase signaling too.

It is thought that a protein complex composed of ephrin-B2 (a co-receptor for

VEGFR2), Dab2, and Par-3 associates with activated VEGFR2 in clathrin-coated vesicles and that the formation of this complex signals for trafficking of the receptor to the early endosome (marked by Rab5). In the early endosome, VEGFR2 can signal to ERK1/2 and RAC1 which can be blocked by inhibiting trafficking of VEGFR2[31]. It is unknown what other proteins may be involved in this early trafficking step or how signaling is amplified later now. Thus, though we know endocytosis can increase signaling, the precise mechanism and details remain obscure.

Since we are interested in signal amplification, it came to our attention that receptor-coreceptor binding could regulate the strength of extracellular VEGF signals as well. For instance, knockdown of ephrinB2 decreases the level of VEGF-induced VEGFR2 phosphoralation at the 1175 site. This seems to also affect receptor endocytosis though it is unclear whether a decrease in phosphorylated VEGFR2 precedes this process[32,33].

More recent studies have highlighted the interaction between VEGFR2 and another co-receptor called Neuropilin 1 (NRP1)[34-36]. NRP1 is a 130-140 kDa glycoprotein that was first identified in the nervous system[37]. It is highly conserved and in the nervous system, it is localized on neurons to guide axon formation. In the vascular system NRP1 is expressed on small and large vessels but is not ubiquitous[38]. For example, NRP1 seems to be more common in blood islands, which are early vascular structures, and in arterioles[39]. Knockout of the cytoplasmic domain of NRP1 impairs VEGFR2, phosphorylation and VEGFR2/NRP1 complexes formed in trans inhibit the amount of VEGFR2 internalized[40,41]. NRP1 seems to be essential for vascular morphogenesis but how it guides vascular development is still not completely

understood.

Trafficking of proteins from the plasma membrane and within intracellular compartments is dominated by small GTPases, especially those of the Ras superfamily such as Rab and Arf[42,43]. These molecules are GDP/GTP binding proteins that are active when bound to GTP and inactive when bound to GDP. Studies in Saccharomyces cerevisiae have shown that sequential steps in trafficking, from the endoplasmic reticulum to the golgi to the plasma membrane are mediated by subfamilies of Rab proteins[44,45]. Our own work has defined a role for Arf6 in regulating trafficking of cadherins and catenins to and from the cell surface[46,47]. These insights led us to question whether Arf6 may be the critical player by which VEGFR2 controls its own receptor-coreceptor internalization and signal amplification.

Pharmaceutical targeting of RTKs has changed the landscape of cancer research[48]. Drugs like erlotinib and lapatinib are used to treat breast cancers by inhibiting epidermal growth factors receptors while bevacizumab and sunitinib are used to treat colon cancer by inhibiting VEGF-mediated signaling[49,50]. The discovery that VEGF levels are elevated in vascular eye diseases has also informed the use of anti-VEGF agents in a subset of eye diseases including age-related macular degeneration and diabetic retinopathy. So far, these anti-VEGF drugs focus on blocking ligand and receptor interactions at the cell surface (bevacizumab) or to poisoning RTK activity (sunitinib)[51]. Our elucidation of a mechanism by which VEGF regulates its receptor and co-receptor internalization to amplify signaling has the potential to build on this by offering a new strategy for interfering with RTK signaling through inhibiting receptor endocytosis.

References

1. Mitchell, R., Kumar V., Abbas A., Fausto. *Multiple Myeloma*, (Saunders, Philadelphia).

2. D, L. *Harrison's Principles of Internal Medicine (18th Ed.)*, (McGraw Hill Medical, 2012).

3. Adams, J.*, et al.* Proteasome inhibitors: a novel class of potent and effective antitumor agents. *Cancer research* **59**, 2615-2622 (1999).

4. Field-Smith, A., Morgan, G.J. & Davies, F.E. Bortezomib (Velcade™) in the Treatment of Multiple Myeloma. *Therapeutics and Clinical Risk Management* **2**, 271-279 (2006).

5. Richardson, P.G., Hideshima, T. & Anderson, K.C. Bortezomib (PS-341): a novel, first-in-class proteasome inhibitor for the treatment of multiple myeloma and other cancers. *Cancer control : journal of the Moffitt Cancer Center* **10**, 361-369 (2003).

6. Lonial, S.*, et al.* Risk factors and kinetics of thrombocytopenia associated with bortezomib for relapsed, refractory multiple myeloma. *Blood* **106**, 3777-3784 (2005).

7. Behnke, O. An electron microscope study of the megacaryocyte of the rat bone marrow. I. The development of the demarcation membrane system and the platelet surface coat. *Journal of ultrastructure research* **24**, 412-433 (1968).

8. Rowley, J.W.*, et al.* Genome-wide RNA-seq analysis of human and mouse platelet transcriptomes. *Blood* **118**, e101-111 (2011).

9. Kenney, B. & Stack, G. Drug-induced thrombocytopenia. *Archives of pathology & laboratory medicine* **133**, 309-314 (2009).

10. Moynagh, P.N. The NF-kappaB pathway. *Journal of cell science* **118**, 4589-4592 (2005).

11. Paramore, A. & Frantz, S. Bortezomib. *Nature reviews. Drug discovery* **2**, 611-612 (2003).

12. Demchenko, Y.N.*, et al.* Classical and/or alternative NF-κB pathway activation in multiple myeloma. *Blood* **115**, 3541-3552 (2010).

13. Mitchell, W.B., Li, J., French, D.L. & Coller, B.S. alphaIIbbeta3 biogenesis is controlled by engagement of alphaIIb in the calnexin cycle via the N15-linked glycan. *Blood* **107**, 2713-2719 (2006).

14. Saur, S.J., Sangkhae, V., Geddis, A.E., Kaushansky, K. & Hitchcock, I.S. Ubiquitination and degradation of the thrombopoietin receptor c-Mpl. *Blood* **115**, 1254-1263 (2010).

15. Rezvani, N.*, et al.* Heterozygosity for the proteasomal Psmc1 ATPase is insufficient to cause neuropathology in mouse brain, but causes cell cycle defects in mouse embryonic fibroblasts. *Neuroscience letters* **521**, 130-135 (2012).

16. Coultas, L., Chawengsaksophak, K. & Rossant, J. Endothelial cells and VEGF in vascular development. *Nature* **438**, 937-945 (2005).

17. Olsson, A.K., Dimberg, A., Kreuger, J. & Claesson-Welsh, L. VEGF receptor signalling - in control of vascular function. *Nature reviews. Molecular cell biology* **7**, 359-371 (2006).

18. Lemmon, M.A. & Schlessinger, J. Cell signaling by receptor tyrosine kinases. *Cell* **141**, 1117-1134 (2010).

19. Veikkola, T., Karkkainen, M., Claesson-Welsh, L. & Alitalo, K. Regulation of angiogenesis via vascular endothelial growth factor receptors. *Cancer research* **60**, 203-212 (2000).

20. Ferrara, N. Vascular endothelial growth factor: basic science and clinical progress. *Endocrine reviews* **25**, 581-611 (2004).

21. Keating, M.T. & Williams, L.T. Autocrine stimulation of intracellular PDGF receptors in v-sis-transformed cells. *Science* **239**, 914-916 (1988).

22. Nakayama, M.*, et al.* Spatial regulation of VEGF receptor endocytosis in angiogenesis. *Nature cell biology* **15**, 249-260 (2013).

23. Vieira, A.V., Lamaze, C. & Schmid, S.L. Control of EGF receptor signaling by clathrin-mediated endocytosis. *Science* **274**, 2086-2089 (1996).

24. Sousa, L.P.*, et al.* Suppression of EGFR endocytosis by dynamin depletion reveals that EGFR signaling occurs primarily at the plasma membrane. *Proceedings of the National Academy of Sciences of the United States of America* **109**, 4419-4424 (2012).

25. Hommelgaard, A.M., Lerdrup, M. & van Deurs, B. Association with Membrane Protrusions Makes ErbB2 an Internalization-resistant Receptor. *Molecular biology of the cell* **15**, 1557-1567 (2004).

26. Aguilar, R.C. & Wendland, B. Endocytosis of membrane receptors: two pathways are better than one. *Proceedings of the National Academy of Sciences of the United States of America* **102**, 2679-2680 (2005).

27. Gorden, P., Carpentier, J.L., Cohen, S. & Orci, L. Epidermal growth factor: morphological demonstration of binding, internalization, and lysosomal association in human fibroblasts. *Proceedings of the National Academy of Sciences of the United States of America* **75**, 5025-5029 (1978).

28. Beattie, E.C., Howe, C.L., Wilde, A., Brodsky, F.M. & Mobley, W.C. NGF signals through TrkA to increase clathrin at the plasma membrane and enhance clathrin-mediated membrane trafficking. *The Journal of neuroscience : the official journal of the Society for Neuroscience* **20**, 7325-7333 (2000).

29. Sorkin, A. & von Zastrow, M. Endocytosis and signalling: intertwining molecular networks. *Nature reviews. Molecular cell biology* **10**, 609-622 (2009).

30. Simons, M. An Inside View: VEGF Receptor Trafficking and Signaling. *Physiology (Bethesda, Md.)* **27**, 213-222 (2012).

31. Gaengel, K. & Betsholtz, C. Endocytosis regulates VEGF signalling during angiogenesis. *Nature cell biology* **15**, 233-235 (2013).

32. Wang, Y.*, et al.* Ephrin-B2 controls VEGF-induced angiogenesis and lymphangiogenesis. *Nature* **465**, 483-486 (2010).

33. Sawamiphak, S.*, et al.* Ephrin-B2 regulates VEGFR2 function in developmental and tumour angiogenesis. *Nature* **465**, 487-491 (2010).

34. Evans, I.M.*, et al.* Neuropilin-1 signaling through p130Cas tyrosine phosphorylation is essential for growth factor-dependent migration of glioma and endothelial cells. *Molecular and cellular biology* **31**, 1174-1185 (2011).

35. Beck, B.*, et al.* A vascular niche and a VEGF-Nrp1 loop regulate the initiation and stemness of skin tumours. *Nature* **478**, 399-403 (2011).

36. Herzog, B., Pellet-Many, C., Britton, G., Hartzoulakis, B. & Zachary, I.C. VEGF binding to NRP1 is essential for VEGF stimulation of endothelial cell migration, complex formation between NRP1 and VEGFR2, and signaling via FAK Tyr407 phosphorylation. *Molecular biology of the cell* **22**, 2766-2776 (2011).

37. Eickholt, B.J., Mackenzie, S.L., Graham, A., Walsh, F.S. & Doherty, P. Evidence for collapsin-1 functioning in the control of neural crest migration in both trunk and hindbrain regions. *Development (Cambridge, England)* **126**, 2181-2189 (1999).

38. Moyon, D., Pardanaud, L., Yuan, L., Breant, C. & Eichmann, A. Plasticity of endothelial cells during arterial-venous differentiation in the avian embryo. *Development (Cambridge, England)* **128**, 3359-3370 (2001).

39. Herzog, Y., Kalcheim, C., Kahane, N., Reshef, R. & Neufeld, G. Differential expression of neuropilin-1 and neuropilin-2 in arteries and veins. *Mechanisms of development* **109**, 115-119 (2001).

40. Lanahan, A.*, et al.* The neuropilin 1 cytoplasmic domain is required for VEGF-A-dependent arteriogenesis. *Developmental cell* **25**, 156-168 (2013).

41. Koch, S.*, et al.* NRP1 presented in trans to the endothelium arrests VEGFR2 endocytosis, preventing angiogenic signaling and tumor initiation. *Developmental cell* **28**, 633-646 (2014).

42. Molendijk, A.J., Ruperti, B. & Palme, K. Small GTPases in vesicle trafficking. *Current opinion in plant biology* **7**, 694-700 (2004).

43. Schweitzer, J.K., Sedgwick, A.E. & D'Souza-Schorey, C. ARF6-mediated endocytic recycling impacts cell movement, cell division and lipid homeostasis. *Seminars in cell & developmental biology* **22**, 39-47 (2011).

44. Nielsen, E., Cheung, A.Y. & Ueda, T. The regulatory RAB and ARF GTPases for vesicular trafficking. *Plant physiology* **147**, 1516-1526 (2008).

45. Sannerud, R.*, et al.* Rab1 defines a novel pathway connecting the pre-Golgi intermediate compartment with the cell periphery. *Molecular biology of the cell* **17**, 1514-1526 (2006).

46. Grossmann, A.H.*, et al.* The small GTPase ARF6 stimulates beta-catenin transcriptional activity during WNT5A-mediated melanoma invasion and metastasis. *Science signaling* **6**, ra14 (2013).

47. Zhu, W.*, et al.* Interleukin receptor activates a MYD88-ARNO-ARF6 cascade to disrupt vascular stability. *Nature* **492**, 252-255 (2012).

48. Brunelleschi, S., Penengo, L., Santoro, M.M. & Gaudino, G. Receptor tyrosine kinases as target for anti-cancer therapy. *Current pharmaceutical design* **8**, 1959-1972 (2002).

49. Flynn, J.F., Wong, C. & Wu, J.M. Anti-EGFR Therapy: Mechanism and Advances in Clinical Efficacy in Breast Cancer. *Journal of oncology* **2009**, 526963 (2009).

50. Ortega, J., Vigil, C.E. & Chodkiewicz, C. Current progress in targeted therapy for colorectal cancer. *Cancer control : journal of the Moffitt Cancer Center* **17**, 7-15 (2010).

51. Alfaro, C.*, et al.* Influence of bevacizumab, sunitinib and sorafenib as single agents or in combination on the inhibitory effects of VEGF on human dendritic

cell differentiation from monocytes. *British journal of cancer* **100**, 1111-1119 (2009).

CHAPTER 2

PROTEASOME FUNCTION IS REQUIRED FOR PROPLATELET FORMATION

The following chapter is a reprint of a manuscript published in Journal of Clinical Investigation. It was published September 2, 2014, volume 124 (9), pages 3757-66, doi: 10.1172/JCI75247. In addition to myself, the other authors were Matthew Smith, Robert Campbell, Patrick Zimmerman, Zechariah Franks, Bjorn Kraemer, Kellie Machlus, Jing Ling, Patrick Kamba, Hansjorg Schwertz, Jesse Rowley, Rodney Miles, Zhi-Jian Liu, Martha Sola-Visner, Joseph Italiano Jr., Hilary Christensen, Walter Kahr, Dean Li, and Andrew Weyrich. I participated in the design, execution, interpretation of data, and preparation of the manuscript.

The Journal of Clinical Investigation RESEARCH ARTICLE

Proteasome function is required for platelet production

Dallas S. Shi,[1,2,3] Matthew C.P. Smith,[1,3,4] Robert A. Campbell,[1] Patrick W. Zimmerman,[1] Zechariah B. Franks,[1] Bjorn F. Kraemer,[1] Kellie R. Machlus,[5,6] Jing Ling,[1] Patrick Kamba,[1] Hansjörg Schwertz,[1,7] Jesse W. Rowley,[1,3] Rodney R. Miles,[8] Zhi-Jian Liu,[6,9] Martha Sola-Visner,[6,9] Joseph E. Italiano Jr.,[5,6,10] Hilary Christensen,[11] Walter H.A. Kahr,[11,12] Dean Y. Li,[1,2,3,4,13] and Andrew S. Weyrich[1,3]

[1]The Molecular Medicine Program, [2]Department of Human Genetics, [3]Department of Internal Medicine, and [4]Department of Oncological Sciences, University of Utah, Salt Lake City, Utah, USA. [5]Division of Hematology, Department of Medicine, Brigham and Women's Hospital, Boston, Massachusetts, USA. [6]Harvard Medical School, Boston, Massachusetts, USA. [7]Department of Immunology and Transfusion Medicine, Ernst-Moritz-Arndt University of Greifswald, Greifswald, Germany. [8]Department of Pathology, University of Utah, Salt Lake City, Utah, USA. [9]Division of Newborn Medicine and [10]Vascular Biology Program, Department of Surgery, Children's Hospital, Boston, Massachusetts, USA. [11]Division of Haematology/Oncology, Program in Cell Biology, The Hospital for Sick Children, Toronto, Ontario, Canada. [12]Departments of Paediatrics and Biochemistry, University of Toronto, Toronto, Ontario, Canada. [13]Key Laboratory for Human Disease Gene Study of Sichuan Province, Institute of Laboratory Medicine, Sichuan Academy of Medical Sciences and Sichuan Provincial People's Hospital, Chengdu, Sichuan, People's Republic of China.

The proteasome inhibiter bortezomib has been successfully used to treat patients with relapsed multiple myeloma; however, many of these patients become thrombocytopenic, and it is not clear how the proteasome influences platelet production. Here we determined that pharmacologic inhibition of proteasome activity blocks proplatelet formation in human and mouse megakaryocytes. We also found that megakaryocytes isolated from mice deficient for PSMC1, an essential subunit of the 26S proteasome, fail to produce proplatelets. Consistent with decreased proplatelet formation, mice lacking PSMC1 in platelets (*Psmc1$^{fl/fl}$ Pf4-Cre* mice) exhibited severe thrombocytopenia and died shortly after birth. The failure to produce proplatelets in proteasome-inhibited megakaryocytes was due to upregulation and hyperactivation of the small GTPase, RhoA, rather than NF-κB, as has been previously suggested. Inhibition of RhoA or its downstream target, Rho-associated protein kinase (ROCK), restored megakaryocyte proplatelet formation in the setting of proteasome inhibition in vitro. Similarly, fasudil, a ROCK inhibitor used clinically to treat cerebral vasospasm, restored platelet counts in adult mice that were made thrombocytopenic by tamoxifen-induced suppression of proteasome activity in megakaryocytes and platelets (*Psmc1$^{fl/fl}$ Pdgf-Cre-ER* mice). These results indicate that proteasome function is critical for thrombopoiesis, and suggest inhibition of RhoA signaling as a potential strategy to treat thrombocytopenia in bortezomib-treated multiple myeloma patients.

Introduction

Thrombocytopenia (low platelet count) is observed in numerous diseases and can be life threatening due to bleeding complications. Bortezomib, a reversible chemotherapeutic inhibitor used to treat patients with relapsed multiple myeloma, often induces thrombocytopenia within a few days of therapy initiation (1–3). Bortezomib-induced thrombocytopenia is dose-limiting, and if severe, bortezomib is withheld (2, 3). Although the mechanisms by which bortezomib induces thrombocytopenia is not clear, its primary mode of action is inhibition of the proteasome. The clinical observation that platelet counts rise above pretherapy levels upon cessation of bortezomib treatment suggests that bortezomib affects thrombopoiesis (1, 3).

Like other cells, megakaryocytes and anucleate platelets possess proteasome activity (4, 5). While the specific functions of the proteasome in platelet precursors (e.g., megakaryocytes) is relatively unknown (6), there is evidence that bortezomib alters the function of platelets (7–11). It has also been hypothesized, but not proven, that bortezomib inhibits megakaryocyte development via nuclear factor κB (NF-κB) (12). The aim of the present work was to precisely define the roles of the proteasome in thrombopoiesis and, in doing so, determine whether bortezomib-induced thrombocytopenia can be reversed. Using a combination of pharmacologic and genetic tools, we showed that inhibition of proteasome activity in megakaryocytes blocks proplatelet formation. In addition, conditional deletion of proteasome activity in mouse megakaryocytes led to severe thrombocytopenia and postnatal death. Decreased thrombopoiesis in proteasome-inhibited mice was caused by accumulation and increased activity of RhoA, and inhibitors of the RhoA signaling pathway restored platelet production. These findings demonstrated that the megakaryocyte proteasome controls the final stages of platelet production and also provided a potential option for restoring platelet counts in thrombocytopenic patients treated with bortezomib.

Results

Pharmacologic inhibition of the proteasome blocks platelet production. Due to its thrombocytopenic side effects, bortezomib is typically administered as a bolus twice weekly for 2 weeks (days 1, 4, 8, and 11), followed by a 10-day rest period (3). To ascertain the immediate effects of this inhibitor on platelets, mice were administered a clinically relevant dose (2 mg/kg body weight) of bortezomib, and platelet counts and proteasome activity were measured. Consistent with its well-known effect on platelet counts in patients, bortezomib induced a mild thrombocytopenia within 24 hours of

Authorship note: Dallas S. Shi and Matthew C.P. Smith contributed equally to this work.
Conflict of interest: The authors have declared that no conflict of interest exists.
Submitted: January 17, 2014; **Accepted:** June 5, 2014.
Reference information: *J Clin Invest.* 2014;124(9):3757–3766. doi:10.1172/JCI75247.

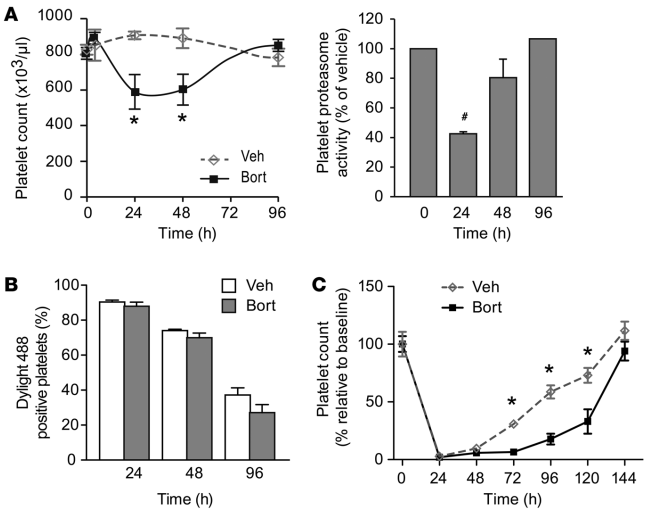

Figure 1. Pharmacologic inhibition of the proteasome induces thrombocytopenia in mice by decreasing platelet production. (**A**) Mice were treated with a bolus of bortezomib (Bort) or vehicle (Veh), and platelet counts and platelet proteasome activity were measured at the indicated times. Data are mean ± SEM of 6 experiments. (**B**) Mouse platelets were labeled in vivo with Dylight 488, as described in Methods. In parallel, the mice were treated with a bolus of bortezomib or vehicle, and the percentage of labeled platelets was determined at 24, 48, and 96 hours after treatment. Data are mean ± SEM of 6 independent experiments. (**C**) Mouse platelets were depleted in the presence of bortezomib or its vehicle, as described in Methods. The percentage of platelets relative to baseline control (0 hours) is shown. Data are mean ± SEM of 5 independent experiments. Note that **A**–**C** are derived from separate experiments. $^{*}P < 0.05$ vs. vehicle; $^{\#}P < 0.05$ vs. 0 hours.

treatment (Figure 1A). The thrombocytopenia was transient and temporally correlated with inhibition of proteasome activity in circulating platelets (Figure 1A).

To assess whether bortezomib-induced thrombocytopenia was due to accelerated clearance, we injected Dylight 488 conjugated to GPIBβ into the bloodstream to track the lifespan of platelets in vivo in the presence of bortezomib or its vehicle. As expected, the number of labeled platelets decreased over 96 hours as platelets were cleared from the circulation (13). However, the number of labeled platelets was similar between bortezomib and vehicle treatment groups at every time point tested (Figure 1B). This suggested that bortezomib did not induce platelet activation in the bloodstream, which would facilitate platelet clearance. Consistent with this notion, we found that bortezomib did not directly induce activation of integrin $\alpha_{IIb}\beta_3$ (Supplemental Figure 1; supplemental material available online with this article; doi:10.1172/JCI75247DS1), nor did it alter agonist-induced activation of integrin $\alpha_{IIb}\beta_3$ or surface expression of P-selectin in mouse platelets (Supplemental Figures 1 and 2). Similarly, bortezomib did not influence PAC-1 binding to human platelets in the presence or absence of agonist stimulation (Supplemental Figure 3 and data not shown).

Since acute administration of bortezomib did not shorten the lifespan of circulating platelets, we hypothesized that the bortezomib-induced thrombocytopenia was due to a decrease in platelet production. To test this, we depleted platelets with an antibody against GPIBα and then treated mice with bortezomib or its vehicle to determine whether bortezomib prevented platelet counts from rebounding. Platelet counts rebounded at a slower pace with bortezomib treatment than with the vehicle control (Figure 1C).

The data in Figure 1 suggested that bortezomib-induced thrombocytopenia was due to a defect in the formation of platelets from megakaryocytes. To examine this further, we determined whether inhibition of the proteasome with bortezomib blocked proplatelet formation in murine megakaryocytes. Bortezomib significantly decreased proplatelet formation in fetal liver–derived megakaryocytes (Figure 2A). Similar responses were observed in human megakaryocytes, and removal of bortezomib from the incubation media restored proplatelet formation (Figure 2B and data not shown). To confirm that this effect was specific to proteasome inhibition, megakaryocytes were treated with MG132 or lactacystin. Both proteasome inhibitors phenocopied the effects of bortezomib (Supplemental Figure 4 and data not shown). The inability to form proplatelets was accompanied by a notable increase in cell spreading on immobilized fibrinogen (Figure 2B), which indicates that the proteasome regulates key cytoskeletal proteins in megakaryocytes.

Phenotypic consequences of proteasome inhibition are independent of NF-κB and integrin α_{IIb}. Bortezomib's antitumor activity in multiple myeloma has been attributed to inhibition of NF-κB in plasma cells (14). Therefore, others have speculated that proteasome inhibitors may induce thrombocytopenia via the NF-κB signaling pathway (12). To test this hypothesis, we first treated megakaryocytes with bortezomib and examined the expression of nuclear factor of κ light polypeptide gene enhancer in B cells inhibitor, α (IκBα), which sequesters NF-κB in the cytoplasm until it is phosphorylated, ubiquitinated, and degraded (15). As expected, bortezomib increased the expression of IκBα in megakaryocytes (Figure 3A), which demonstrated that inhibition of the proteasome blocks the NF-κB signaling pathway. We also found that inhibition of IκB kinase with SC-514, which induces IκBα phosphorylation, increased IκBα protein levels in megakaryocytes (Figure 3A). However, unlike bortezomib, SC-514 did not halt proplatelet production (Figure 3B).

In addition to regulating NF-κB activity, Mitchell and colleagues previously demonstrated that the proteasome is capable of degrading pro–integrin α_{IIb} (5). Based on this published work, and our present finding that inhibition of the proteasome decreased

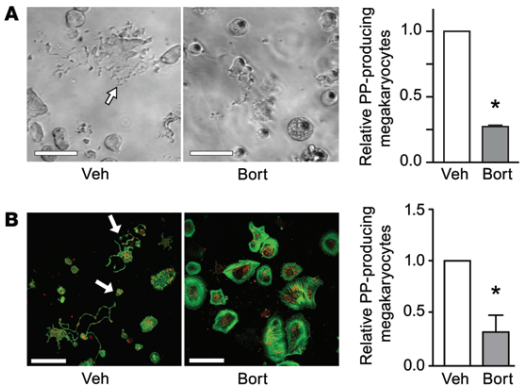

Figure 2. Pharmacologic inhibition of the proteasome blocks proplatelet formation in murine and human megakaryocytes. Mouse fetal liver–derived megakaryocytes (**A**) and human megakaryocytes (**B**) were pretreated with vehicle or bortezomib, and megakaryocytes producing proplatelets (PP) were examined. Shown are (**A**) representative transmission images and (**B**) representative confocal images with wheat germ agglutinin (WGA; red) and phalloidin (green) staining. Arrows denote proplatelet extensions. Also shown for each is the number of proplatelet-producing megakaryocytes relative to vehicle control. Data are mean ± SEM of 3 independent experiments. *$P < 0.05$ vs. vehicle. Scale bars: 100 μm (**A**); 50 μm (**B**).

the formation of proplatelets when megakaryocytes adhere to fibrinogen, we sought to determine whether bortezomib regulated the activity of integrin $\alpha_{IIb}\beta_3$ in megakaryocytes. Bortezomib did not alter the expression of mature integrin α_{IIb} protein, nor did it increase binding of soluble fibrinogen or PAC-1 to human megakaryocytes (Supplemental Figure 5 and data not shown). Bortezomib also had no effect on adherence of human megakaryocytes to fibrinogen (Supplemental Figure 6). Together, these data indicate that bortezomib does not directly block proplatelet formation through NF-κB– or integrin $\alpha_{IIb}\beta_3$–dependent mechanisms.

Phenotypic consequences of proteasome inhibition require RhoA. The changes in actin polymerization observed in megakaryocytes treated with proteasome inhibitors were reminiscent of cytoskeletal changes in endothelial cells that rely on the small GTPase RhoA (16). Indeed, we found that bortezomib increased total RhoA protein expression (Figure 4A). Bortezomib also increased RhoA-GTP activity and phosphorylation of myosin light chain (MLC) kinase, which is downstream of RhoA (Figure 4, A and B).

RhoA-dependent signaling has been linked to the production of proplatelets (17, 18). Therefore, we treated human megakaryocytes with Y27632, a selective inhibitor of the Rho-associated protein kinase p160ROCK, or with C3 transferase, a direct RhoA inhibitor. Y27632 and C3 transferase rescued proplatelet formation in bortezomib-treated cells (Figure 4C and Supplemental Figure 7). This response was likely due to inhibition of downstream RhoA effectors, because Y27632 decreased phosphorylation of MLC kinase in the presence of bortezomib (Figure 4B). In agreement with the rescue of proplatelet formation observed in bortezomib-treated human megakaryocytes, mouse megakaryocytes treated with bortezomib plus Y27632 or with bortezomib plus fasudil, a more clinically relevant p160ROCK inhibitor, formed proplatelets (Figure 4D). These results in mouse megakaryocytes were similar to a recent report by Murai et al. (19).

Genetic deletion of the proteasome results in severe thrombocytopenia and death. To further dissect the role of the proteasome in thrombopoiesis, we focused on protease (prosome, macropain) 26S subunit, ATPase 1 (*Psmc1*; gene ID 19179) in mouse megakaryocytes and platelets. *Psmc1* is an essential subunit of the 19S regulatory particle that is critical for ubiquitin-mediated protein degradation by the 26S proteasome complex (20–22). It is conserved at the protein level in human and mouse megakaryocytes (Supplemental Figure 8). mRNA for *Psmc1* was also expressed in both species, although human megakaryocytes had lower levels of the transcript compared with mouse megakaryocytes (Supplemental Table 1).

Psmc1$^{fl/fl}$ mice were crossed with platelet factor 4 *Cre* recombinase (*Pf4-Cre*) mice to disrupt proteasome activity in megakaryocytes and platelets. *Psmc1*$^{fl/fl}$ *Pf4-Cre* mice had significantly reduced protein for PSMC1 in megakaryocytes, but not other tissues (Supplemental Figure 9). Ubiquinated proteins also accumulated in megakaryocytes from *Psmc1*$^{fl/fl}$ *Pf4-Cre* mice (Supplemental Figure 10).

Despite a marked reduction in PSMC1 protein, the number of megakaryocytes from *Psmc1*$^{fl/fl}$ *Pf4-Cre* mice in bone marrow or spleen was not reduced compared with *Psmc1*$^{fl/wt}$ mice (Supplemental Figure 11). Unlike their littermate controls, however, *Psmc1*$^{fl/fl}$ *Pf4-Cre* mice had severe thrombocytopenia at postnatal day 1 (P1), and the majority of *Psmc1*$^{fl/fl}$ *Pf4-Cre* mice died before weaning (Figure 5, A and B). The reduction in platelet counts was more severe than in *c-Mpl* knockout pups at the same age (Supplemental Figure 12). In addition to reduced numbers of platelets, *Psmc1*$^{fl/fl}$ *Pf4-Cre* mice had lower hematocrits than *Psmc1*$^{fl/wt}$ mice, and bleeding was seen in the abdomen and limbs (Figure 5, C and D). Pathological signs of hemorrhage were also present in the bladder and testes of all animals and occasionally observed in the brain, lymph nodes, and intestines (Figure 5E and data not shown).

Ultrastructure examination of megakaryocytes from *Psmc1*$^{fl/fl}$ *Pf4-Cre* mice revealed less cytoplasm compared with megakaryocytes from *Psmc1*$^{fl/wt}$ mice (Figure 6A). In addition, *Psmc1*$^{fl/fl}$ *Pf4-Cre* megakaryocytes lacked demarcation membranes, which were readily visible in *Psmc1*$^{fl/wt}$ megakaryocytes (Figure 6A). Similar to mouse megakaryocytes treated with bortezomib (Figure 2A), megakaryocytes from *Psmc1*$^{fl/fl}$ *Pf4-Cre* mice failed to produce proplatelets (Figure 6B).

Inhibition of RhoA-dependent signaling prevents thrombocytopenia induced by genetic disruption of proteasome activity. As predicted from the pharmacological data, megakaryocytes from *Psmc1*$^{fl/fl}$ *Pf4-Cre* mice expressed higher levels of total RhoA protein and RhoA-GTP

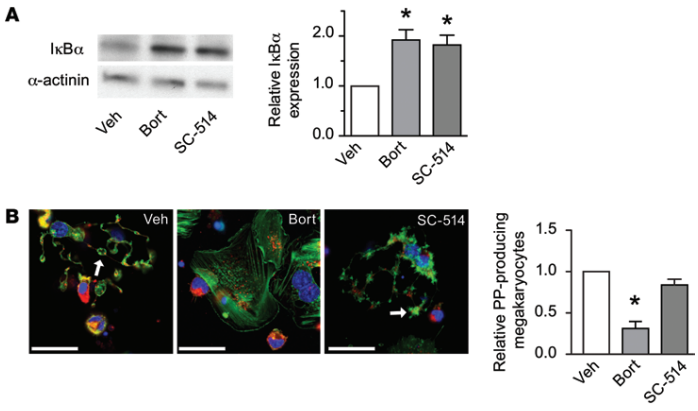

Figure 3. Proteasome-dependent formation of proplatelets in human megakaryocytes occurs independently of NF-κB. (**A**) Human megakaryocytes were treated with vehicle, bortezomib, or the NF-κB inhibitor SC-514. Shown are a representative Western blot for IκBα as well as IκBα expression levels, as measured by densitometry, relative to vehicle control. Data are mean ± SEM (n = 3). (**B**) Morphology of megakaryocytes treated with vehicle, bortezomib, or SC-514. Megakaryocytes were stained with WGA (red), phalloidin (green), and DAPI (blue). Arrows denote proplatelets. Images are representative of 3 independent experiments. Also shown is the number of proplatelet-producing megakaryocytes relative to vehicle control. Data are mean ± SEM of 3 independent experiments. Scale bars: 25 μm. *$P < 0.05$ vs. vehicle.

(Figure 7A). Fasudil also rescued proplatelet formation in bone marrow–derived megakaryocytes from *Psmc1*$^{fl/fl}$ *Pf4-Cre* mice (Figure 7B).

Next we generated inducible conditional knockouts by crossing *Psmc1*$^{fl/fl}$ mice with platelet-derived growth factor–*Cre* estrogen receptor (*Pdgf-Cre-ER*) mice, which allowed for time-restricted deletion of *Psmc1* in megakaryocytes and platelets after administration of the competitive estrogen receptor ligand tamoxifen. Although *Pdgf* is expressed by other cells besides megakaryocytes, *Pdgf-Cre-ER* mice were used because *Pf4-Cre-ER* mouse lines are not currently available. Like *Psmc1*$^{fl/fl}$ *Pf4-Cre* mice (Figure 5, A and B), administration of tamoxifen to *Psmc1*$^{fl/fl}$ *Pdgf-Cre-ER* mice at P1 resulted in thrombocytopenia and early postnatal mortality (Supplemental Figure 13, A and B). When tamoxifen was administered to adult *Psmc1*$^{fl/fl}$ *Pdgf-Cre-ER* mice, platelet counts were reduced by approximately 50% after 6 days compared with *Psmc1*$^{fl/wt}$ mice (Figure 8A). In the presence of fasudil, however, tamoxifen did not significantly decrease platelet counts in *Psmc1*$^{fl/fl}$ *Pdgf-Cre-ER* mice (Figure 8A). Consistent with these rescue experiments, staining of megakaryocytes in crude bone marrow showed that the in vivo fasudil treatment rescued proplatelet formation (Figure 8B). These results are consistent with our in vitro findings that fasudil maintained proplatelet formation in bortezomib-treated megakaryocytes (Figure 4D).

Discussion

In this study, we found that pharmacologic or genetic disruption of proteasome activity in megakaryocytes inhibits proplatelet formation. Pharmacologic inhibition was reversible in megakaryocytes treated in vitro with bortezomib, and thrombocytopenia was transient when bortezomib was administered as a bolus in vivo. When inhibition of proteasome activity was sustained, as was the case with genetic deletion of *Psmc1* in megakaryocytes and platelets, megakaryocytes did not form proplatelets, and *Psmc1*$^{fl/fl}$ *Pf4-Cre* mice had severe thrombocytopenia. Mice with genetic ablation of *Psmc1* in megakaryocytes and platelets also died shortly after birth. Taken together, these data provide compelling evidence that the proteasome is critically involved in thrombopoiesis. The data also offer a strong explanation as to why multiple myeloma patients require cyclic treatment regimes of bortezomib in order to tolerate the drug (3, 12).

Our findings provide definitive proof that the megakaryocyte proteasome is required for the final stages of platelet production. Evidence for this is 2-fold: first, pharmacologic inhibition of proteasome activity in late-stage human or mouse megakaryocytes significantly blunted proplatelet formation; and second, platelet production was significantly reduced in *Psmc1*$^{fl/fl}$ *Pf4-Cre* mice, in which genetic deletion of *Psmc1* does not occur until megakaryocytes express platelet factor 4, which activates the *Cre* recombinase (23). In addition to regulating thrombopoiesis, others have shown that the proteasome is important for the proliferation of megakaryocyte precursors (24) and the degradation of cyclin B and pro–integrin α_{IIb} in megakaryocytes (5, 25).

Like their parent megakaryocytes, anucleate platelets also possess proteasome activity (4, 10), and several groups have demonstrated that pharmacologic inhibition of the proteasome regulates platelet function (8–11, 26). Under the conditions of our experiments, bortezomib did not affect indices of platelet activation in mouse or human platelets that included activation of integrin $\alpha_{IIb}\beta_3$ and translocation of P-selectin to the surface of platelets. However, similar to Gupta and coworkers (8), we observed that bortezomib reduced the aggregation of human platelets when low concentrations of thrombin were used as the agonist (Supplemental Figure 14). Although more work is needed, results generated by multiple independent groups strongly indicate that protein degradation systems regulate platelet function (6).

Other groups have shown that pharmacologic inhibition regulates the function of platelets ex vivo (8–11, 26), but bortezomib did not accelerate the clearance of labeled platelets under the conditions of our present studies. Our results contrasted those of Nayak and colleagues (7), who showed that pharmacologic inhibition of the proteasome reduced the half-life of platelets in mice. One potential explanation for these discordant findings is that the bolus dose of bortezomib used in our studies only produced a mild thrombocytopenia and did not completely abolish platelet proteasome activity (Figure 1A). Although Nayak's group did not measure cellular proteasome activity (7), it is possible that they achieved more efficient pharmacologic inhibition of the proteasome in platelets and other vascular cells. Different routes of drug administra-

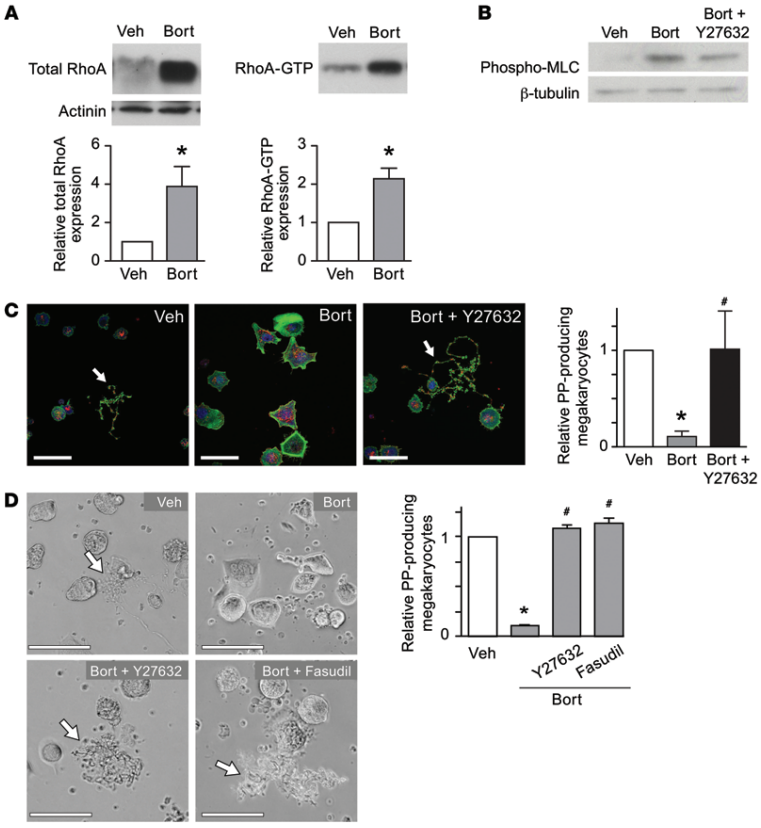

Figure 4. The proteasome regulates proplatelet formation through the RhoA signaling pathway. (**A**) Human megakaryocytes were treated with vehicle or bortezomib, and total RhoA and GTP-bound RhoA were measured. Shown are representative Western blots and expression of RhoA or RhoA-GTP, as measured by densitometry, relative to vehicle control. Data are mean ± SEM of 4 independent experiments. (**B** and **C**) Human megakaryocytes were treated with vehicle, bortezomib, or bortezomib plus Y27632. (**B**) Western blot for phospho-MLC. (**C**) Representative confocal images of human megakaryocytes stained with WGA (red) and phalloidin (green). Arrows denote proplatelets. Scale bar: 50 μm. Also shown is the number of proplatelet-producing megakaryocytes relative to vehicle control. Data are mean ± SEM of 3 independent experiments. (**D**) Representative transmission images of mouse bone marrow–derived megakaryocytes treated with vehicle, bortezomib, bortezomib plus Y27632, or bortezomib plus fasudil. Scale bar: 100 μm. Also shown is the number of proplatelet-producing megakaryocytes relative to vehicle control. Data are mean ± SEM of 3 independent experiments. $^{*}P < 0.05$ vs. vehicle; $^{\#}P < 0.05$ vs. bortezomib alone.

tion and types/concentrations of proteasome inhibitors between the studies may also explain the divergent results. Further studies are needed to resolve the in vivo pharmacology of proteasome inhibition and its relation to thrombocytopenia. However, our present studies clearly showed that platelet counts rebounded at a slower pace in mice subjected to platelet depletion in the presence of bortezomib. These data, in combination with the severe thrombocytopenia we observed in *Psmc1*$^{fl/fl}$ *Pf4-Cre* mice, demonstrated that the proteasome directly modulates platelet production.

We found that thrombocytopenia was more severe in *Psmc1*$^{fl/fl}$ *Pf4-Cre* mice compared with *c-Mpl* knockout mice (Supplemental Figure 12), which have normal life expectancies (27). Consistent with a marked reduction in platelet counts, *Psmc1*$^{fl/fl}$ *Pf4-Cre* mice had low hematocrits and hemorrhaging in the abdominal region. Occasional hemorrhaging was also observed in the brain, lymph nodes, and intestines. This suggests that severe thrombocytopenia is the primary driver of postnatal death in *Psmc1*$^{fl/fl}$ *Pf4-Cre* mice. Hemorrhaging in *Psmc1*$^{fl/fl}$ *Pf4-Cre* mice may occur because platelet numbers are simply too low to prevent bleeding. Alternatively, insufficient platelet counts in *Psmc1*$^{fl/fl}$ *Pf4-Cre* mice may result in abnormal vascular development or blood/lymphatic vessel separation, which could lead to excessive bleeding (28). In this regard, several groups have shown that platelet C-type lectin-like receptor 2 (CLEC-2) receptors regulate lymphatic vascular development, and, like *Psmc1*$^{fl/fl}$ *Pf4-Cre* mice (29–33), platelet-specific knockout of *CLEC-2* results in postnatal lethality (32). It should also be noted that a very low threshold of platelet function sufficiently maintains vascular function (27, 33, 34), raising the possibility that *Psmc1*$^{fl/fl}$ *Pf4-Cre* mice produce dysfunctional platelets that are incapable of maintaining vascular integrity. Indeed, recent studies have demonstrated that immune-type receptors in platelets are critical for the prevention of inflammation-induced hemorrhage (35). Thus, it is entirely possible that in addition to being reduced in number, platelets from *Psmc1*$^{fl/fl}$ *Pf4-Cre* mice express an abnormal repertoire of proteins resulting in platelet dysfunction.

Studies in megakaryocytes revealed that genetic or pharmacologic interruption of proteasome activity led to accumulation of IκBα and RhoA. Although both proteins were upregulated, we found that the final stages of proplatelet formation required RhoA signaling rather than inhibition of NF-κB, as previously suggested (12). The inability to sprout proplatelets resembled studies in neu-

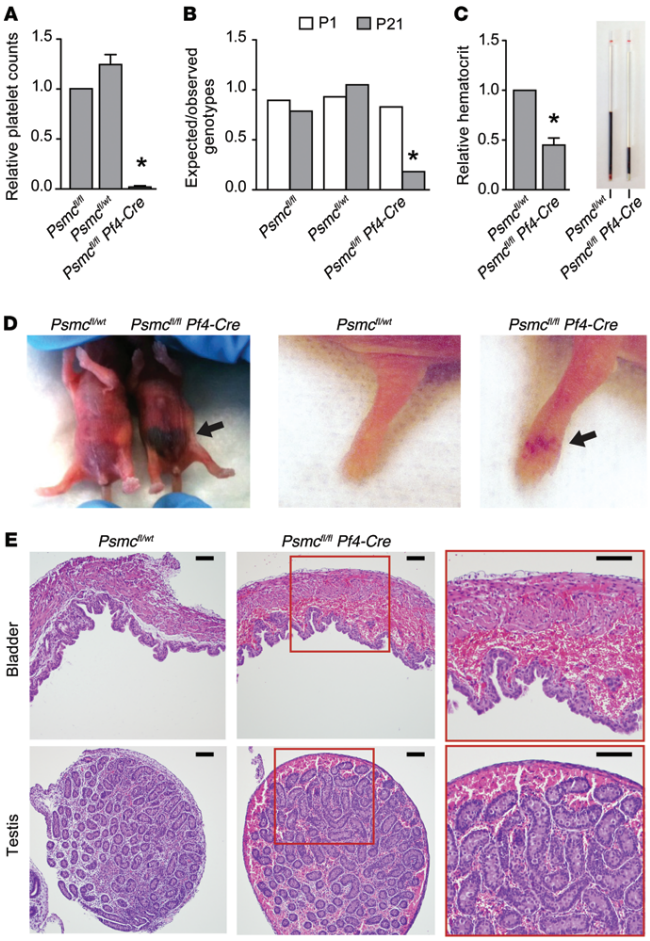

Figure 5. Genetic ablation of proteasome activity in megakaryocytes causes severe thrombocytopenia and postnatal death. (**A**) Platelet counts at P1 in *Psmc1*$^{fl/fl}$ *Pf4-Cre* and *Psmc1*$^{fl/wt}$ mice, expressed relative to *Psmc1*$^{fl/fl}$ mice. Bars show mean ± SEM of 6 independent experiments. *$P < 0.05$ vs. *Psmc1*$^{fl/fl}$. (**B**) Mortality rates in *Psmc1*$^{fl/fl}$, *Psmc1*$^{fl/wt}$, and *Psmc1*$^{fl/fl}$ *Pf4-Cre* mice at P1 and P21. Shown are ratios of expected versus observed genotypes, determined by χ^2 analysis, at P1 and P21 ($n = 88$). *$P < 0.05$ vs. P1, determined by χ^2 distribution table. (**C**) Hematocrits in *Psmc1*$^{fl/fl}$ *Pf4-Cre* relative to *Psmc1*$^{fl/wt}$ mice at P1. Data are mean ± SEM of 6 independent experiments. *$P < 0.05$ vs. *Psmc1*$^{fl/wt}$. (**D**) Left: Images of *Psmc1*$^{fl/wt}$ and *Psmc1*$^{fl/fl}$ *Pf4-Cre* mice at P1. Evidence of bleeding was observed in the abdominal region (arrow). Middle and right: Limbs of *Psmc1*$^{fl/wt}$ and *Psmc1*$^{fl/fl}$ *Pf4-Cre* mice. Hemorrhaging was observed in the limb of the *Psmc1*$^{fl/fl}$ *Pf4-Cre* mouse (arrow). (**E**) Whereas P1 histological sections of *Psmc1*$^{fl/wt}$ mice demonstrated normal histology, bleeding was observed in the bladder and testis of a *Psmc1*$^{fl/fl}$ *Pf4-Cre* mouse. Boxed regions are shown at higher magnification at right. Scale bars: 100 μm.

rons, in which acute inhibition of the proteasome blocks activity-dependent growth of new dendritic spines. It is not known what proteins are degraded by the proteasome in order to stimulate new spine growth; however, inactivation of RhoA leads to neurite outgrowth (36, 37). This suggests that, similar to megakaryocyte proplatelet formation, the proteasome may control neuronal outgrowth by degrading RhoA. Moreover, RhoA signaling has been shown to maintain normal megakaryocyte development, which is critical for platelet production (18).

Malfunction of the proteasome in human diseases may lead to aberrant platelet production or abnormal platelet generation. Disruption of proteasome activity could occur at multiple checkpoints, since human megakaryocytes expressed the full repertoire of proteasome components at the mRNA level (Supplemental Table 1). Identifying the complete portfolio of target proteins degraded by the proteasome in megakaryocytes will shed additional light on the mechanisms that control thrombopoiesis and the phenotype of platelets as they enter the circulation. Understanding the functions of the proteasome in platelets, which is active and capable of degrading proteins (7–9), also requires further investigation. From an immediate perspective, our present findings demonstrated that bortezomib directly inhibits proteasome activity in megakaryocytes and thereby decreases platelet production. Our findings also established fasudil as a potential treatment for preventing and/or reversing bortezomib-induced thrombocytopenia in multiple myeloma patients. Additionally, inhibitors of the RhoA signaling pathway may have efficacy in the treatment of other thrombocytopenic disorders caused by abnormal platelet production, especially if the disease is driven by proteasome-dependent mechanisms.

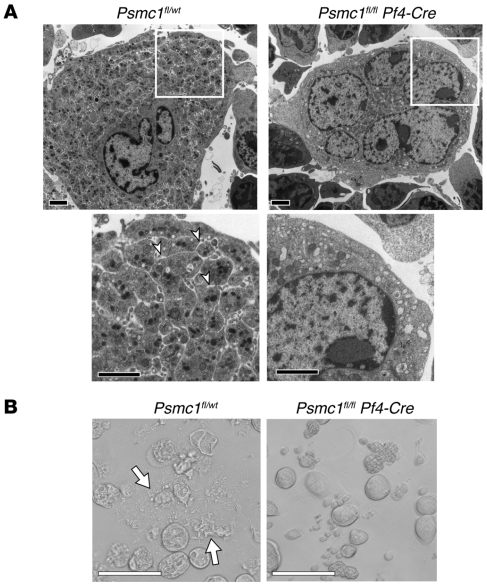

Figure 6. Platelet territories and proplatelets fail to form in PSMC1-deficient megakaryocytes. (**A**) Whereas *Psmc1*$^{fl/wt}$ mouse megakaryocytes showed a large cytoplasmic region compared with the nucleus, those from a *Psmc1*$^{fl/fl}$ *Pf4-Cre* mouse had less cytoplasm compared with the multilobed nucleus. Boxed regions are shown at higher magnification below, in which the demarcation membrane exhibited in the *Psmc1*$^{fl/wt}$ megakaryocytes (arrowheads) was not observed in the *Psmc1*$^{fl/fl}$ *Pf4-Cre* megakaryocyte. (**B**) Transmission images of megakaryocytes derived from *Psmc1*$^{fl/wt}$ and *Psmc1*$^{fl/fl}$ *Pf4-Cre* mice at P1. Proplatelet formation (arrows) was absent in *Psmc1*$^{fl/fl}$ *Pf4-Cre* mice. Scale bars: 2 μm (**A**); 100 μm (**B**).

Methods

Differentiation of human and mouse megakaryocytes

Cord blood from normal full-term deliveries was obtained, and CD34$^+$ hematopoietic progenitors were isolated and differentiated into megakaryocytes as previously described (38, 39). Mature megakaryocytes were placed on immobilized human fibrinogen–coated surfaces in the presence of specific inhibitors or their vehicle, and the number of megakaryocytes that possessed proplatelets was counted by an independent blinded observer. On average, 12% ± 3% of vehicle-treated megakaryocytes had proplatelet extensions.

Mouse megakaryocytes were isolated from fetal liver as previously described (40). Mouse bone marrow–derived megakaryocytes were obtained using modifications of a published report (41). For the bone marrow megakaryocytes, C57BL/6 mice (8–10 weeks of age) were euthanized, and cells were obtained from the bone marrow of femur and tibia by flushing the bone marrow. Cells were homogenized by pipetting followed by passage through a 100-μm filter. The cell population was resuspended in 10% fetal bovine serum–supplemented DMEM with 2 mM L-glutamine, penicillin/streptomycin, and fibroblast condition media containing thrombopoietin. The cells were cultured for 5 days (37°C and 5% CO_2), and mature megakaryocytes were layered over a bovine serum albumin (BSA) gradient as described previously (42). Fetal liver and bone marrow–derived megakaryocytes were subsequently resuspended in culture media as described above, then placed on immobilized BSA or fibrinogen in the presence or absence of inhibitors, and megakaryocytes with proplatelets were counted. On average, 34% ± 1% of vehicle-treated fetal liver–derived megakaryocytes produced proplatelets. Proplatelet formation in vehicle-treated bone marrow–derived megakaryocytes was 50% ± 1%.

Inhibitors used in these in vitro studies (all diluted in DMSO) included bortezomib (100 nM; Selleck Chem), Y27632 (10 μM; Sigma-Aldrich), fasudil (10 μM; Selleck Chem), C3 transferase (10 μM; Cytoskeleton Inc.), SC-514 (0.5 μM; Calbiochem), MG132 (10 μM; Sigma-Aldrich), and lactacystin (10 μM; Sigma-Aldrich). Inhibitors were administered at different times, as indicated in the figure legends.

Next-generation RNA-Seq

Fetal liver–derived megakaryocytes for RNA-Seq were provided by J. Thon (Harvard Medical School, Boston, Massachusetts, USA). RNA from human CD34-differentiated or fetal liver–derived proplatelet-producing megakaryocytes was isolated and prepped for deep sequencing as previously described (43–45). In brief, RNA was prepared for sequencing according to Illumina's (DNA vision) TruSeq kit V2 for poly-A RNA. Libraries were sequenced 36 (human) and 50 (mouse) base pairs on an Illumina sequencer. Reads were aligned using Novoalign (Novocraft Technologies) software followed by processing, including RPKM assignment, using the USeq analysis package (46). The processed RNA-Seq data and aligned reads were deposited in GEO (accession no. GSE58202; ref. 47).

Protein expression analyses and assessment of RhoA activity

Cell lysates were placed in laemmli buffer, proteins were separated by SDS-page, and IκBα and phospho-MLC (Cell Signaling) were analyzed by Western blotting. To measure RhoA activity, platelets were placed in Mg^{2+} lysis buffer supplemented with protease (Roche Applied Science) and phosphatase inhibitors (Sigma-Aldrich). A small portion of the lysate was retained as total cell lysate, and the rest was incubated with the assay reagent. GTP-bound forms were eluted from the assay reagent using Laemmli sample buffer. Total RhoA and RhoA-GTP bound protein were analyzed by Western blotting using a pulldown kit (Millipore).

Mouse in vivo studies

In vivo measurements of platelets. In Figure 1A, platelet counts were determined at various time points with a Hemavet 950 (Drew Scientific). For platelet clearance, C57BL/6 mice were injected intravenously (i.v.) on day 0 with anti-GPIBβ Dylight 488 (0.1 μg/g body weight; Emfret Analytics) and intraperitoneally (i.p.) with bortezomib (2 mg/kg body weight) or its vehicle (10% DMSO in 0.9% saline). Blood samples (30 μl) were taken daily, diluted in Hanks balanced salt solution, and stained with a phycoerythrin-conjugated anti-mouse CD41 antibody (BD Biosciences), and clearance of Dylight 488–positive platelets was measured as previously described (48).

For estimation of platelet production, C57BL/6 mice were injected i.v. on day 0 with anti-GPIBα antibodies (3 μg/g body weight; Emfret Analytics) to deplete circulating platelets. On day 1,

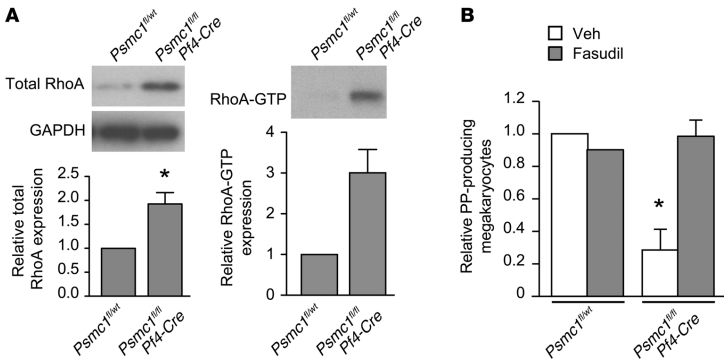

Figure 7. Genetic deletion of *Psmc1* in megakaryocytes is associated with increased RhoA protein and activity. (**A**) Representative Western blot of total RhoA and RhoA-GTP in megakaryocytes derived from *Psmc1*$^{fl/wt}$ and *Psmc1*$^{fl/fl}$ *Pf4-Cre* mice at P1. Also shown is densitometry quantification relative to *Psmc1*$^{fl/wt}$ control; for RhoA-GTP, megakaryocytes were isolated from 10 P1 mice, lysed, and then the lysates were pooled together for each pulldown experiment (see Methods). Data are mean ± SEM of 3 (total RhoA) and 2 (RhoA-GTP) experiments. **P* < 0.05 vs. *Psmc1*$^{fl/wt}$. (**B**) Bone marrow–derived megakaryocytes from *Psmc1*$^{fl/wt}$ and *Psmc1*$^{fl/fl}$ *Pf4-Cre* mice were treated with vehicle or fasudil, and the number of proplatelet-producing megakaryocytes was quantified and expressed relative to *Psmc1*$^{fl/wt}$ controls. Data are mean ± SEM of 3 independent experiments. **P* < 0.05 vs. vehicle-treated *Psmc1*$^{fl/wt}$.

platelet counts were assessed to confirm depletion; shortly after, mice were treated i.p. with bortezomib or its vehicle as above. Blood samples (2 μl) were taken daily for the remainder of the experiment, and platelet counts were measured by flow cytometry as previously described (13).

Knockout of the proteasome in mouse megakaryocytes and platelets. Megakaryocyte and platelet ablation of proteasome activity was achieved by crossing *Psmc1*$^{fl/fl}$ mice (provided by J. Mayer, Baylor College of Medicine, Houston, Texas, USA) with *Pf4-Cre* or *Pdgf-Cre-ER* mice (Jackson Labs), generating *Psmc1*$^{fl/wt}$ and *Psmc1*$^{fl/fl}$ *Pf4-Cre* mice or *Psmc1*$^{fl/wt}$ and *Psmc1*$^{fl/fl}$ *Pdgf-Cre-ER* mice. *Psmc1*$^{fl/fl}$ mice were also used as controls in select studies. Knockdown was confirmed in megakaryocytes using an antibody against PSMC1 (Novus Biologicals), and platelet counts were assessed as recently described (49). Tamoxifen (0.25 mg/kg) was administered i.p. to *Psmc1*$^{fl/fl}$ *Pdgf-Cre-ER* pups on P1, and then mortality was monitored from P2 to P21. For studies in adult *Psmc1*$^{fl/fl}$ *Pdgf-Cre-ER* mice, tamoxifen was administered 8 weeks after birth. In these mice, fasudil (5 mg/kg) was injected i.p. to *Psmc1*$^{fl/fl}$ *Pdgf-Cre-ER* mice 4 and 48 hours after tamoxifen administration, and blood was retrieved from tail veins on day 6 after tamoxifen to determine circulating platelet counts. In a subset of mice (n = 2 per treatment group), ex vivo assessment of proplatelet formation was performed. For these studies, mice were euthanized via CO_2 asphyxiation followed by cervical dislocation. Femurs were isolated, and bone marrow cords were flushed with HEPES-tyrodes buffer with 100 U/ml penicillin/streptomycin. Crude bone marrow cords were sliced into multiple sections, and buffer was replaced with HEPES-tyrodes buffer with 5% mouse serum and 100 U/ml penicillin/streptomycin. Bone marrow sections were then incubated at 37°C for 2 hours and stained with

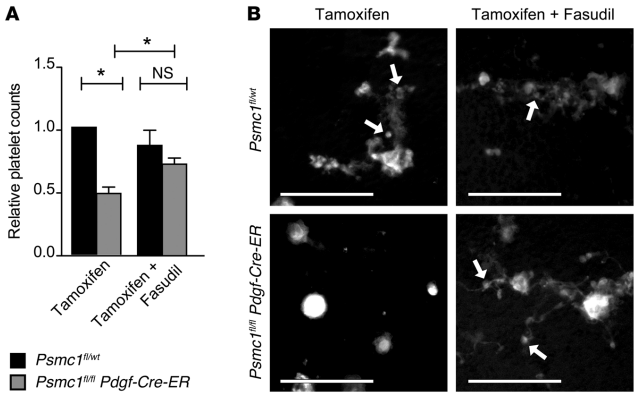

Figure 8. Inhibition of RhoA signaling rescues platelet counts in adult mice in which proteasome activity is conditionally deleted. (**A**) Tamoxifen was administered to adult *Psmc1*$^{fl/wt}$ and *Psmc1*$^{fl/fl}$ *Pdgf-Cre-ER* mice, followed by treatment with fasudil or saline control (4 and 48 hours after tamoxifen). Shown are platelet counts at day 6 after tamoxifen administration relative to *Psmc1*$^{fl/wt}$ controls treated with tamoxifen alone. Data are mean ± SEM of 9 experiments performed on independent mice. **P* < 0.05 as indicated. No significant difference was observed between groups treated with tamoxifen plus fasudil. (**B**) Representative images of Dylight 488–positive megakaryocytes present in crude bone marrow isolated from *Psmc1*$^{fl/wt}$ and *Psmc1*$^{fl/fl}$ *Pdgf-Cre-ER* mice immediately after euthanasia. Bone marrow for these studies was isolated from a subset of the mice in **A** (n = 2 per treatment group). Scale bars: 100 μm.

anti-GPIBβ Dylight 488. Megakaryocytes were imaged on a Nikon Eclipse TS100 fluorescence microscope and quantified by counting 10 fields (×20) per well.

Measurement of blood hematocrit

Hematocrit was measured in *Psmc1*$^{fl/wt}$ and *Psmc1*$^{fl/fl}$ *Pf4-Cre* mice at P3. After anesthesia (ketamine-xylazine; 0.2 mg/g body weight), blood was acquired via the retro-orbital venous plexus. Blood was collected into heparinized capillary tubes and spun at 50,000 *g* for 10 minutes to obtain a hematocrit for each mouse.

Histopathology

Organs from P1 mice were collected and fixed in neutral buffered formalin. Tissues were embedded in paraffin, sectioned at 10 μm, and stained with hematoxylin and eosin (H&E). Slides were then assessed by a hematopathologist.

Electron microscopy

Femurs from mice were collected, and bone marrow was flushed into glutaraldehyde 2.5% in PBS. Fixed samples were kept at 4°C, shipped to the Hospital for Sick Children in Toronto, and further processed and imaged as previously described (50).

Statistics

For multiple-group comparisons, data were subjected to 1-way analysis of variance (ANOVA), and Tukey's post-hoc test was used to assess statistical significance among groups. 2-way ANOVA with Newman-Keuls post-hoc test was used to assess statistical significance for the data in Figure 8B. 2-tailed Student's *t* test was used when comparisons were made between 2 groups. Differences in mortality were assessed by χ^2 test, and observed outcomes were graphed relative to calculated expected outcomes (Figure 5B and Supplemental Figure 13B). When possible, quantifications were done by a blinded observer. *P* values less than 0.05 were considered statistically significant.

All data graphed relative to controls (Figures 2–5, 7, and 8 and Supplemental Figures 4, 7, 10, and 13) were generated by comparing the average of the data set in each treated group with that of the control group (as the denominator).

Study approval

The human studies were approved by the University of Utah's Institutional Review Board (IRB no. 392). All participating subjects provided informed consent. Cord blood from normal full-term deliveries was obtained after informed consent by the mothers (IRB no. 11919). The mouse studies were approved by the University of Utah's Institutional Animal Care and Review Board (IACUC nos. 12-10002 and 12-11017) or by the Children's Hospital in Boston (IACUC no. A3431-01).

Further information can be found in the supplemental material and citations therein (51, 52).

Acknowledgments

We thank Diana Lim for preparation of the figures, critical comments, and consultation regarding responsible and effective display of the images. We also thank Guy Zimmerman for helpful discussions regarding the roles of the proteasome in platelets and megakaryocytes. This work was funded by NIH grants HL066277 and HL112311 (to A.S. Weyrich), HL112311, HL084516, and AR064788 (to D.Y. Li), GM103806 (to J.W. Rowley), and HL68130 (to J.E. Italiano Jr.); by the American Heart Association (13POST13930019 to K.R. Machlus; 11POST7290019 to R.A. Campbell; 0625098Y and 09BG1A2250381 to H. Schwertz); and by the Canadian Institutes of Health Research (MOP-259952 to W.H.A. Kahr). In addition, H. Schwertz was funded by a Lichtenberg-Professorship from the Volkswagen Foundation.

Address correspondence to: Dean Li or Andrew S. Weyrich, Eccles Institute of Human Genetics, 15 North 2030 East, Bldg. 533, Rm. 4150, Salt Lake City, Utah 84112, USA. Phone: 801.585.0950; E-mail: dean.li@u2m2.utah.edu (D. Li), andy.weyrich@u2m2.utah.edu (A.S. Weyrich).

1. Adams J, et al. Proteasome inhibitors: a novel class of potent and effective antitumor agents. *Cancer Res*. 1999;59(11):2615–2622.
2. Richardson PG, et al. A phase 2 study of bortezomib in relapsed, refractory myeloma. *N Engl J Med*. 2003;348(26):2609–2617.
3. Field-Smith A, Morgan GJ, Davies FE. Bortezomib (Velcadetrade mark) in the treatment of multiple myeloma. *Ther Clin Risk Manag*. 2006;2(3):271–279.
4. Ostrowska H, Ostrowska JK, Worowski K, Radziwon P. Human platelet 20S proteasome: inhibition of its chymotrypsin-like activity identification of the proteasome activator PA28. A preliminary report. *Platelets*. 2003;14(3):151–157.
5. Mitchell WB, Li J, French DL, Coller BS. αIIbβ3 biogenesis is controlled by engagement of αIIb in the calnexin cycle via the N15-linked glycan. *Blood*. 2006;107(7):2713–2719.
6. Kraemer BF, Weyrich AS, Lindemann S. Protein degradation systems in platelets. *Thromb Haemost*. 2013;110(5):920–924.
7. Nayak MK, Kulkarni PP, Dash D. Regulatory role of proteasome in determination of platelet life span. *J Biol Chem*. 2013;288(10):6826–6834.
8. Gupta N, Li W, Willard B, Silverstein RL, McIntyre TM. Proteasome proteolysis supports stimulated platelet function and thrombosis. *Arterioscler Thromb Vasc Biol*. 2014;34(1):160–168.
9. Kumari S, Dash D. Regulation of β-catenin stabilization in human platelets. *Biochimie*. 2013;95(6):1252–1257.
10. Nayak MK, Kumar K, Dash D. Regulation of proteasome activity in activated human platelets. *Cell Calcium*. 2011;49(4):226–232.
11. Avcu F, Ural AU, Cetin T, Nevruz O. Effects of bortezomib on platelet aggregation and ATP release in human platelets, in vitro. *Thromb Res*. 2008;121(4):567–571.
12. Lonial S, et al. Risk factors and kinetics of thrombocytopenia associated with bortezomib for relapsed, refractory multiple myeloma. *Blood*. 2005;106(12):3777–3784.
13. Mason KD, et al. Programmed anuclear cell death delimits platelet life span. *Cell*. 2007;128(6):1173–1186.
14. McConkey DJ. Bortezomib paradigm shift in myeloma. *Blood*. 2009;114(5):931–932.
15. Spinelli SL, et al. Platelets and megakaryocytes contain functional nuclear factor-kappaB. *Arterioscler Thromb Vasc Biol*. 2010;30(3):591–598.
16. Whitehead KJ, et al. The cerebral cavernous malformation signaling pathway promotes vascular integrity via Rho GTPases. *Nat Med*. 2009;15(2):177–184.
17. Gobbi G, et al. Proplatelet generation in the mouse requires PKCepsilon-dependent RhoA inhibition. *Blood*. 2013;122(7):1305–1311.
18. Suzuki A, et al. RhoA is essential for maintaining normal megakaryocyte ploidy and platelet generation. *PLoS One*. 2013;8(7):e69315.
19. Murai K, et al. Bortezomib induces thrombocytopenia by the inhibition of proplatelet formation of megakaryocytes [published online ahead of print April 21, 2014]. *Eur J Haematol*. doi:10.1111/ejh.12342.
20. Rubin DM, Glickman MH, Larsen CN, Dhruvakumar S, Finley D. Active site mutants in the six regulatory particle ATPases reveal multiple roles for ATP in the proteasome. *EMBO J*. 1998;17(17):4909–4919.
21. Kohler A, Cascio P, Leggett DS, Woo KM, Gold-

berg AL, Finley D. The axial channel of the proteasome core particle is gated by the Rpt2 ATPase controls both substrate entry product release. *Mol Cell*. 2001;7(6):1143–1152.
22. Smith DM, Fraga H, Reis C, Kafri G, Goldberg AL. ATP binds to proteasomal ATPases in pairs with distinct functional effects, implying an ordered reaction cycle. *Cell*. 2011;144(4):526–538.
23. Tiedt R, Schomber T, Hao-Shen H, Skoda RC. Pf4-Cre transgenic mice allow the generation of lineage-restricted gene knockouts for studying megakaryocyte platelet function in vivo. *Blood*. 2007;109(4):1503–1506.
24. Galimberti S, et al. PS-341 (Bortezomib) inhibits proliferation induces apoptosis of megakaryoblastic MO7-e cells. *Leuk Res*. 2008;32(1):103–112.
25. Zhang Y, Wang Z, Liu DX, Pagano M, Ravid K. Ubiquitin-dependent degradation of cyclin B is accelerated in polyploid megakaryocytes. *J Biol Chem*. 1998;273(3):1387–1392.
26. Necchi V, et al. Ubiquitin/proteasome-rich particulate cytoplasmic structures (PaCSs) in the platelets and megakaryocytes of ANKRD26-related thrombo-cytopenia. *Thromb Haemost*. 2012;109(2):263–271.
27. Murone M, Carpenter DA, de Sauvage FJ. Hematopoietic deficiencies in c-mpl and TPO knockout mice. *Stem Cells*. 1998;16(1):1–6.
28. Bertozzi CC, Hess PR, Kahn ML. Platelets: covert regulators of lymphatic development. *Arterioscler Thromb Vasc Biol*. 2010;30(12):2368–2371.
29. Benezech C, et al. CLEC-2 is required for development maintenance of lymph nodes. *Blood*. 2014;123(20):3200–3207.
30. Herzog BH, et al. Podoplanin maintains high endothelial venule integrity by interacting with platelet CLEC-2. *Nature*. 2013;502(7469):105–109.
31. Osada M, et al. Platelet activation receptor CLEC-2 regulates blood/lymphatic vessel separation by inhibiting proliferation, migration, tube formation of lymphatic endothelial cells. *J Biol Chem*. 2012;287(26):22241–22252.
32. Finney BA, et al. CLEC-2 and Syk in the megakaryocytic/platelet lineage are essential for development. *Blood*. 2012;119(7):1747–1756.
33. Bertozzi CC, et al. Platelets regulate lymphatic vascular development through CLEC-2-SLP-76 signaling. *Blood*. 2010;116(4):661–670.
34. Levin J, et al. Pathophysiology of thrombocytopenia and anemia in mice lacking transcription factor NF-E2. *Blood*. 1999;94(9):3037–3047.
35. Boulaftali Y, et al. Platelet ITAM signaling is critical for vascular integrity in inflammation. *J Clin Invest*. 2013;123(2):908–916.
36. Hamilton AM, et al. Activity-dependent growth of new dendritic spines is regulated by the proteasome. *Neuron*. 2012;74(6):1023–1030.
37. Jeon CY, et al. Control of neurite outgrowth by RhoA inactivation. *J Neurochem*. 2012;120(5):684–698.
38. Foulks JM, et al. PAF-acetylhydrolase expressed during megakaryocyte differentiation inactivates PAF-like lipids. *Blood*. 2009;113(26):6699–6706.
39. Denis MM, et al. Escaping the nuclear confines: signal-dependent pre-mRNA splicing in anucleate platelets. *Cell*. 2005;122(3):379–391.
40. Thon JN, Italiano JE. Visualization and manipulation of the platelet and megakaryocyte cytoskeleton. *Methods Mol Biol*. 2012;788:109–125.
41. Mazharian A, Watson SP, Severin S. Critical role for ERK1/2 in bone marrow fetal liver-derived primary megakaryocyte differentiation, motility, proplatelet formation. *Exp Hematol*. 2009;37(10):1238–1249.
42. Thon JN, et al. Cytoskeletal mechanics of proplatelet maturation and platelet release. *J Cell Biol*. 2010;191(4):861–874.
43. Cecchetti L, Tolley ND, Michetti N, Bury L, Weyrich AS, Gresele P. Megakaryocytes differentially sort mRNAs for matrix metalloproteinases and their inhibitors into platelets: a mechanism for regulating synthetic events. *Blood*. 2011;118(7):1903–1911.
44. Kahr WH, et al. Mutations in NBEAL2, encoding a BEACH protein, cause gray platelet syndrome. *Nat Genet*. 2011;43(8):738–740.
45. Rowley JW, et al. Genome-wide RNA-seq analysis of human and mouse platelet transcriptomes. *Blood*. 2011;118(14):e101–e111.
46. Nix DA, Courdy SJ, Boucher KM. Empirical methods for controlling false positives and estimating confidence in ChIP-Seq peaks. *BMC Bioinformatics*. 2008;9.
47. Edgar R, Domrachev M, Lash AE. Gene Expression Omnibus: NCBI gene expression and hybridization array data repository. *Nucleic Acids Res*. 2002;30(1):207–210.
48. Josefsson EC, White MJ, Dowling MR, Kile BT. Platelet life span and apoptosis. *Methods Mol Biol*. 2012;788:59–71.
49. Liu ZJ, et al. Expansion of the neonatal platelet mass is achieved via an extension of platelet lifespan. *Blood*. 2014;123(22):3381–3389.
50. Kahr WH, et al. Abnormal megakaryocyte development and platelet function in Nbeal2(–/–) mice. *Blood*. 2013;122(19):3349–3358.
51. Holly SP, et al. Chemoproteomic discovery of AADACL1 as a regulator of human platelet activation. *Chem Biol*. 2013;20(9):1125–1134.
52. Ramskold D, Wang ET, Burge CB, Sandberg R. An abundance of ubiquitously expressed genes revealed by tissue transcriptome sequence data. *PLoS Comput Biol*. 2009;5(12):e1000598.

Supplemental Material

Supplemental Methods

Human and Mouse Platelet Isolation. Whole blood from humans or mice was drawn into acid-citrate-dextrose (ACD) and platelets were isolated as previously described (39, 45). Freshly-isolated platelets were resuspended in M199 culture medium for each experiment.

Assessment of human megakaryocyte activation and adhesion. To measure megakaryocyte spreading and adhesion, day 13 $CD34^+$ progenitor cell derived megakaryocytes were placed on immobilized human fibrinogen (100 μg/ml; Calbiochem-Novabiochem Corporation, San Diego, CA) coated glass cover slips and incubated 2-6 hours in the presence or absence of inhibitors (described above), controls (DMSO), or media alone. After indicated time points, cells were fixed with 4% paraformaldehyde for 20 minutes at room temperature followed by permeabilization in 0.1% Triton-X 100 for 5 minutes. Fixed and permeabilized cells were stained with Alexa fluor 488 Phalloidin, Alexa fluor 555 Wheat Germ Agglutinin (WGA), and TO-PRO 3 (Life Technologies, Grand Island, NY). Cells were imaged using an FV300 Olympus IX81 microscope (Melville, NY). Adherent cells were quantified by counting five 20x fields per chamber. All quantifications were done by a blind observer.

To measure activation, $CD34^+$ progenitor cell derived megakaryocytes were isolated as above. Megakaryocytes were treated with thrombin and PAC-1 binding was measured as described previously by us (38). Fibrinogen binding was also determined in megakaryocytes using published methods from our group. (51).

Ex vivo assessment of megakaryocyte numbers in bone marrow and spleen. A rabbit anti-human von-Willebrand factor (vWF) antibody known to cross-react with murine vWF (Dako, Denmark) was used as the primary antibody to immunohistochemically stain megakaryocytes present in the bone marrow or spleen of *Psmc1*$^{fl/wt}$ and *Psmc1*$^{fl/fl}$*;Pf4cre* mice. A biotinylated horse anti-rabbit antibody was used as the secondary antibody, and color development was achieved with DAB substrate following the Vector Elite ABC kit protocols (Vector, Burlingame, CA). Megakaryocytes, identified by vWF staining in conjunction with morphological features, were then quantified using an eyepiece reticle that delineates an area of tissue measuring 250 x 250 μm at 400X (Klarmann Rulings Inc, Litchfield, NH). The megakaryocyte concentration was expressed as number of megakaryocytes in an area of bone marrow or spleen measuring 250 x 250 μm.

Ex vivo assessment of platelet aggregation. Platelet aggregation studies were performed as previously described (8). Briefly, washed platelets were resuspended in HBSS with 0.5% human serum albumin and preincubated with bortezomib or vehicle control for 30 minutes at 37^{o}C. Treated platelets were then stimulated with 0.05 U/ml or 0.2 U/ml thrombin and aggregation was monitored by transmittance (Chronolog) with stirring (600 rpm).

Ex vivo assessment of mouse and human platelet activation. Washed mouse platelets (1 x 10^6) were resuspended in M199 media, pretreated for 30 minutes with bortezomib or its vehicle, and then left alone or activated for 15 minutes with varying concentrations of U46619, convulxin, or Par4 in the presence of PE-JonA (Emfret Analytics, Eibelstadt, Germany), an antibody that recognizes the active form of integrin $\alpha_{IIb}\beta_3$. Agonist-induced expression of surface P-selectin expression (Santa Cruz Biotech, Santa Cruz, CA) was also assessed by flow cytometry in separate experiments.

Washed human platelets ($5x10^8$ total) were resuspended in M199 medium containing 100µg/ml of fibrinogen and were pretreated for 30 minutes with bortezomib or its vehicle. Platelets were then stimulated with U46619, ADP, or thrombin for 15 minutes in the presence of PAC-1 (BD Biosciences, Franklin, NJ), an antibody that binds to the active conformation of integrin $\alpha_{IIb}\beta_{3.}$. Platelets were analyzed immediately using a FacScan.

Supplemental Figures and Table Legend

Supplemental Figure 1. *Bortezomib does not directly activate or alter Par4-induced activation in mouse platelets.* Washed mouse platelets were left alone or incubated with increasing concentrations of Par4. After 15 minutes, JonA binding was assessed by flow cytometry. The bars represent the mean±SEM of 3 independent experiments.

Supplemental Figure 2. *Inhibition of the proteasome ex vivo does not alter the function of mouse platelets.* Washed mouse platelets were pretreated with Bort or its Veh and subsequently stimulated with increasing concentrations of U46619 or convulxin as described in the Methods section. After 15 minutes, JonA binding (**A**) or P-selectin surface expression (**B**) was assessed by flow cytometry. The bars represent the mean±SEM of 3 independent experiments.

Supplemental Figure 3. *Inhibition of the proteasome ex vivo does not alter the function of human platelets.* Washed human platelets were pretreated with Bort or its Veh and subsequently stimulated with increasing concentrations of U46619, ADP, or thrombin as described in the Methods section. After 15 minutes, PAC-1 binding was assessed by flow cytometry. The bars represent the mean±SEM of 3 independent experiments.

Supplemental Figure 4. *MG132 attenuates proplatelet formation*. Human megakaryocytes were left alone (NT – no treatment) or treated with MG132 and then analyzed by confocal microscopy (6 hours post-MG132). The images show megakaryocytes stained with WGA (red) and phalloidin (green) where white arrows point to proplatelet extensions and yellow arrows point to non-proplatelet producing megakaryocytes. Scale bar = 50μm. The bar graph on the right depicts the relative change in proplatelet producing megakaryocytes in MG132 treated

cells compared to untreated cells. The bars represent the mean±SEM of 3 independent experiments and the asterisk is $p<0.05$ compared to NT.

Supplemental Figure 5. *Inhibition of the proteasome does not alter $\alpha_{IIb}\beta_3$ activity in human megakaryocytes*. (**A**) $CD34^+$-derived human megakaryocytes were treated with Veh or Bort and binding of soluble fibrinogen (FGN), in the presence or absence of 0.05 U/ml of thrombin (Thr), was assessed as described in the Methods section. The bars represent the mean±SEM of 3 experiments and the asterisk identifies $p<0.05$ when comparing megakaryocytes with and without Thr to one another. There was no difference in soluble FGN binding when comparing Veh to Bort treated megakaryocytes. MFI = mean fluorescent intensity. (**B**) PAC-1 binding to megakaryocytes in the presence of Bort, Veh, or Thr (0.05 U/ml). The bars represent the mean±SEM of 3 experiments and the asterisk identifies $p<0.05$ compared to Thr-treated megakaryocytes.

Supplemental Figure 6. *Inhibition of the proteasome does not alter adherence of human megakaryocytes to fibrinogen*. Human megakaryocytes were placed on immobilized fibrinogen for 1 hour in the presence of Veh or Bort. The cells were analyzed by confocal microscopy and adhered megakaryocytes were counted in five different fields. The bars represent the mean±SEM of 2 independent experiments.

Supplemental Figure 7. *The proteasome regulates human proplatelet formation through the RhoA signaling pathway*. Human megakaryocytes were treated with Veh, Bort, or Bort + C3 transferase and the change in the relative number of proplatelet producing megakaryocytes in treated groups compared to Veh was assessed. The bars in this figure represent the mean±SEM of 3 independent experiments. The asterisk is $p<0.05$ compared to Veh.

Supplemental Figure 8. *Psmc1 protein is expressed in human and mouse megakaryocytes*. Human $CD34^{+}$-derived and mouse bone marrow derived proplatelet producing megakaryocytes lysates were separated by SDS-Page and protein for Psmc1 was assessed. Lanes 1 and 2 show Psmc1 protein expression levels in two independent human megakaryocyte samples. Lanes 3 and 4 show Psmc1 protein expression in two independent mouse megakaryocyte samples.

Supplemental Figure 9. *Protein for Psmc1 is reduced in megakaryocytes, but not other tissues, isolated from* $Psmc1^{fl/fl}$*;PF4cre.* (**A**) Western blot of megakaryocyte lysates obtained from $Psmc1^{fl/wt}$ and $Psmc1^{fl/fl}$*;PF4cre* mice. Protein for Psmc1 is shown in the top panel. After Psmc1 protein levels were assessed, the gel was stained with coomassie blue. A coomassie stained region of this gel is shown in the bottom panel. This image is representative of 4 independent experiments. (**B**) Western blot of Psmc1 protein expression in megakaryocytes, brain, heart, liver and thymus from $Psmc1^{fl/wt}$ and $Psmc1^{fl/fl}$*;PF4cre* mice. After Psmc1 protein levels were assessed, the gel was stained with coomassie blue. Coomassie stained regions for each tissue are shown in the bottom panel.

Supplemental Figure 10. *Genetic ablation of proteasome activity in megakaryocytes increases protein ubiquitination.* The top left panel shows a representative western blot of ubiquitinated proteins in megakaryocytes derived from $Psmc1^{fl/wt}$ and $Psmc1^{fl/fl}$*;Pf4cre* mice. The corresponding coomassie image of this gel is shown directly below. The bars in the right panel show the relative change in ubiquitin expression in megakaryocytes from $Psmc1^{fl/fl}$*;PF4cre* mice compared to $Psmc1^{fl/wt}$ mice. The asterisk is $p<0.05$ compared to $Psmc1^{fl/wt}$ mice.

Supplemental Figure 11. *Deletion of Psmc1 in megakaryocytes does not alter the number of megakaryocytes found in the bone marrow or spleen.* Sections of bone marrow and spleen were stained for von Willebrand Factor (vWF) and vWF positive megakaryocytes were assessed in *Psmc1$^{fl/wt}$* and *Psmc1$^{fl/fl}$;PF4cre* mice. The left panels show representative bone marrow and spleen tissue sections. Higher magnification insets from the spleen tissue sections are shown at the very bottom. The red boxes indicate the region of the spleen selected for the inset. Scale bars for full images = 50μm. Scale bars for insets = 20μm. In the far right panel, the number of megakaryocytes in the bone marrow and spleen were counted as described in the Methods section. The bars on the right represent the mean±SEM of tissue sections from 3 *Psmc1$^{fl/wt}$* and 3 *Psmc1$^{fl/fl}$;PF4cre* mice.

Supplemental Figure 12. *c-mpl and Psmc1$^{fl/fl}$;PF4cre mice are thrombocytopenic, but platelet counts are lower in Psmc1$^{fl/fl}$;PF4cre mice.* Platelet counts at P3 in *Psmc1$^{fl/wt}$* and *Psmc1$^{fl/fl}$;PF4cre* mice were compared to platelet counts from *c-mpl* knockout mice (*c-mpl$^{ko/ko}$*) and their littermate controls (*c-mpl$^{wt/wt}$*). As shown in this figure, thrombocytopenia is observed in both the *c-mpl$^{ko/ko}$* and *Psmc1$^{fl/fl}$;PF4cre* mice but is more severe in the *Psmc1$^{fl/fl}$;PF4cre* mice. The bars represent the mean±SEM of platelet counts obtained from 6 mice for each experimental group. The asterisk is $p<0.05$ between groups designated by the lines above the bars.

Supplemental Figure 13. *Inducible deletion of Psmc1 in Pdgfcre-ER mice at P1 results in thrombocytopenia and death*. (**A**) Relative changes in platelet counts in *Psmc1$^{fl/fl}$;Pdgf-creER* mice compared to *Psmc1$^{fl/fl}$ and Psmc1$^{fl/wt}$* mice. Platelet counts were determined 1 day post-tamoxifen. The bars represent the mean±SEM of 3 independent experiments and the asterisk is $p<0.05$ compared to control mice. (**B**) Mortality rates in *Psmc1$^{fl/fl}$ and Psmc1$^{fl/wt}$* compared to

Psmc1$^{fl/fl}$;Pdgf-creER mice treated with tamoxifen on postnatal day 1 (P1). Mortality was assessed at postnatal day 2 (P2) and 21 (P21). The bars represent a Chi-square analysis comparing the expected versus observed genotypes at P1 and P21 (n=82) where the asterisk denotes significance as determined by a Chi-square distribution table.

Supplemental Figure 14. *Bortezomib blunts human platelet aggregation in response to low dose thrombin*. Washed human platelets were preincubated with Veh or Bort and stimulated with low dose (0.05 U/ml) thrombin in the left panel or high dose (0.2 U/ml) thrombin in the right panel. Aggregation was monitored by light transmittance using a Chronolog platelet aggregometer. The platelet aggregation tracings are representative of three independent experiments.

Supplemental Table 1. *Expression of transcripts coding for proteasome subunits in human and mouse megakaryocytes***.** Poly-A RNA isolated from CD34^{+}-derived human megakaryocytes and fetal liver derived mouse megakaryocytes were sequenced on an Illumina genome analyzer. Reads were aligned and RPKM (reads per kilobase per million) expression estimates were calculated as previously described (45). RPKM values with a threshold at $\leq$0.3 identify mRNAs with expression levels above background (45, 52). Transcripts listed are proteasome subunits found within the gene ontology term “proteasome complex.”

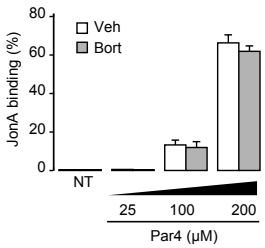

Supplemental Figure 1
D Shi & M Smith, et al.

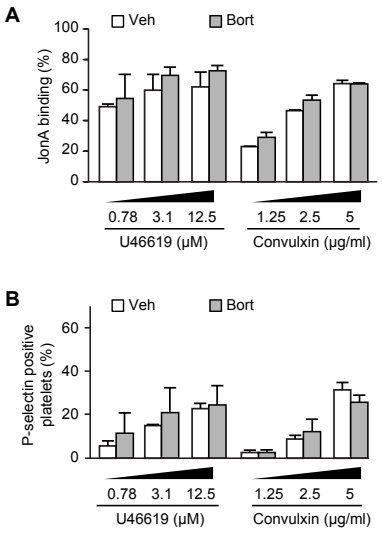

Supplemental Figure 2
D Shi & M Smith, et al.

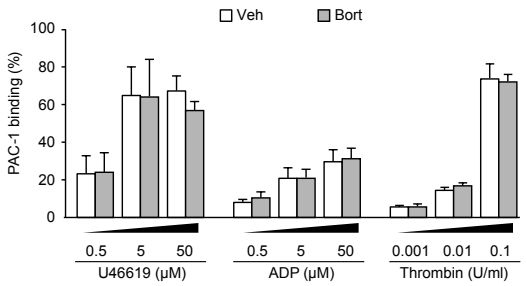

Supplemental Figure 3
D Shi & M Smith, et al.

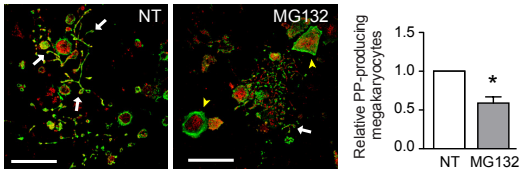

Supplemental Figure 4
D Shi & M Smith, et al.

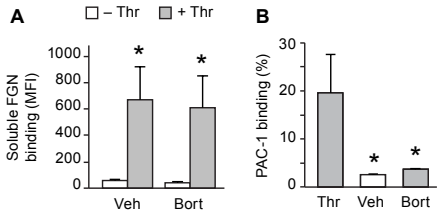

Supplemental Figure 5
D Shi & M Smith, et al.

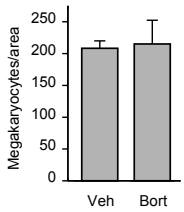

Supplemental Figure 6
D Shi & M Smith, et al.

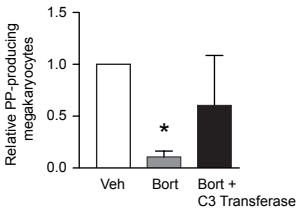

Supplemental Figure 7
D Shi & M Smith, et al.

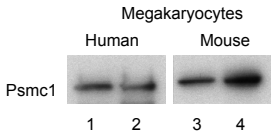

Supplemental Figure 8
D Shi & M Smith, et al.

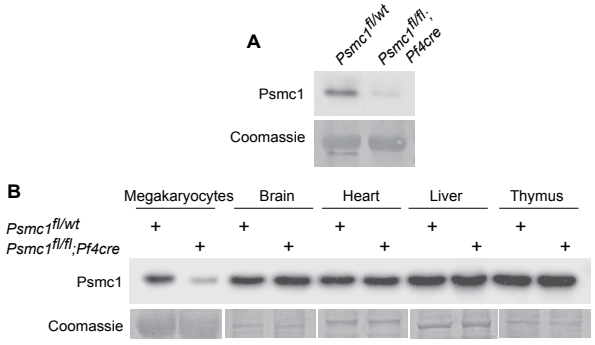

Supplemental Figure 9
D Shi & M Smith, et al.

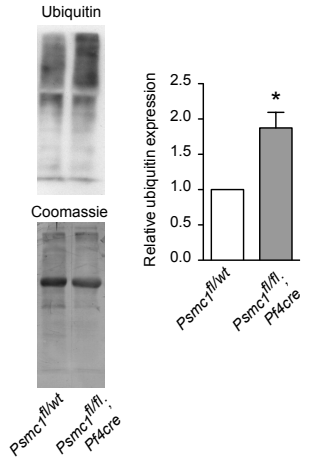

Supplemental Figure 10
D Shi & M Smith, et al.

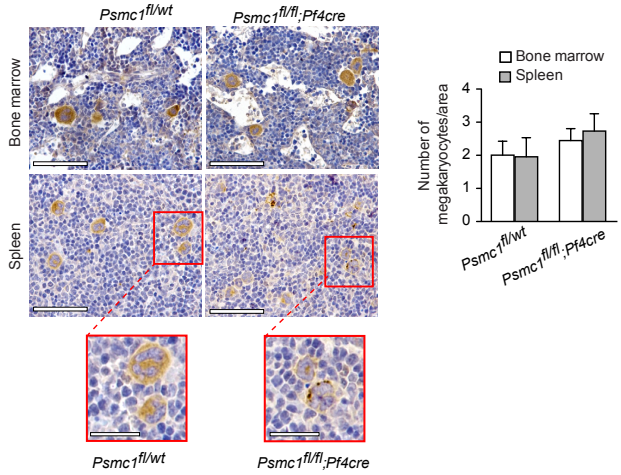

Supplemental Figure 11
D Shi & M Smith, et al.

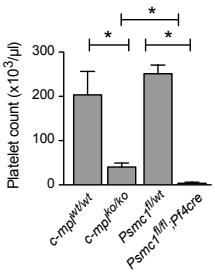

Supplemental Figure 12
D Shi & M Smith, et al.

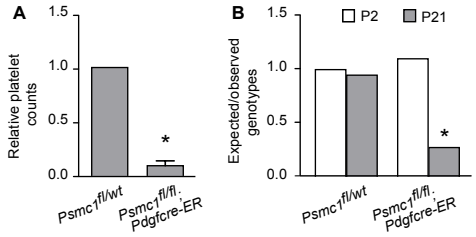

Supplemental Figure 13
D Shi & M Smith, et al.

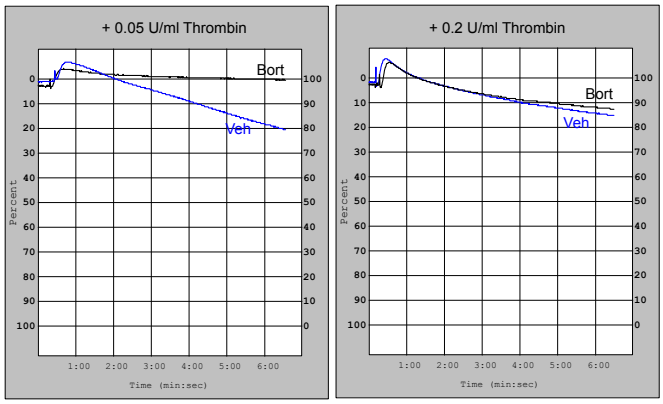

Supplemental Figure 14
D Shi & M Smith, et al.

Supplemental Table 1.

Gene	Human $CD34^+$ Megs	Murine Fetal Liver Megs
proteasome 26S subunit, ATPase, 1	2.07	38.73
proteasome 26S subunit, ATPase, 2	30.23	16.62
proteasome 26S subunit, ATPase, 3	112.71	44.12
proteasome 26S subunit, ATPase, 4	90.42	26.15
proteasome 26S subunit, ATPase, 5	143.93	41.51
proteasome 26S subunit, ATPase, 6	13.60	40.92
proteasome 26S subunit, non-ATPase, 1	58.30	25.59
proteasome 26S subunit, non-ATPase, 2	95.75	43.05
proteasome 26S subunit, non-ATPase, 3	113.65	15.10
proteasome 26S subunit, non-ATPase, 4	67.07	85.09
proteasome 26S subunit, non-ATPase, 5	8.08	12.86
proteasome 26S subunit, non-ATPase, 6	103.13	31.87
proteasome 26S subunit, non-ATPase, 7	73.95	32.28
proteasome 26S subunit, non-ATPase, 8	115.63	128.93
proteasome 26S subunit, non-ATPase, 9	24.49	5.45
proteasome 26S subunit, non-ATPase, 10	22.52	20.26
proteasome 26S subunit, non-ATPase, 11	64.91	33.28
proteasome 26S subunit, non-ATPase, 12	25.27	22.85
proteasome 26S subunit, non-ATPase, 13	73.65	39.99
proteasome 26S subunit, non-ATPase, 14	39.55	19.04
proteasome subunit, alpha type, 1	54.43	38.70
proteasome subunit, alpha type, 2	22.37	33.71
proteasome subunit, alpha type, 3	60.60	5.50
proteasome subunit, alpha type, 4	92.04	28.32
proteasome subunit, alpha type, 5	105.97	12.41
proteasome subunit, alpha type, 6	80.73	116.02
proteasome subunit, alpha type, 7	187.17	36.16
proteasome subunit, beta type, 1	166.42	182.02
proteasome subunit, beta type, 2	71.94	47.88
proteasome subunit, beta type, 3	125.76	8.63
proteasome subunit, beta type, 4	224.93	91.72
proteasome subunit, beta type, 5	67.47	38.21
proteasome subunit, beta type, 6	114.32	38.13
proteasome subunit, beta type, 7	123.10	51.79
proteasome subunit, beta type, 10	36.24	22.47

CHAPTER 3

INTERLEUKIN RECEPTOR ACTIVATES A MYD88-ARNO-ARF6 CASCADE TO DISRUPT VASCULAR STABILITY

The following chapter is a reprint of a manuscript published in Nature. It was published December 13, 2012, volume 492, pages 252-255. In addition to myself, the other authors were Weiquan Zhu, Nyall London, Christopher Gibson, Chadwick Davis, Zongzhong Tong, Lise Sorenson, Jinping Guo, Matthew Smith, Allie Grossman, Kirk Thomas, and Dean Li. I participated in the interpretation of data and preparation of the manuscript.

LETTER

doi:10.1038/nature11603

Interleukin receptor activates a MYD88–ARNO–ARF6 cascade to disrupt vascular stability

Weiquan Zhu[1,2]*, Nyall R. London[1,2,3]*, Christopher C. Gibson[2,4]*, Chadwick T. Davis[2,5], Zongzhong Tong[6], Lise K. Sorensen[2], Dallas S. Shi[2,5], Jinping Guo[1,2,7], Matthew C. P. Smith[1,2,3], Allie H. Grossmann[2,8], Kirk R. Thomas[1,2] & Dean Y. Li[1,2,3,9,10]

The innate immune response is essential for combating infectious disease. Macrophages and other cells respond to infection by releasing cytokines, such as interleukin-1β (IL-1β), which in turn activate a well-described, myeloid-differentiation factor 88 (MYD88)-mediated, nuclear factor-κB (NF-κB)-dependent transcriptional pathway that results in inflammatory-cell activation and recruitment[1–4]. Endothelial cells, which usually serve as a barrier to the movement of inflammatory cells out of the blood and into tissue, are also critical mediators of the inflammatory response[5,6]. Paradoxically, the cytokines vital to a successful immune defence also have disruptive effects on endothelial cell–cell interactions and can trigger degradation of barrier function and dissociation of tissue architecture[7–9]. The mechanism of this barrier dissolution and its relationship to the canonical NF-κB pathway remain poorly defined. Here we show that the direct, immediate and disruptive effects of IL-1β on endothelial stability in a human *in vitro* cell model are NF-κB independent and are instead the result of signalling through the small GTPase ADP-ribosylation factor 6 (ARF6) and its activator ARF nucleotide binding site opener (ARNO; also known as CYTH2). Moreover, we show that ARNO binds directly to the adaptor protein MYD88, and thus propose MYD88–ARNO–ARF6 as a proximal IL-1β signalling pathway distinct from that mediated by NF-κB. Finally, we show that SecinH3, an inhibitor of ARF guanine nucleotide-exchange factors such as ARNO, enhances vascular stability and significantly improves outcomes in animal models of inflammatory arthritis and acute inflammation.

A defining characteristic of the cytokine-induced inflammatory response is the destabilization of endothelial barriers resulting in vascular permeability[7–9]. To dissect the pathway(s) involved in this tissue disruption, we treated cultured monolayers of human dermal microvascular endothelial cells (HMVEC-d) with IL-1β, and detected an increase in endothelial permeability within 15 min (Fig. 1a). The canonical IL-1β pathway involves ligand-stimulated activation of interleukin-1 receptor (IL-1R), which recruits MYD88 to its cytoplasmic tail[10]. The subsequent signalling cascade through IRAK1 results in the phosphorylation of IκB-α by the IκB kinase (IKK) complex, leading to translocation of NF-κB to the nucleus and the eventual transcription of target genes that promote inflammatory-cell responses[3,4] (Supplementary Fig. 1). To test the involvement of this pathway in IL-1β-induced vascular permeability, cells were treated with the IKK inhibitor SC-514 (ref. 11). Although SC-514 prevented IL-1β-induced nuclear localization of NF-κB, it was unable to rescue either IL-1β-induced permeability or disruption of vascular endothelial (VE)-cadherin surface localization (Fig. 1b, c and Supplementary Fig. 2a–c). We also wondered whether IL-1β-induced vascular permeability required other known MYD88-mediated downstream signalling mechanisms, including ERK1/2, p38 and JNK (also known as MAPK3/MAPK1, MAPK14 and MAPK8, respectively)[12,13]. Although ERK1/2, p38 and JNK were activated by IL-1β stimulation of endothelial cells, small-molecule inhibitors of each of these pathways were unable to prevent IL-1β-induced vascular permeability or IL-1β-induced disruption of VE-cadherin cell-surface localization (Supplementary Fig. 2d–h). Although specific NF-κB targets, such as VEGFA, COX-2 (also known as PTGS2) and the COX-2 product prostaglandin E_2 are modulated by IL-1β, their activation had no effect on IL-1β-induced endothelial permeability[3,14,15] (Supplementary Fig. 3a–e). Finally, treatment with actinomycin D or cycloheximide effectively inhibited transcription or translation, respectively, of NF-κB targets, but did not blunt IL-1β-induced permeability (Fig. 1d and Supplementary Fig. 3f, g). These data strongly support a role for the immediate and destabilizing effects of IL-1β on endothelial stability through signalling pathways independent of NF-κB, transcription and translation.

IL-1β can disrupt VE-cadherin cell-surface localization by promoting endocytic internalization[9]. We proposed that IL-1β might use ARF6, a known regulator of adherens protein localization[16,17]. Indeed, IL-1β activated ARF6 in HMVEC-d within 1 min, a response accompanied by increased endocytosis of VE-cadherin within 5 min and an increase in monolayer permeability within 15 min (Fig. 1a, e and Supplementary Fig. 4a, b). IL-1β treatment did not affect total VE-cadherin messenger RNA or protein levels (Supplementary Fig. 4c, d). Adenoviral-mediated overexpression of constitutively active ARF6 (ARF6(Q67L))[18] elicited a dose-dependent increase in endothelial permeability, as well as a disruption of VE-cadherin cell-surface localization (Fig. 1f, g and Supplementary Fig. 4e, f). A similar dose-dependent loss of total VE-cadherin was also observed, probably through internalization and subsequent degradation (Supplementary Fig. 4g). Interestingly, at lower doses of adenovirus at which permeability was still induced, loss of total VE-cadherin was not observed, but a dose-dependent loss of cell-surface VE-cadherin occurred (Fig. 1f–h and Supplementary Fig. 4g). Moreover, short interfering RNA (siRNA) knockdown of *ARF6* enhanced VE-cadherin cell-surface localization and prevented both IL-1β-induced disruption of VE-cadherin and IL-1β-induced endothelial permeability (Fig. 1i–k and Supplementary Fig. 4h, i). Collectively, these data link ARF6 as a critical regulator of VE-cadherin trafficking by controlling cell-surface localization and the immediate and disruptive effects of IL-1β-induced vascular permeability.

The ARF6 activation state is decreased through interaction with GTPase-activating proteins (GAPs) and increased through interaction with guanine nucleotide-exchange factors (GEFs). Consistent with this, treatment of endothelial cells with the ARF-GAP inhibitor QS11 evoked an increase in ARF6–GTP, a decrease in VE-cadherin cell-surface localization and increased permeability (Fig. 2a–d and

[1]Department of Medicine, University of Utah, Salt Lake City, Utah 84112, USA. [2]Program in Molecular Medicine, University of Utah, Salt Lake City, Utah 84112, USA. [3]Department of Oncological Sciences, University of Utah, Salt Lake City, Utah 84112, USA. [4]Department of Bioengineering, University of Utah, Salt Lake City, Utah 84112, USA. [5]Department of Human Genetics, University of Utah, Salt Lake City, Utah 84112, USA. [6]Navigen Inc, Salt Lake City, Utah 84112, USA. [7]Department of Anatomy, Second Military Medical University, Shanghai 200433, China. [8]Department of Pathology, University of Utah, Salt Lake City, Utah 84112, USA. [9]Cardiology Section, VA Salt Lake City Health Care System, Salt Lake City, Utah 84112, USA. [10]The Key Laboratory for Human Disease Gene Study of Sichuan Province, Institute of Laboratory Medicine, Sichuan Academy of Medical Sciences & Sichuan Provincial People's Hospital, Chengdu, Sichuan 610072, China.
*These authors contributed equally to this work.

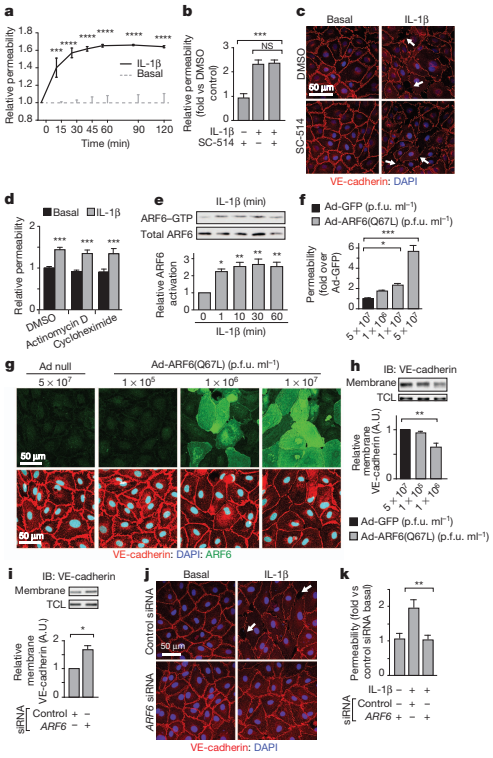

Figure 1 | Immediate effects of IL-1β are NF-κB independent and ARF6 dependent. **a**–**d**, Monolayers of HMVEC-d stimulated with IL-1β and assayed for permeability to horseradish peroxidase (HRP) over time (**a**), permeability to HRP following 2-h treatment with SC-514 (**b**), immunofluorescent localization of VE-cadherin (**c**) and permeability to HRP after 30-min treatment with actinomycin D or cycloheximide (**d**). **e**, IL-1β-stimulated HMVEC-d lysates were precipitated with glutathione *S*-transferase (GST)–GGA3 and immunoblotted for ARF6. **f**–**i**, HMVEC-d monolayers infected with adenovirus (Ad) containing empty vector (null), green fluorescent protein (GFP) or ARF6(Q67L), showing permeability (**f**) and VE-cadherin localization (**g**) (green denotes ARF6 expression). Membrane fractions from adenoviral-vector-infected (**h**) or *ARF6*-siRNA-treated (**i**) HMVEC-d were immunoblotted for VE-cadherin. **j**, **k**, *ARF6*-siRNA-treated HMVEC-d stimulated with IL-1β, showing VE-cadherin localization (**j**) (arrows denote disrupted VE-cadherin cell-surface localization) and permeability (**k**). A.U., arbitrary unit; DMSO, dimethylsulphoxide; IB, immunoblot; TCL, total cell lysate. $n \geq 3$; error bars denote s.e.m. $^{*}P < 0.05$, $^{**}P < 0.01$, $^{***}P < 0.001$, $^{****}P < 0.0001$.

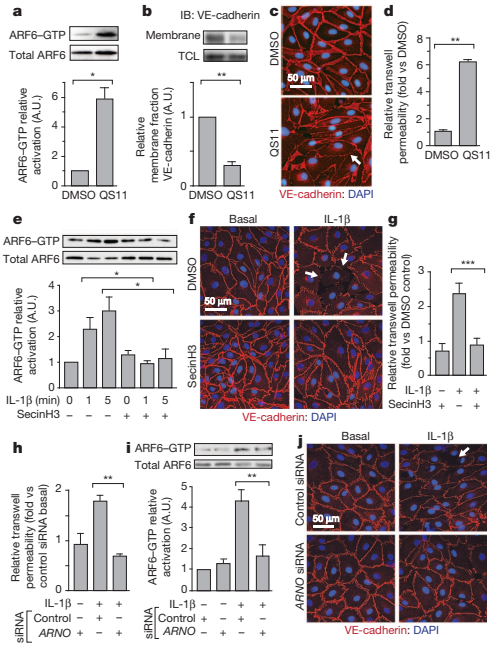

Figure 2 | Inhibition of ARF-GAPs and ARF-GEFs affect ARF6 activation and VE-cadherin localization. **a**–**d**, HMVEC-d treated with QS11, showing whole-cell lysates precipitated with GST–GGA3 and immunoblotted for ARF6 (**a**), membrane fractions immunoblotted for VE-cadherin (**b**), immunofluorescence for VE-cadherin (red) (**c**) and permeability to HRP (**d**). **e**–**g**, HMVEC-d treated with IL-1β and SecinH3, showing immunoblotting for ARF6 (**e**), immunofluorescence for VE-cadherin (**f**) and permeability to HRP (**g**). **h**–**j**, HMVEC-d treated with anti-*ARNO* siRNA and stimulated with IL-1β, showing permeability to HRP (**h**), GST–GGA3 precipitation and ARF6 immunoblotting (**i**) and immunofluorescence of VE-cadherin (**j**). Arrow denotes less cell-surface VE-cadherin. $n \geq 3$; error bars denote s.e.m. $^{*}P < 0.05$, $^{**}P < 0.01$, $^{***}P < 0.001$.

Supplementary Fig. 5a, b)[19]. We noted that a class of ARF-GEFs, the cytohesins, is highly expressed in multiple types of endothelial cells (Supplementary Fig. 5c). Accordingly, treatment of HMVEC-d with SecinH3, a cytohesin inhibitor, significantly increased endothelial cell-surface localization of VE-cadherin (Supplementary Fig. 5d–f)[20]. Notably, SecinH3 inhibited IL-1β-induced ARF6–GTP, as well as IL-1β-induced disruption of VE-cadherin cell-surface localization and endothelial permeability (Fig. 2e–g and Supplementary Fig. 5g, h). To determine which GEF might be uniquely involved, we used siRNA to knockdown *CYTH1*, *ARNO* and *CYTH3* (coding for cytohesins 1, 2 and 3, respectively) and *GEP100* (also known as *IQSEC1*) (Supplementary Fig. 6a), and found that only siRNA targeting *ARNO* completely blocked IL-1β-induced endothelial permeability and phenocopied the knockdown of *ARF6* (Fig. 2h and Supplementary Fig. 6b). Furthermore, *ARNO* siRNA inhibited IL-1β-induced ARF6–GTP formation, IL-1β-induced disruption of VE-cadherin cell–cell contacts and IL-1β-induced internalization of surface VE-cadherin (Fig. 2i, j and Supplementary Fig. 6c, g); all of these effects were rescued by the expression of siRNA-resistant *ARNO* (Supplementary Fig. 6d–g). In cells treated with *ARNO* siRNA, viral expression of siRNA-resistant *ARNO*, but not viral expression of siRNA-resistant *ARNO(E156K)* (carrying a mutation in the Sec7 domain), rescued the disruption of IL-1β-induced ARF6–GTP formation and permeability[21] (Supplementary Fig. 6d, e). These data demonstrate that ARNO is a critical ARF-GEF necessary for IL-1β-induced activation of ARF6 and subsequent induction of vascular permeability, but does not rule out the role of other GEF family members in similar responses in different cell types or in response to different cytokines.

The signalling components in the NF-κB pathway downstream of IL-1β-induced activation of IL-1R are well characterized (Supplementary Fig. 1). Although the inhibition of the NF-κB pathway at the level of IRAK1 by siRNA did not inhibit IL-1β-induced ARF6 activation, siRNA knockdown of *MYD88* inhibited both IL-1β-induced permeability and ARF6–GTP activation, suggesting a bifurcation of

RESEARCH LETTER

IL-1β-induced signalling at the point of MYD88 (Fig. 3a–c and Supplementary Fig. 7a, b). The proposed bifurcation was further verified by the pharmacological uncoupling of the two pathway arms: although SecinH3 blunted IL-1β-induced permeability, it did not significantly inhibit IL-1β-induced NF-κB nuclear localization or NF-κB-dependent expression or localization of cell-surface adhesion molecules (Fig. 3d and Supplementary Fig. 7c, d). Furthermore, SecinH3 was unable to inhibit IL-1β-induced polymorphonuclear leukocyte rolling and adherence under shear stress on an endothelial monolayer (Supplementary Fig. 7e). Mechanistic support for this novel signalling arm was provided by the demonstration of an interaction between MYD88 and ARNO by co-immunoprecipitation in both overexpression and endogenous settings (Fig. 3e, f). Our hypothesis that ARNO is the critical GEF in IL-1β-induced permeability in endothelial cells was further strengthened by our inability to detect an interaction between MYD88 and other potentially relevant ARF-GEFs including CYTH1, CYTH3 and GEP100 (Supplementary Fig. 7f, g).

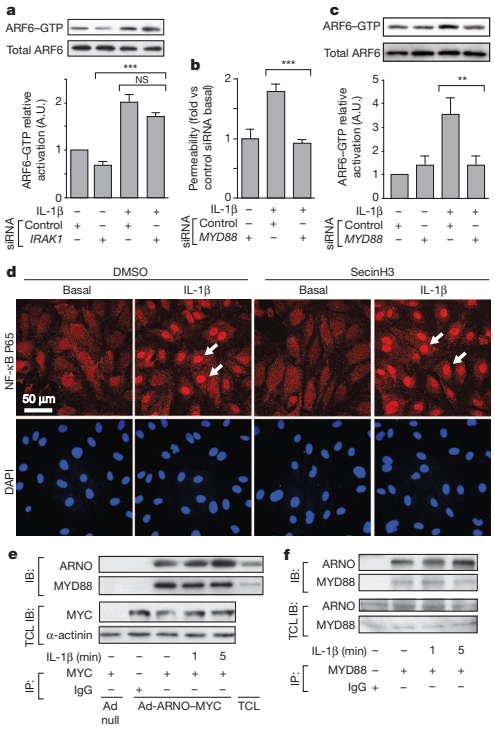

Figure 3 | The immediate IL-1β-induced permeability pathway diverges at MYD88. **a**, *IRAK1*-siRNA-treated HMVEC-d, stimulated with IL-1β, subjected to ARF6–GTP pull-down and immunoblotted for ARF6. **b**, **c**, *MYD88*-siRNA-treated HMVEC-d stimulated with IL-1β, showing permeability and ARF6 activation. **d**, NF-κB p65 (also known as RELA) immunofluorescence in HMVEC-d stimulated with IL-1β and SecinH3. Arrows denote nuclear localization. **e**, Cell lysates from Ad-ARNO–MYC-infected HMVEC-d immunoprecipitated (IP) with anti-MYC antibodies and immunoblotted with anti-MYD88 antibodies. **f**, Lysates from HMVEC-d immunoprecipitated with anti-MYD88 antibodies and immunoblotted with anti-ARNO antibodies. $n \geq 3$. Error bars denote s.e.m. $^{*}P < 0.05$, $^{**}P < 0.01$, $^{***}P < 0.001$.

An effective therapeutic strategy to combat numerous inflammatory conditions is to target pro-inflammatory cytokines proximal to the NF-κB pathway. However, this strategy can result in undesired pleiotropic effects. We wanted to know whether targeting a single arm in this pathway—the one mediated by ARNO–ARF6—could inhibit acute or chronic inflammation *in vivo* in two animal models of inflammation. The first model we tested was rheumatoid arthritis, a disease characterized by a dysregulated cytokine response causing excessive inflammation and tissue damage and treated therapeutically in humans with the anti-cytokine tumour necrosis factor receptor (TNFR)–Fc fusion protein etanercept (Enbrel)[22–25]. A standard animal model of arthritis through which a TNFR fusion approach has been proven effective is collagen-induced arthritis (CIA)[24–26]. Exposure of animals to the cytohesin inhibitor SecinH3 after the onset of CIA reduced vascular permeability in the joints, but had no effect on global cytokine levels at 24 h after treatment initiation (Fig. 4a and Supplementary Fig. 8a, b). In addition, a significant inhibition in the increase in arthritic index, comparable to that achieved by treatment with Enbrel, was observed. The arthritic index is a scoring system determined by the number of digits or joints that are oedematous or erythematous. The significance of our findings was verified by histologic scoring of inflammation, pannus development, cartilage damage and bone damage (Fig. 4c, d). A similar effect of SecinH3 was confirmed in a second model of inflammation, the carrageenan air-pouch model. Six hours after an inflammatory stimulus, a time at which substantial inflammation was induced in the positive control mice, treatment with SecinH3 decreased exudate volume as well as leukocyte concentration in the exudates (Supplementary Fig. 8c, d). Collectively, these data identify MYD88–ARNO–ARF6 as a valid target for inflammatory conditions confirming a relevant role for manipulation of this pathway *in vivo* to modulate inflammatory processes and in the treatment of disease.

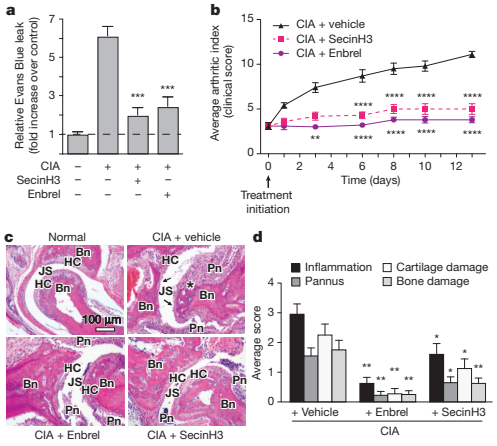

Figure 4 | Inhibition of ARF-GEFs decreases collagen-induced vascular permeability and arthritis in mice. **a**, Arthritis-induced vascular permeability in the joint measured by Evans Blue leak 7 days after treatment initiation in the presence of SecinH3 or Enbrel. $n = 14$ per group. **b**, Chronological arthritic assessment. $n = 10$ per group. Significance values are measured against CIA plus vehicle. **c**, Haematoxylin and eosin staining of sections through joints. Bn, bone; HC; hyaline cartilage; JS, joint space; Pn, inflamed pannus. Asterisk denotes cartilage and bone loss; arrows denote eroded cartilage. **d**, Summary of histological changes of inflammation, pannus, cartilage and bone damage of indicated treatment. Control, $n = 5$; Enbrel and SecinH3, $n = 10$. Error bars denote s.e.m. $^{*}P < 0.05$, $^{**}P < 0.01$, $^{***}P < 0.001$, $^{****}P < 0.0001$ versus disease group.

Chronic inflammation causes tissue destruction through dysregulated cytokine release, inflammatory cell recruitment and vascular permeability; yet each of these mechanisms has critical roles in many physiologic processes, including the immune response[5–7]. We have identified a novel pathway that uncouples cytokine effects on vascular stability from other critical functions of the canonical NF-κB transcription program (Supplementary Fig. 1). Our model suggests the potential for inhibition of vascular leak without modulation of immune-cell adhesion or other critical NF-κB-dependent responses.

The activation of many inflammatory cytokine receptors disrupts cell–cell interactions, precipitating tissue oedema and destruction[5,7,9,27]. Toll-like receptors and the interleukin receptor also use MYD88, and the mechanism described here may well apply[3,10]. Interestingly, TNFR1 (also known as TNFRSF1A) does not use MYD88 yet still activates ARF6–GTP after stimulation (Supplementary Fig. 9). Whether ARNO or another ARF-GEF binds directly to TNFR1 or its adaptor protein TRADD is unknown, as is the possibility that ARF-GEF–ARF6–cadherin serves as a common signalling module exploited by multiple cytokines. Although this study focused on the endothelium, the concept of cytokine receptor–ARF–cadherin may also apply to the epithelial barrier, which expresses these constituents and is also compromised by cytokines including IL-1β[16].

Inhibition of this novel vascular-stability pathway, which is aimed at enhancing the resilience of the host to the cytokine response, shows effects commensurate to those of class-leading drugs that target cytokines upstream of NF-κB and seek to blunt the cytokine response of the immune system outright. This approach may be particularly useful in arthritis, as the current medical therapy can render a patient immunocompromised and susceptible to reactivation of infectious disease such as tuberculosis[28]. Application of these findings to other diseases characterized by excessive acute or chronic inflammatory states, including sepsis, Crohn's disease, ulcerative colitis, scleroderma and psoriasis, should also be considered[9,29,30].

METHODS SUMMARY

Transwell permeability. HMVEC-d cells were seeded on 1.0-μm Costar transwell inserts coated with fibronectin. Cells were grown to confluency and treated with SecinH3 for 3 h or MAPK/NF-κB/transcription/translation inhibitors for 30 min followed by treatment with 10 ng ml^{-1} IL-1β. Alternatively, cells were infected with Ad-GFP or Ad-ARF6(Q67L) for 48 h. siRNA knockdown was performed as described in Supplementary Methods, and cells were treated with IL-1β 72 h after the second siRNA transfection. Two hours later, HRP was added to the top chamber at a final concentration of 100 μg ml^{-1}. Medium was removed after 60 min from the lower chamber. For time-course transwell assays and transcription/translation-inhibitor experiments (Fig. 1a, c, d), HRP was added to the insert at the same time as IL-1β. Transwell inserts were moved to fresh wells after each time point, and the concentration of HRP in the bottom chamber was measured for monolayer permeability. HRP was assessed using media samples obtained from the lower chamber incubated with 0.5 mM of guaiacol and 0.6 mM H_2O_2. Spectrophotometric analysis of absorbance at 490 nm provided a quantitative evaluation of the amount of HRP that crossed the membrane. Data are presented as mean ± s.e.m. of at least three independent experiments performed in quadruplicate.

A detailed description of all methods is provided in Supplementary Information.

Received 9 December 2011; accepted 19 September 2012.
Published online 11 November 2012.

1. Li, Q. & Verma, I. M. NF-κB regulation in the immune system. *Nature Rev. Immunol.* **2,** 725–734 (2002).
2. Collins, T. *et al.* Transcriptional regulation of endothelial cell adhesion molecules: NF-κB and cytokine-inducible enhancers. *FASEB J.* **9,** 899–909 (1995).
3. Liu, S. F. & Malik, A. B. NF-κB activation as a pathological mechanism of septic shock and inflammation. *Am. J. Physiol. Lung Cell. Mol. Physiol.* **290,** L622–L645 (2006).
4. Rothwarf, D. M. & Karin, M. The NF-κB activation pathway: a paradigm in information transfer from membrane to nucleus. *Sci. STKE* **1999,** RE1 (1999).
5. Pober, J. S. & Sessa, W. C. Evolving functions of endothelial cells in inflammation. *Nature Rev. Immunol.* **7,** 803–815 (2007).
6. Muller, W. A. Leukocyte–endothelial cell interactions in the inflammatory response. *Lab. Invest.* **82,** 521–533 (2002).
7. Royall, J. A. *et al.* Tumor necrosis factor and interleukin 1 alpha increase vascular endothelial permeability. *Am. J. Physiol. Lung Cell. Mol. Physiol.* **257,** L399–L410 (1989).
8. West, X. Z. *et al.* Oxidative stress induces angiogenesis by activating TLR2 with novel endogenous ligands. *Nature* **467,** 972–976 (2010).
9. London, N. R. *et al.* Targeting Robo4-dependent Slit signaling to survive the cytokine storm in sepsis and influenza. *Sci. Transl. Med.* **2,** 23ra19 (2010).
10. Zhu, J. & Mohan, C. Toll-like receptor signaling pathways–therapeutic opportunities. *Mediators Inflamm.* **2010,** 781235 (2010).
11. Kishore, N. *et al.* A selective IKK-2 inhibitor blocks NF-κB-dependent gene expression in interleukin-1β-stimulated synovial fibroblasts. *J. Biol. Chem.* **278,** 32861–32871 (2003).
12. Matthews, J. S. & O'Neill, L. A. Distinct roles for p42/p44 and p38 mitogen-activated protein kinases in the induction of IL-2 by IL-1. *Cytokine* **11,** 643–655 (1999).
13. Martin, M. U. & Wesche, H. Summary and comparison of the signaling mechanisms of the Toll/interleukin-1 receptor family. *Biochim. Biophys. Acta* **1592,** 265–280 (2002).
14. Kaltschmidt, B., Linker, R. A., Deng, J. & Kaltschmidt, C. Cyclooxygenase-2 is a neuronal target gene of NF-κB. *BMC Mol. Biol.* **3,** 16 (2002).
15. Funk, C. D. Prostaglandins and leukotrienes: advances in eicosanoid biology. *Science* **294,** 1871–1875 (2001).
16. Palacios, F., Price, L., Schweitzer, J., Collard, J. G. & D'Souza-Schorey, C. An essential role for ARF6-regulated membrane traffic in adherens junction turnover and epithelial cell migration. *EMBO J.* **20,** 4973–4986 (2001).
17. D'Souza-Schorey, C., Li, G., Colombo, M. I. & Stahl, P. D. A regulatory role for ARF6 in receptor-mediated endocytosis. *Science* **267,** 1175–1178 (1995).
18. Riley, K. N., Maldonado, A. E., Tellier, P., D'Souza-Schorey, C. & Herman, I. M. Betacap73–ARF6 interactions modulate cell shape and motility after injury *in vitro*. *Mol. Biol. Cell* **14,** 4155–4161 (2003).
19. Zhang, Q. *et al.* Small-molecule synergist of the Wnt/β-catenin signaling pathway. *Proc. Natl Acad. Sci. USA* **104,** 7444–7448 (2007).
20. Hafner, M. *et al.* Inhibition of cytohesins by SecinH3 leads to hepatic insulin resistance. *Nature* **444,** 941–944 (2006).
21. Béraud-Dufour, S. *et al.* A glutamic finger in the guanine nucleotide exchange factor ARNO displaces $Mg2^+$ and the β-phosphate to destabilize GDP on ARF1. *EMBO J.* **17,** 3651–3659 (1998).
22. Arend, W. P. Cytokine imbalance in the pathogenesis of rheumatoid arthritis: the role of interleukin-1 receptor antagonist. *Semin. Arthritis Rheum.* **30,** 1–6 (2001).
23. Szekanecz, Z. & Koch, A. E. Vascular involvement in rheumatic diseases: 'vascular rheumatology'. *Arthritis Res. Ther.* **10,** 224 (2008).
24. van den Berg, W. B., Joosten, L. A., Helsen, M. & van de Loo, F. A. Amelioration of established murine collagen-induced arthritis with anti-IL-1 treatment. *Clin. Exp. Immunol.* **95,** 237–243 (1994).
25. Joosten, L. A., Helsen, M. M., van de Loo, F. A. & van den Berg, W. B. Anticytokine treatment of established type II collagen-induced arthritis in DBA/1 mice. A comparative study using anti-TNFα, anti-IL-1α/β, and IL-1Ra. *Arthritis Rheum.* **39,** 797–809 (1996).
26. Wooley, P. H., Dutcher, J., Widmer, M. B. & Gillis, S. Influence of a recombinant human soluble tumor necrosis factor receptor FC fusion protein on type II collagen-induced arthritis in mice. *J. Immunol.* **151,** 6602–6607 (1993).
27. London, N. R., Whitehead, K. J. & Li, D. Y. Endogenous endothelial cell signaling systems maintain vascular stability. *Angiogenesis* **12,** 149–158 (2009).
28. Keane, J. *et al.* Tuberculosis associated with infliximab, a tumor necrosis factor α-neutralizing agent. *N. Engl. J. Med.* **345,** 1098–1104 (2001).
29. Lee, W. L. & Slutsky, A. S. Sepsis and endothelial permeability. *N. Engl. J. Med.* **363,** 689–691 (2010).
30. Silva, L. C., Ortigosa, L. C. & Benard, G. Anti-TNF-α agents in the treatment of immune-mediated inflammatory diseases: mechanisms of action and pitfalls. *Immunotherapy* **2,** 817–833 (2010).

Supplementary Information is available in the online version of the paper.

Acknowledgements We thank D. Lim and T. Mleynek for graphical assistance, G. Zimmerman and J. Kaplan for reading the manuscript, S. Odelberg for reading the manuscript and statistical analysis, J. Ling for help with immunostaining, R. Campbell and A. Weyrich for providing primary human blood cells, C. Rodesch and the University of Utah Cell Imaging/Fluorescence Facility as well as the University of Utah Flow Cytometry Facility, and M. P. Revelo for help with pathology. D.Y.L. and his laboratory were funded by grants from the National Heart, Lung, and Blood Institute; Burroughs Wellcome Fund; Juvenile Diabetes Research Foundation; NIAID Rocky Mountain Regional Center of Excellence in Biodefense and Emerging Infectious Disease; the American Asthma Foundation; and the Department of Defense. D.Y.L. is the HA and Edna Benning Endowed Professor of Medicine and Cardiology.

Author Contributions W.Z., N.R.L., C.C.G. and D.Y.L. were responsible for project conceptualization, experimental design, data analysis and manuscript preparation. W.Z., C.C.G., C.T.D., Z.T., L.K.S., D.S.S. and J.G. performed and collected data for *in vitro* experiments. N.R.L. collected data for *in vivo* experiments. C.C.G. developed software techniques for immunofluorescence analysis. M.C.P.S. performed flow cytometry experiments. Z.T. and K.R.T. made constructs and adenoviruses. A.H.G. provided histology and pathology expertise. D.Y.L. was responsible for funding the project.

Author Information Reprints and permissions information is available at www.nature.com/reprints. The authors declare competing financial interests: details are available in the online version of the paper. Readers are welcome to comment on the online version of the paper. Correspondence and requests for materials should be addressed to D.Y.L. (dean.li@u2m2.utah.edu).

SUPPLEMENTARY INFORMATION doi:10.1038/nature11603

Correction notice

Interleukin receptor activates a MYD88–ARNO–ARF6 cascade to disrupt vascular stability

Weiquan Zhu, Nyall R. London, Christopher C. Gibson, Chadwick T. Davis, Zongzhong Tong, Lise K. Sorensen, Dallas S. Shi, Jinping Guo, Matthew C. P. Smith, Allie H. Grossmann, Kirk R. Thomas & Dean Y. Li

Nature doi:10.1038/nature11603 (11 November 2012)

In the version of the Supplementary Information originally posted online, two images in Supplementary Fig. 4a were incorrect. These have been replaced in the new version of the Supplementary Information; see Supplementary Information Table of Contents for details.

SUPPLEMENTARY INFORMATION

doi:10.1038/nature11603

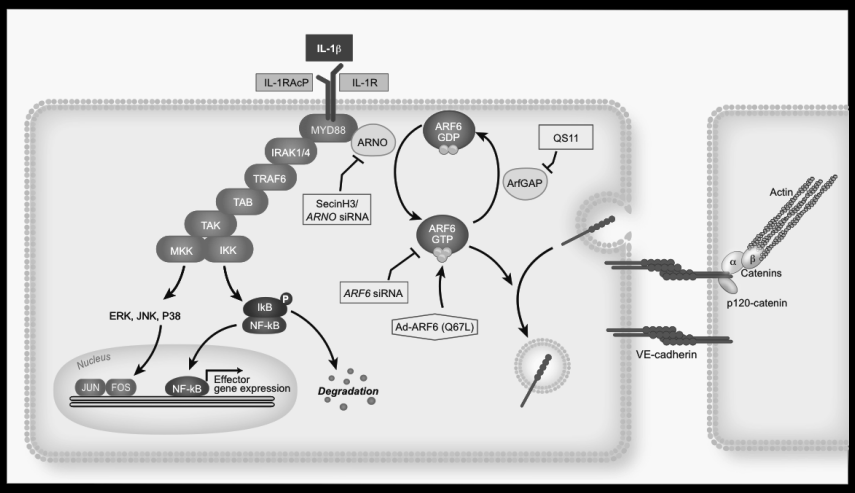

Supplementary Figure 1. Proposed IL-1β signaling pathways.
IL-1β activates NF-κB through a MYD88-IRAK-IκB-dependent pathway. MYD88 also binds to ARNO, and through a divergent pathway, enhances ARF6-GTP and decreases VE-cadherin cell surface localization.

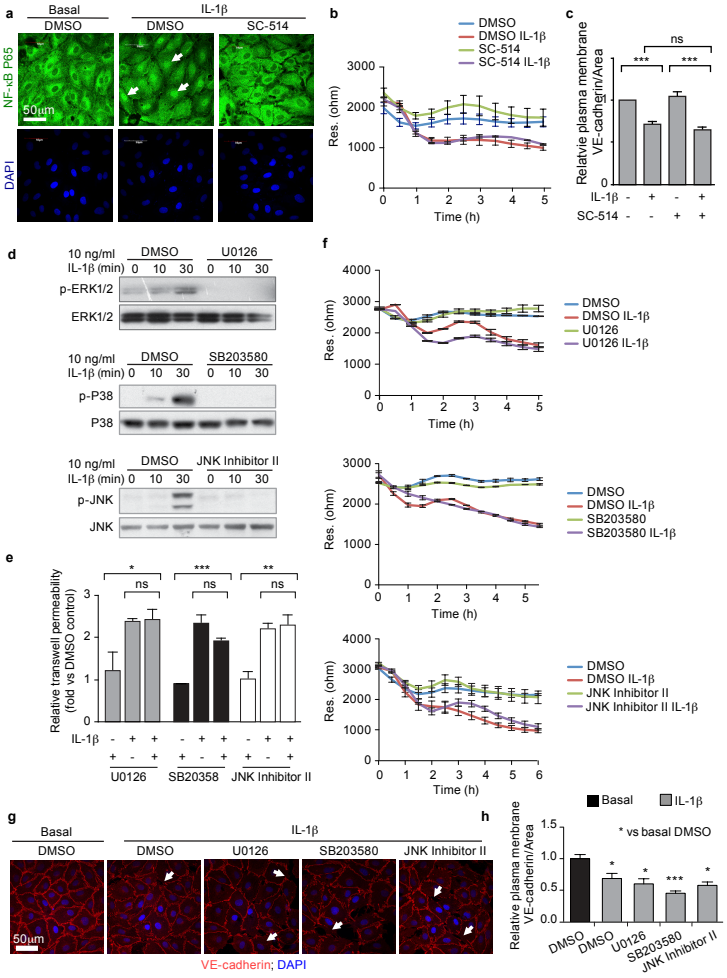

Supplementary Figure 2. IL-1β-induced permeability is independent of NF-κB, ERK1/2, JNK, and p38. **(a)** HMVEC-D cells were stimulated with IL-1β in the presence of DMSO or SC-514 and subjected to immunofluorescence for NF-κB (green). White arrows indicate nuclear NF-κB. **(b)** HMVEC-D cells were stimulated with IL-1β in the presence of DMSO or the NF-κB inhibitor, SC-514. Transendothelial resistance was measured by Electric Cell-substrate Impedance Sensing (ECIS). **(c)** Quantification of IL-1β-induced disruption of plasma membrane VE-cadherin treated with DMSO and SC-514 as shown in Figure 1c. **(d)** Lysates from HMVEC-D cells stimulated with IL-1β in the presence of DMSO, U0126, SB203580 or JNK Inhibitor II were subjected to immunoblotting for p-ERK1/2, p-P38, or p-JNK. **(e)** Transwell permeability of HMVEC-D cells stimulated with IL-1β in the presence of inhibitors of ERK1/2 (U0126), P38 (SB203580), and JNK (JNK Inhibitor II). **(f)** Transendothelial resistance was measured by ECIS in HMVEC-D cells treated with IL-1β in the presence of DMSO, ERK1/2 inhibitor U0126, P38 inhibitor SB203580, or JNK Inhibitor II in EGM2-MV complete media. **(g)** VE-cadherin immunofluorescence of HMVEC-D cells treated with IL-1β in the presence of DMSO, U0126, SB203580, or JNK Inhibitor II. White arrows indicate areas of reduced VE-cadherin surface localization. **(h)** Quantification of (g). For all experiments, N ≥ 3 and error bars represent SEM. * p<0.05, ** p<0.01, *** p<0.001.

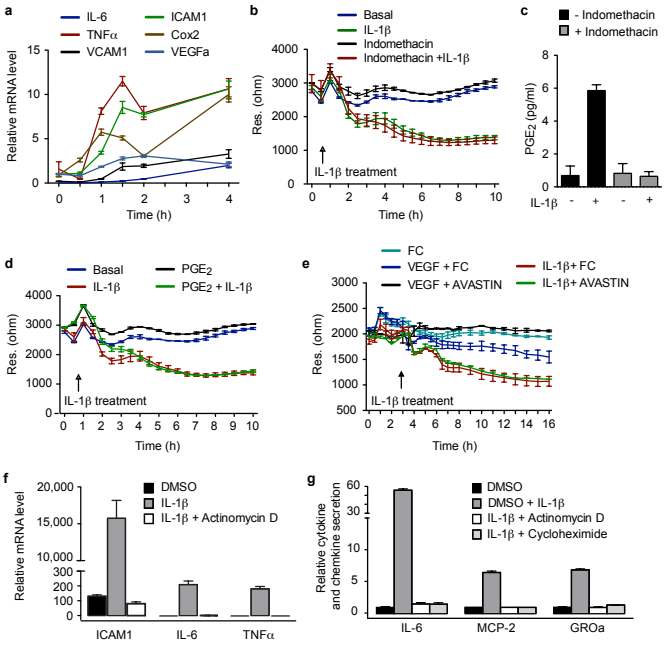

Supplementary Figure 3. IL-1β induced permeability is independent of NF-κB-transcription and its targets. **(a)** HMVEC-D cells treated with IL-1β for 0.5, 1, 1.5, 2 or 4 hours were subjected to quantitative RT-PCR to assess NF-κB target gene mRNA levels. **(b)** Transendothelial resistance was measured by ECIS in HMVEC-D cells treated with IL-1β in the presence or absence of a Cox inhibitor, Indomethacin. **(c)** Conditional media from HMVEC-D cells treated with IL-1β in the presence or absence of Indomethacin were subjected to ELISA for PGE_2. **(d)** Transendothelial resistance was measured by ECIS in HMVEC-D cells treated with IL-1β in the presence of PGE_2. **(e)** Transendothelial resistance was measured by ECIS in HMVEC-D cells treated with IL-1β or VEGF in the presence of anti-VEGF antibody (AVASTIN) or an IgG FC control. **(f)** NF-κB transcriptional targets ICAM1, IL-6 and TNFα mRNA levels were checked by quantitative RT-PCR in HMVEC-D cells treated with IL-1β in the presence or absence of Actinomycin-D. **(g)** NF-κB transcriptional targets IL-6, MCP-2 and GROa protein levels were checked in the conditioned media from HMVEC-D cells treated with IL-1β in the presence or absence of Actinomycin-D and Cycloheximide by ELISA.

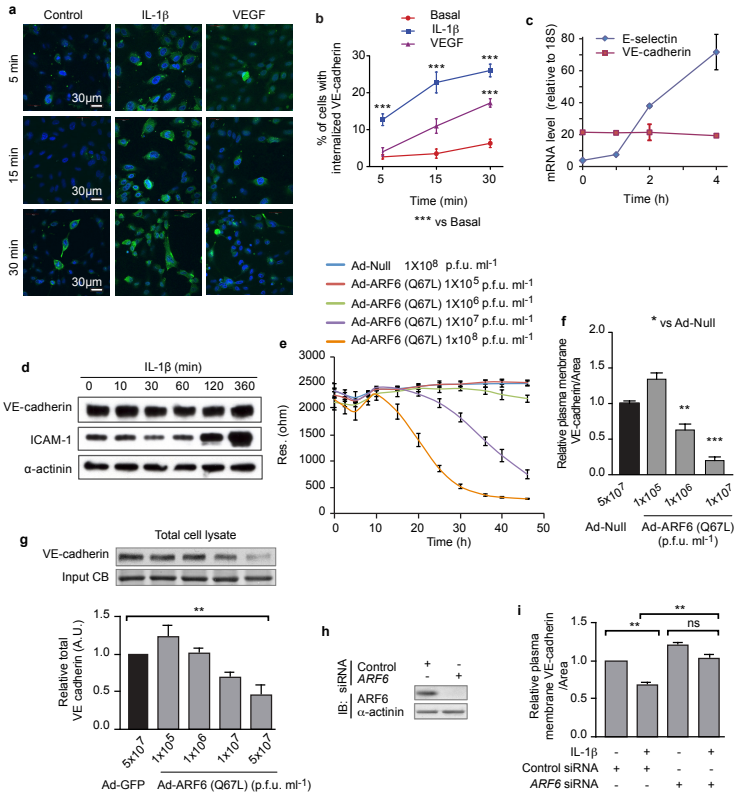

Supplementary Figure 4. ARF6 constitutive activation enhances vascular permeability.
(a) Immunofluorescence of internalized VE-cadherin (green) in IL-1β and VEGF stimulated HMVEC-D cells after 5, 15, and 30 minutes. **(b)** Quantification of VE-cadherin internalization in IL-1β and VEGF stimulated HMVEC-D cells after 5, 15, and 30 minutes. Induction of VE-cadherin internalization by IL-1 β is more rapid than that induced by VEGF. **(c)** VE-cadherin and E-selectin mRNA levels in IL-1β-stimulated HMVEC-D cells. **(d)** Lysates from IL-1β-stimulated HMVEC-D were immunoblotted with antibodies against VE-Cadherin and ICAM-1 at various time points. **(e)** HMVEC-D cells infected with Ad-Null or Ad-ARF6 (Q67L) adenovirus were assessed for transendothelial resistance by ECIS. **(f)** Quantification of Figure 2e. **(g)** Immunoblotting for VE-cadherin of cell lysates or from ARF6 (Q67L) adenoviral-vector infected HMVEC-D. **(h)** Lysates from HMVEC-D cells transfected with *ARF6* or control siRNA were immunoblotted for ARF6. **(i)** Quantification of Figure 1j. For all experiments, N ≥ 3, and error bars represent SEM. * p<0.05, ** p<0.01, *** p<0.001, **** p<0.0001.

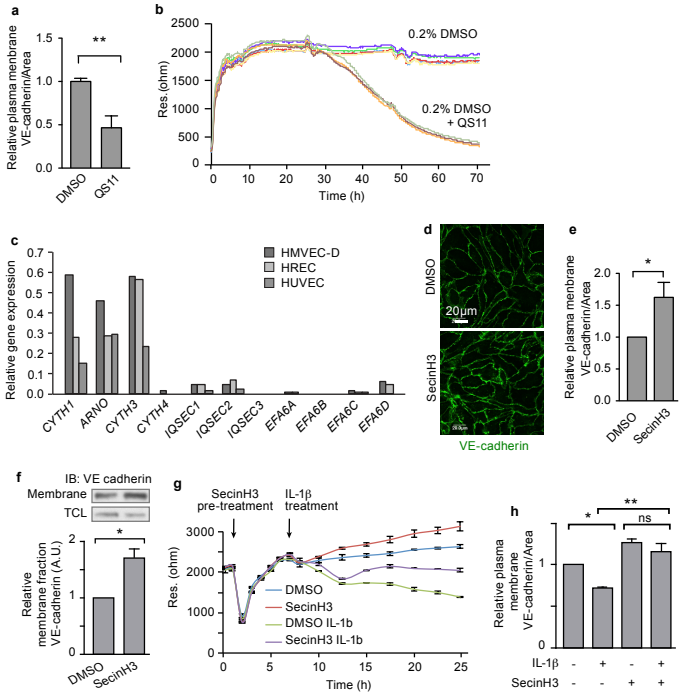

Supplementary Figure 5. Inhibition of ARF-GAPS or ARF-GEFs with small molecules decreases or increases VE-cadherin cell-surface localization respectively.
(a) Quantification of plasma membrane VE-cadherin as shown in Figure 3c. **(b)** Transendothelial resistance was measured by ECIS in HMVEC-D cells treated with DMSO or QS11. **(c)** HMVEC-D, Human retinal endothelial cells (HREC), and Human umbilical vein endothelial cells (HUVEC) were analyzed by quantitative RT-PCR for ARF-GEF, CYTH, IQSEC and EFA6 family gene expression. **(d)** HMVEC-D cells stimulated with DMSO or SecinH3 were subjected to immunofluorescence for VE-cadherin (green). **(e)** Quantification of (d). **(f)** VE-cadherin membrane fraction after treatment with SecinH3 or DMSO control. **(g)** Transendothelial resistance was measured in HMVEC-D cells stimulated with IL-1β in the presence of DMSO or SecinH3 by ECIS. **(h)** Quantification of Figure 2g. For all experiments, N ≥ 3, and error bars represent SEM. * p<0.05, ** p<0.01, *** p<0.001, **** p<0.0001.

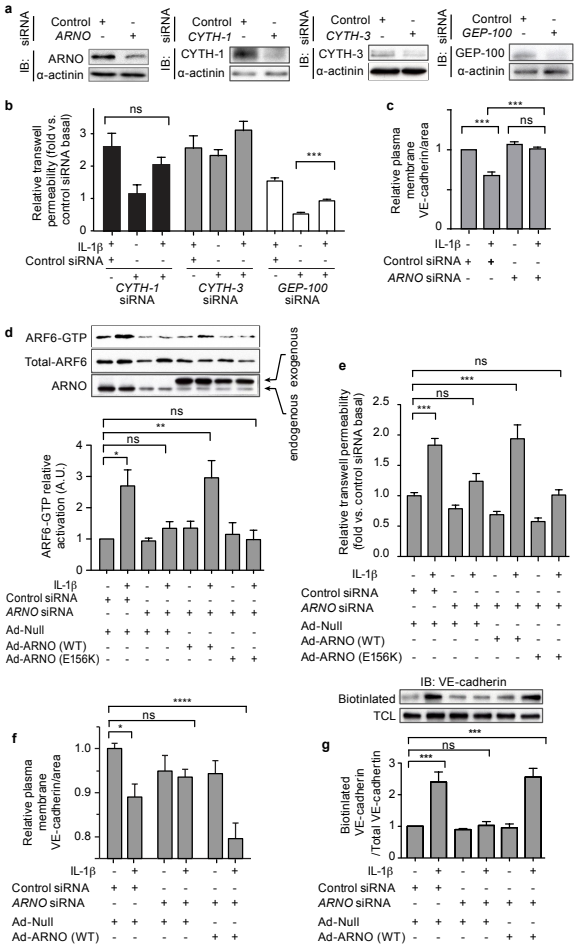

Supplementary Figure 6. The ARF-GEF ARNO/Cytohesin-2 is critical for modulating IL-1β-induced VE-cadherin localization.

(a) Lysates from HMVEC-D cells transfected with *Cytohesin-1, ARNO, Cytohesin-3, GEP-100* or control siRNA were immunoblotted for Cytohesin-1, ARNO, Cytohesin-3, or GEP-100. **(b)** Transwell permeability of *Cytohesin-1, Cytohesin-3, GEP-100* or control siRNA treated HMVEC-D stimulated with IL-1β for 2 hours. We show that loss of cytohesin-1 or cyothesin-3 have no effect in IL-1β induced permeability. Additionally, while loss of GEP-100 decreases baseline permeability, there is no effect on the fold increase in IL-1β induced permeability, suggesting that GEP-100 is regulating permeability independent of an IL-1β pathway. **(c)** Quantification of Figure 2k. **(d)** HMVEC-D treated with *ARNO* or control siRNA were stimulated with IL-1β in the presence or absence of Ad-ARNO-MYC or Ad-Null then assayed by GTP-ARF6 pulldown and immunoblotted with ARF6 antibodies. **(e)** HMVEC-D treated with *ARNO* or control siRNA were infected with Ad-Null or *ARNO* siRNA resistant Ad-ARNO-MYC, then stimulated with IL-1β and assayed by transwell permeability assay. **(f)** Quantification of cell-surface VE-cadherin in HMVEC-D treated with *ARNO* or control siRNA and infected with Ad-Null or *ARNO* siRNA resistant Ad-ARNO-MYC, then stimulated with IL-1β as in (e). **(g)** Immunoblot for biotin-labeled internalized VE-cadherin after IL-1β stimulation in conditions described in (e) and (f). For all experiments, N ≥ 3, and error bars represent SEM. * p<0.05, ** p<0.01, *** p<0.001, **** p<0.0001.

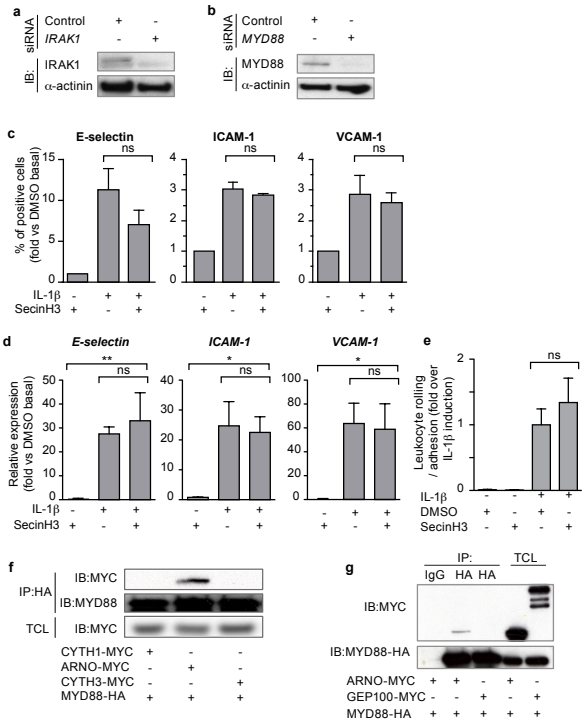

Supplementary Figure 7. The IL-1β-induced permeability pathway diverges from the canonical NF-κB pathway at MYD88.
(a) Lysates from HMVEC-D cells transfected with *IRAK1* or control siRNA were immunoblotted for IRAK1. **(b)** Lysates from HMVEC-D cells transfected with *MYD88* or control siRNA were immunoblotted for MYD88. **(c)** Fluorescence-activated cell sorting for E-selectin, ICAM-1 and VCAM-1 cell surface localization of HMVEC-D stimulated with IL-1β in the presence of DMSO or SecinH3. **(d)** Quantitative RT-PCR for *E-selectin, ICAM-1* and *VCAM-1* of HMVEC-D stimulated with IL-1β in the presence of DMSO or SecinH3. **(e)** Quantification of human polymorphonuclear leukocyte rolling and adherence to a HMVEC-D monolayer under shear stress conditions. **(f)**, **(g)** Lysates from HEK 293T cells expressing MYD88-HA and the indicated ARF-GEF-MYC constructs were immunoprecipitated with anti-HA antibodies and immunoblotted with anti-MYC antibodies. For all experiments, N ≥ 3, and error bars represent SEM. * p<0.05, ** p<0.01, *** p<0.001, **** p<0.0001.

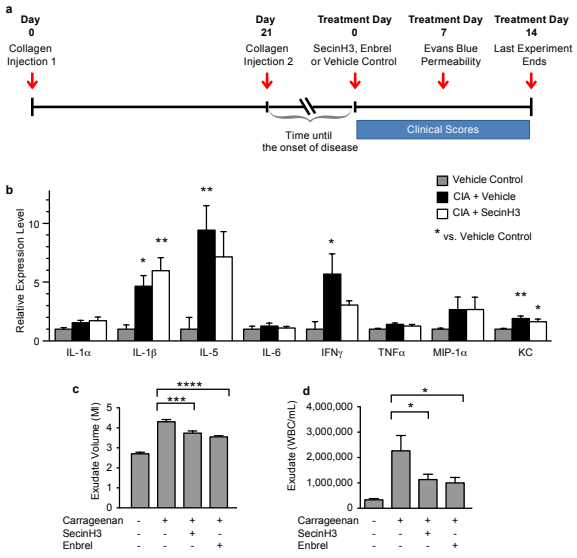

Supplementary Figure 8. The effects of SecinH3 treatment in the collagen-induced arthritis and air-pouch models.
(a) Timeline of the collagen-induced arthritis assay. Arthritis was induced by two collagen injections 21 days apart. Mice were segregated into pools and treatment with SecinH3, Enbrel, or Vehicle Control was initiated after the onset of disease. Evans Blue experiments were performed seven days after treatment initiation. Clinical scores were recorded daily from the day of treatment initiation until the experiment ended 14 days later. **(b)** Measurement of cytokine levels within arthritic joints 24 hours post treatment initiation. In an air-pouch model of acute inflammation, exudate volume **(c)**, as well as the white blood cell concentration **(d)** in the exudates was measured in the vehicle, SecinH3, or Enbrel-treated mouse six hours after inflammatory stimulus. Error bars represent SEM for 6-8 mice per group. * $p<0.05$, ** $p<0.01$, *** $p<0.001$, **** $p<0.0001$.

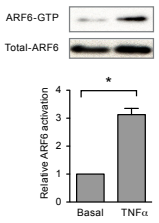

Supplementary Figure 9. TNFα activates ARF6 in endothelial cells.
HMVEC-D cells stimulated with TNFα were assayed by ARF6-GTP pull down assay and then immunoblotted with anti-ARF6 antibodies. Experiments, N=3, and error bars represent SEM. * $p<0.05$.

METHODS

Reagents

Human dermal microvascular endothelial cells (HMVEC-D) were purchased at passage 0 from Lonza and used at passages 2-6. SecinH3, ERK1/2 signal pathway inhibitor (U0126), P38 signal pathway inhibitor (SB203580), JNK signal pathway inhibitor (JNK Inhibitor II), and NF-κB signal pathway inhibitor (SC-514) were from Calbiochem. QS11 was from Sigma. Rabbit anti-VE-cadherin antibody, rabbit anti-MYD88 antibody (#3699 for western blot, #4283 for immunoprecipitation), rabbit anti-IRAK1 antibody, rabbit anti-p-ERK1/2, rabbit anti-p-P38, rabbit anti-p-JNK antibody, rabbit anti-ERK1/2, rabbit anti-P38 antibody, rabbit anti-JNK antibody and rabbit anti-NF-κB P65 antibody were from Cell Signaling. Mouse anti-ARF6 antibody was from Millipore. Mouse anti-ARNO antibody was from Abnova. *ARF6* siRNA, *ARNO* siRNA, *MYD88* siRNA and *IRAK1* siRNA were from Qiagen.

Transfection and siRNAs

siRNAs were diluted in 12.5% HiPerFect Transfection Reagent (Qiagen) in Optimem (Invitrogen) and incubated 10-20 minutes at room temperature. As siRNAs were sitting, passage 3-4 HMVEC-D cells were passaged and resuspended in EGM2-MV (Endothelial Cell Basal medium-2 supplied with EGM®-2 MV SingleQuots®, Lonza) and combined with siRNAs such that the final concentration of siRNA was 30nM (all targets). The cells were plated, allowed to grow overnight and then the growth media was replaced. Three days after the initial transfection, the cells were transfected a second time using the same HiPerFect/siRNA concentrations as above.

The following is a table of all siRNAs used, their catalogue numbers, sequence, the location within the gene the siRNA targets, and average knockdown observed by western blot.

Gene	Catalogue Number	Target sequence (5'-3')	Region	Mean knockdown
ARF6	SI02757286	CAACGTGGAGACGGTGACTTA	exon	77%
ARNO	SI00061299	CACGCTGTTGGTAATCTTATT	3' UTR	63%
Cytohesin-1	SI04217185	CGGGACAGAGGTTCCGGATAA	3' UTR	93%
Cytohesin-3	SI00061257	CAGCATGTTGTGCTCGGACAA	3' UTR	99%
MYD88	SI00300909	AACTGGAACAGACAAACTATC	exon	87%
IRAK1	SI00605262	CCGGGCAATTCAGTTTCTACA	exon	83%

Protein expression constructs

The coding sequence of full-length *MYD88* (BC023589), *ARNO* (BC038713), *CYTH-1* (BC038385), *CYTH-3* (BC028717) and *GEP100* (BC010267) were amplified by PCR from IMAGE cDNA clones and ligated into a **pcDNA3.1** vector after enzyme digestion. The ARNO, CYTH-1, CYTH-3 and GEP100 constructs contained both MYC and HIS epitopes, while the MYD88 construct contained an HA epitope.

Subcellular fractionation

Subcellular fractionation was performed as previously described[9]. Briefly, HMVEC-D cells were infected with adenovirus for 48 hours, stimulated with QS11 for 3 hours, or stimulated with SecinH3 for 2 hours. Alternatively, cells were transfected with siRNA as described above. The monolayer was washed two times with ice-cold phosphate-buffered saline (PBS) containing Ca^{2+} and Mg^{2+}, and then washed a third time with HLB buffer [Tris-HCl 10mM at pH 7.4, KCl 5mM,

protease inhibitors (Roche) and phosphatase inhibitors (Sigma), and dithiothreitol 1mM]. After the third wash, cells were homogenized in a Dounce homogenizer using 20 strokes. The homogenate was then centrifuged at 400g for 10 minutes at 4˚C. The supernatant was subjected to centrifugation again at 16,000g for 30 minutes at 4˚C. The pellet was washed with HLB buffer and resuspended in radioimmunoprecipitation assay (RIPA) buffer for 30 minutes at 4˚C. The resuspended pellet was centrifuged at 16,000g for 15 minutes at 4˚C, and the supernatant was saved as a soluble membrane fraction. To obtain the total cell lysate, an aliquot of cellular material was set aside before Dounce homogenization. RIPA buffer was added to this aliquot and then the mixture was centrifuged at 13,000g for 10 minutes at 4˚C. The resulting supernatant was saved for use as total cell lysate. Densitometry was performed on at least three independent experiments and data are presented as mean ± SEM.

ARNO Rescue Experiment

Cells (1.0×10^6 in a 10 cm dish) were first transfected with *ARNO* siRNA (SI00061299, Qiagen) at 30nM and changed to fresh media 24 hours after the transfection. The siRNA was directed against sequences in the 3' UTR of the endogenous *ARNO* mRNA. 48 hours after the media change, cells were harvested and underwent a second transfection with the same siRNA at the same dose. Cells were then infected with either an Ad-ARNO (WT) or Ad-ARNO (E156K) virus (5×10^7 p.f.u.ml^{-1}) 36 hours after the second siRNA transfection and incubated for 36 hours[2]. The adenoviral vectors expressing human ARNO (or mutant ARNO) fused to a MYC-epitope tag did not contain a 3'UTR *ARNO* sequence, and was thus predicted to be resistant to the siRNA.

ARF6-GTP pull down assay: ARF6-GTP pull-down assays were performed as described[21]. Briefly, HMVEC-D cells were pre-treated with SecinH3 for 3 hours followed by treatment with

10ng/mL IL-1β. Alternatively, cells were transfected with siRNA as described above. Cells were treated with IL-1β 72 hours after the second siRNA transfection for 5 minutes. After treatment, media was aspirated and cells were rinsed with chilled Ultrasaline. Dishes were frozen on dry ice. Following thawing, ARF6 pulldown lysis buffer [Tris-HCl 50mM, NaCl 100mM, $MgCl_2$1mM, NP-40 1%, glycerol 10%, protease inhibitors (Roche) and phosphatase inhibitors (Sigma)] were added to cells. Lysates were centrifuged and supernatants were added to GGA3-conjugated beads (Cell Biolabs, sta-40706), and agitated at 4°C for 60 minutes. Beads were washed in ARF6 pulldown lysis buffer and resuspended in 2X Laemmli prior to loading on 15% SDS-PAGE gels. A fraction of the cell lysate was withheld for use as a measure of total ARF6 in each sample. Data are presented as mean ± SEM of at least three independent experiments.

Quantitative PCR

Total RNA was extracted from cells using the RNeasy plus mini kit (Qiagen) according to manufacturer's instructions. RNA was converted to cDNA using RETROscript® kit (Ambion). Quantitative RT-PCR was performed using TaqMan probes (*CYTH1*, Hs00245092; *ARNO*, Hs00244669; *CYTH3*, Hs00188456; *CYTH4*, Hs00203581; *IQSEC1*, Hs00208333; *IQSEC2*, Hs00390333; *IQSEC3*, Hs01006522; *EFA6A*, Hs00160539; *EFA6B*, Hs00260268; *EFA6C*, Hs00209633; *EFA6D*,Hs00202892; *VEGFA*, Hs00900055; *ICAM1*, Hs00164932; *VCAM1*, Hs01003372; *IL-6*, Hs9999032; *TNFα*, Hs01113624_g1; *Cox2*, Hs00153133; *VE-cadherin*, Hs00901463; *E-selectin*, Hs00174057_m1) and the ABI Prism 7900 HT Real-Time PCR System (Applied Biosystems). Quantification was performed using a human brain cDNA standard curve and normalized to 18S rRNA. Data are presented as mean ± SEM of four duplicates from at least two independent experiments.

Immunofluorescence

10,000 HMVEC-D cells were seeded onto 8 well chamber slides coated with human fibronectin. Cells were pre-treated with small molecule inhibitors of NF-κB or MAPK for 30 minutes or SecinH3 for 3 hours followed by treatment with 10 ng/ml IL-1β for 2 hours. Alternatively, cells were infected with 1×10^{5}-1×10^{8} p.f.u.ml^{-1} of the indicated adenovirus for 48 hours. For siRNA knockdown experiments, cells were harvested 72 hours after the first siRNA transfection, re-transfected with the same siRNA a second time and seeded onto chamber slides. 72 hours after the second siRNA transfection, cells were treated with IL-1β for 2 hours. Cells were fixed, permeabilized, blocked with normal donkey serum and stained for VE-cadherin or NF-κB p65. The only exception to this protocol was for Supplementary Fig. 6f, where permeabilization was not performed in order to increase the signal of cell-surface VE-cadherin. Images are maximum-Z-projections of confocal images acquired at 0.3 μm z-section intervals. Image acquisition settings were identical for all images. Images are representative of at least 3 independent experiments. Quantification was performed using a custom Image-J macro that imported images, applied a threshold to exclude all but intensely-stained areas, and returned this area as an output. Identical threshold and size restriction values were used to analyze all images. Data are presented as mean ± SEM of at least three independent experiments.

Immunoprecipitation

Immunopreciptation assays were performed as described[9]. Briefly, HMVEC-D cells were treated with 10 ng/ml IL-1β for 1 and 5 minutes. For Figure 3e, HMVEC-D cells were infected with 1×10^{7} p.f.u.ml^{-1} Ad Null or Ad-ARNO-MYC 48 hours before IL-1β treatment. Cells were then washed with ice-cold PBS and lysed with ice-cold lysis buffer (Tris-HCl 50 mM, NaCl

250mM, NP-40 1%, and glycerol 10% with protease inhibitors and phosphatase inhibitors). Cell lysates were centrifuged for 15 minutes at 13,000g and the supernatants saved. A BCA assay (Pierce) was used to determine protein concentrations. Lysates were incubated with 8 mg of the indicated antibody and protein A/G–Sepharose (Santa Cruz Biotechnology) for 1 hour at 4°C. Beads were then washed 5 times in lysis buffer. The immunoprecipitates were assayed by western blot analysis using Peroxidase-conjugated AffiniPure Light Chain Specific secondary antibody for signal detection. Data represents at least 3 independent experiments.

Biotinylation Assay

HMVEC-D cells were transfected with *ARNO* siRNA or control siRNA and then infected with Ad null or Ad-ARNO (as described), and grown to 100% confluence on 100-mm dishes. Cells were washed with ice-cold PBS three times and labeled with EZ-link Sulfo-NHS-SS-Biotin (Thermo) at 0.5mg/ml in PBS for 30 minutes on ice. Excess Biotin was removed by washing with glycine in PBS two times on ice. The cells were then incubated with 10 ng/ml IL-1β and 0.6 mM Primaquine (MP Biomedicals) at 37°C for 30 minutes; they were then exposed to GSH buffer (Glutathione 50mM, NaOH 75mM, NaCl 75mM, EDTA 1mM, BSA 0.1%, PH 9.0) on ice for 20 minutes to remove surface biotin. GSH was then quenched by washing with 5 mg/ml iodoacetamide in PBS. After an additional wash with ice-cold PBS, cells were lysed in NP-40 buffer (Tris-HCl 50 mM, NaCl 150 mM, MgCl2 1mM, NP-40 1%, Glycerol 10%) with a protease inhibitor cocktail on ice. Cell lysates were centrifuged at 14,000 rpm for 15 minutes and supernatant was incubated with High Capacity Streptavitin Agarose Resin (Thermo) for 60 minutes at 4°C. Beads were washed with NP-40 lysis buffer three times. Bound proteins were released in 2×Laemmli buffer with 5% β-mercaptoethanol at 95°C and internalized VE-cadherin analyzed by immunoblotting with VE-cadherin antibody.

Transendothelial resistance

Transendothelial resistance was measured by Electric Cell-substrate Impedance Sensing (ECIS). An 8W10E+ electrode culture array (Applied Biophysics) was coated with 10 µg/mL human fibronectin. 5 x 10^4 HMVEC-D per well were seeded in complete media onto the electrode culture array and monitored until a stable monolayer formed. A stable monolayer was indicated by a capacitance <10 nF at 6.4 x 10^4 Hz and a stable resistance over several hours at 4 x 10^3 Hz. Cells were pre-treated with SecinH3/Avastin for 3 hours or MAPK/NF-κB inhibitors or Indomethacin or PGE_2 for 30 minutes followed by treatment with 10 ng/ml IL-1β (unless otherwise indicated). Alternatively, cells were infected with Ad-GFP or Ad-ARF6 (Q67L) adenoviruses. Resistance across the monolayer using alternating current at a frequency of 4 x 10^3 Hz was measured by 40 electrodes per well (1000-2000 cells) using the ECIS-Zθ system (Applied Biophysics) and reported in Ohms or normalized to control treatment or initial resistance. Conditioned media was collected from cells undergoing ECIS (Supplemental Figure 2e) at 16 hours after treatment with IL-1β in the presence of DMSO or inhibitors. PGE_2 concentration was calculated using the PGE_2 Express EIA kit from Cayman Chemical (500141) according to manufacturer's instructions. Data are representative of at least 3 independent experiments or represented as mean ± SEM.

Transwell permeability

HMVEC-D cells were seeded on 1.0 µm Costar transwell inserts coated with fibronectin. Cells were grown to confluency and treated with SecinH3 for 3 hours or MAPK/NF-κB/transcription/translation inhibitors for 30 minutes followed by treatment with 10ng/ml IL-1β. Alternatively, cells were infected with Ad-GFP or Ad-ARF6 (Q67L) adenovirus for 48 hours.

siRNA knockdown was performed as described and cells were treated with IL-1β 72 hours after the second siRNA transfection. Two hours later, horseradish peroxidase (HRP) was added to the top chamber at a final concentration of 100μg/ml. Medium was removed after 60 minutes from the lower chamber. For time-course transwell assays and transcription/translation inhibitor experiments (Figure 1a, d), HRP was added to the insert at the same time as IL-1β. Transwell inserts were moved to fresh wells after each timepoint, and the concentration of HRP in the bottom chamber was measured for monolayer permeability. HRP was assessed using media samples obtained from the lower chamber incubated with 0.5 mM of guaiacol and 0.6 mM H_2O_2. Spectrophotometric analysis of absorbance at 490 nm provided a quantitative evaluation of the amount of HRP that crossed the membrane. Data are presented as mean ± SEM of at least three independent experiments performed in quadruplicate.

Fluorescence-Activated Cell Sorting (FACS)

FACS was performed as decribed[31]. HMVEC-D were pre-treated with SecinH3 for 3 hours and then stimulated with 10 ng/ml IL-1β for 4 hours. Analysis of the cell surface localization of adhesion molecules was performed with one step immunofluorescence staining using anti-hE-selectin-FITC, anti-hICAM1-FITC and anti-hVCAM1-PE antibody (BD). Data are presented as mean ± SEM of at least three independent experiments.

Leukocyte Rolling and Adherence assay

3 x 10^4 HMVEC-D were seeded into each well of a fibronectin-coated parallel plate flow chamber (U-plate 0.4 VI Fibronectin, Ibidi GMBH). Media was changed daily using gentle aspiration until the cells had grown to confluence (approximately 3-5 days). Human polymorphonuclear leukocytes (PMNs) were isolated from whole blood according to previously

described protocols[32,33]. Briefly, human peripheral venous blood (500 mL) from healthy, medication-free, fasting adult subjects was drawn into acid-citrate-dextrose (1.4 mL ACD/8.6 mL blood) through standard venipuncture technique and used immediately upon collection. The University of Utah Institutional Review Board approved this study and all subjects provided informed consent. Blood was centrifuged at 150 x g for 20 minutes at 20^{o}C to separate platelet-rich plasma (PRP) from red and white blood cells (RBC/WBC). The PRP was removed and the remaining RBC/WBC mixture was resuspended in 0.9% sterile saline back to the original volume. A volume equaled to half the original blood volume of 6% Dextran 70 (Sigma-Aldrich, St. Louis, MO) was then added to the RBC/WBC mixture and left for one hour. The leukocyte-rich supernatant was removed and centrifuged at 400 x g for five minutes a 4^{o}C. The supernatant was then removed and the pellet resuspended (in 0.2% NaCl followed by an equal part of 1.6% NaCl), and the cells were centrifuged at 400 x g for five minutes at 4^{o}C. After centrifugation, the cells were resuspended in Hank's Balance Salt Solution (Sigma-Aldrich, St. Louis, MO) with 1% human serum albumin (HBSS/A) (University of Utah Hospital, Salt Lake City, UT) and layered over an equal volume of Ficoll-Paque Plus (GE Healthcare Biosciences, Piscataway, NJ). The layered cells were then centrifuged for 30 minutes at 400 x g at 4^{o}C. After 30 minutes, the mononuclear leukocyte layer was removed, followed by the RBC layer, HBSS/A layer, and Ficoll-Paque layer. The remaining pellet containing greater than 95% PMNs was washed with HBSS/A and resuspended to 1 x 10^{6} ml^{-1} in warmed ultrasaline (Lonza). Endothelial cells in parallel-plate flow chambers were pretreated with IL-1β (10 ng/mL) and/or SecinH3 for 3 hours. A syringe pump (Harvard Apparatus) was used to flow the PMN solution through the parallel plate flow chambers at 1 dynes x cm^{-1} (a typical venous shear stress). Differential Interference contrast microscopy (DIC) images were taken once per second using an Olympus inverted

microscope, and the total number of PMNs rolling and adhered in a 5 minute period were quantified using MetaMorph (Olympus) software. The data is presented as fold over IL-1β induced leukocyte rolling ± SEM and represents three independent experiments, each consisting of at least 3 replicates for each condition.

Internalization assay

VE-cadherin internalization assay was performed as previously described[9]. Briefly, HUVEC were transfected with siRNA as described above and seeded onto 8-well chambered coverglass at 5 x 10^4 cells/coverglass. After 72 hours, the culture was chilled at 4˚C for 30 minutes, surface-labeled for 60 minutes on ice with 1 ug/mL dialyzed anti-VE Cadherin antibody (clone BV6, Millipore) in ice-cold labeling buffer (3% BSA in MCDB131 medium, Invitrogen). At the end of 60 minutes, the labeling buffer was removed and the cells were treated with 0.6 mM Primaquine plus vehicle or 10 ng/mL IL-1β, DMSO vehicle or 30 μM SecinH3 or 50 μM SC-514 for 15 minutes at 37˚C and 5% CO2. Monolayers were washed 3 times over 10 minutes with ice-cold HBSS (HBSS - Hank's Balanced Salt Solution, Invitrogen) + 50mM Glycine + 3% BSA, pH 2.7 to remove surface VE-cadherin. One well for each condition was washed in a neutral pH solution to retain surface VE-cadherin staining. Subsequently, monolayers were fixed immediately in 3% paraformaldehyde for 10 minutes. The VE-cadherin antibody was detected using an Alexa-Fluor 488 conjugated anti-Mouse IgG antibody and traditional immunofluorescence methods. To image the monolayers, five images per well were randomly selected using the DAPI channel at 600x. Z-series images were taken using a confocal Olympus FV1000IX81 microscope. Each treatment was done in triplicate. The assay score represents the average percentage of total cells in each image/well/treatment containing internalized VE-Cadherin.

Collagen-induced arthritis

Collagen-induced arthritis (CIA) studies were conducted by Washington Biotechnology using their standard procedures and DBA/1J mice as previously published[34-38]. All protocols were approved by their IACUC (Institutional Animal Care and Use Committee) prior to initiation of the study. Six to seven week old male DBA/1 mice were used (Jackson Laboratories) with 5-20 animals per group. Bovine type-II collagen (Chondrex) was dissolved in 0.01 M acetic acid, and an emulsion with 50 µl of Complete Freund's Adjuvant was injected at the base of the tail at Day 0. 21 days following the first injection, a booster injection consisting of a 50 µL emulsion of collagen in Incomplete Freund's Adjuvant was injected at the base of the tail. Arthritic index (AI) was scored for each limb of an animal as follows: 0 = no visible effects of arthritis, 1 = edema and erythema of one digit or joint, 2 = edema and erythema of two joints, 3 = edema and erythema of more than 2 joints, 4 = severe arthritis of the entire paw and digits accompanied by deformity of the limb. The score for each limb was summed, with 16 as the highest possible AI score for each animal. Treatments were either vehicle (0.5% DMSO/saline IP BID), SecinH3 (0.1 mg/kg IP BID), or the positive control, Enbrel® (10 mg/kg SC OD). The experiment was repeated multiple times with different endpoints; detailed descriptions of the exact timing for each experiment follow. In all cases, treatment was initiated after mild arthritis was established (therapeutic treatment).

EVAN's BLUE DYE EXTRAVASATION: Treatment was initiated when the average arthritic index for each group was between 3.4 - 3.55 and all mice in each group demonstrated a positive arthritic index. Due to the variation in when each group reached an average arthritic index of 3.4 – 3.55, treatment initiation day varied from study day 28 (seven days after the second collagen injection) to study day 30 (nine days after the second collagen injection). The treatments lasted

for seven days until the mice were sacrificed for the Evan's Blue Dye Assay (described in detail in subsequent methods).

ARTHRITIS PROGRESSION: Treatment was initiated when the average arthritic index for each group was 3.1 and all mice in each group demonstrated a positive arthritic index. Due to the variation in when each group reached an average arthritic index of 3.1, treatment initiation day varied from study day 28 (seven days after the second collagen injection) to study day 29 (eight days after the second collagen injection). The treatments lasted for 13 days in all groups with arthritic index recorded regularly throughout.

HISTOPATHOLOGIC PATTERNS: Treatment was initiated when the average arthritic index for each group was between 3.1-3.2 and all mice in each group demonstrated a positive arthritic index. Due to the variation in when each group reached an average arthritic index of 3.1 - 3.2, treatment initiation day varied from study day 29 (eight days after the second collagen injection) to study day 33 (12 days after the second collagen injection). The treatments lasted for 14 days in all groups before joints were harvested for histology. Limbs were preserved in 10% neutral buffered formalin for histology. Limbs were decalcified in formic acid for 2-3 days, paraffin embedded, and 8 μm sections stained with toluidine blue. Arthritis severity was evaluated for inflammation, pannus, cartilage damage, and bone damage.

CYTOKINE EVALUATION: Treatment was initiated when the average arthritic index for each group was 3.4 and all mice in each group demonstrated a positive arthritic index. All groups reached an average arthritic index of 3.4 on day 34 (13 days after the second collagen injection), and treatment was initiated. The treatments lasted for 1 day, at which time plasma and ankle joints were collected for cytokine analysis (described in detail in subsequent methods).

All selection and later scoring were blinded to treatment. Data are represented as mean ± SEM.

CIA - Cytokine or chemokine array

CIA was induced as described. 24 hours after treatment of SecinH3, joints of mice were collected and pulverized using a mortar and pestle filled with liquid nitrogen. Tissue was transferred to 15 ml tubes, resuspended in 1 ml PBS and homogenized using a Polytron tissue homogenizer (*PRO* Scientific Inc. USA) for 20 s. Mouse joint homogenates were centrifuged for 10 minutes at 500 g at 4°C. Supernatants were transferred to 1.5 ml Eppendorf tubes, centrifuged at 15,000 g for 5 minutes and collected for cytokine analysis by Quansys Biosciences. Data are presented as mean ± SEM for 6 mice per condition.

CIA – Evans Blue permeability

CIA was induced as described. Seven days after randomization and treatment initiation, mice were given an IV injection of 5 ml/kg of 1% Evans Blue dye. One hour later, mice were bled and plasma collected. Mice were perfused, the hind limbs degloved, and ankle joints homogenized in 0.5 ml saline. 1.5 ml formamide was added and Evans Blue dye eluted overnight at 60°C. Supernatant and plasma samples were read spectrophotometrically and expressed as OD620-OD740 joints divided by OD620-OD740 plasma. Values were normalized to non-CIA-induced mice and expressed as fold increase over control. N=14 per group and data are represented as mean ± SEM.

Air-Pouch Model

The Carrageenan-induced Air Pouch Model was performed by Washington Biotechnology as previously described[39-41]. All protocols were approved by their IACUC (Institutional Animal

Care and Use Committee) prior to initiation of the study. Six to seven week old male Swiss-Webster mice were used (Harlan) with 6-8 animals per group. On day 0, the nape of the neck was shaved and six mL of sterile air was injected subcutaneously. On day 3, three mL of sterile air was injected subcutaneously. On days 4 and 5, mice that were to be induced at a later time were injected with either 0.1 mg/kg SecinH3 IP BID, vehicle IP BID, or 10 mg/kg Enbrel® SQ QD. On day 6 an additional injection was administered one hour prior to carrageenan injection. One mL of 3% carrageenan (FLUKA) previously prepared in de-ionized water with heat, or 1mL of saline for the sham group, was then injected into the air pouch. Four hours after carrageenan injection, the mice were anesthetized and 3mL of 10 U/mL heparinized saline was injected into the air pouch. The air pouch was gently massaged, the contents immediately removed, and the exudate volumes recorded. An aliquot of the exudate was transferred to heparin-treated microtainer tubes for differential white blood cell counting. Samples with bloody exudates were discarded from white blood cell counting.

Statistical analysis

For the majority of data, one-way ANOVA (analysis of variance) with Tukey's post-hoc test was used to assess statistical significance. A Student's t-test was used when the experiment was only composed of two groups. Two-way ANOVA with Bonferroni post-hoc test was used to assess statistical significance for data shown in Figure 4b. A *P*-value of less than 0.05 was considered statistically significant. Unless otherwise noted, P-values of less than 0.05 are denoted with a single symbol (ie. *); P-values less than 0.01 are denoted with two symbols (ie **); P-values less than 0.001 are denoted with three symbols (ie ***); P-values less than 0.0001 are denoted with four symbols (ie ****), etc.

Methods References

31 Jones, C.A. *et al.* Robo4 stabilizes the vascular network by inhibiting pathologic angiogenesis and endothelial hyperpermeability. *Nature Medicine* **14**, 448-453 (2008).

32 Zimmerman, G.A., McIntyre, T.M., & Prescott, S.M. Thrombin stimulates the adherence of neutrophils to human endothelial cells in vitro. *J. Clin Invest* **76**, 2235-2246, (1985)

33 Yost, C.C. *et al*. Activated polymorphonuclear leukocytes rapidly synthesize terinoic acid receptor-alpha: a mechanism for transltional control of transcriptional events. *J Exp Med* **200**, 671-680, (2004).

34 Zimmerman, D.H. *et al*. Cel-2000: A therapeutic vaccine for rheumatoid arthritis arrests disease development and alters serum cytokine/chemokine patterns in the bovine collagen type II induced arthritis in the DBA mouse model. *Int immunopharmacol* **10**, 412-421, (2010).

35 Zalevsky, J. *et al.* Dominant-negative inhibitors of soluble TNF attenuate experimental arthritis without suppressing innate immunity to infection. *J Immunol* **179**, 1872-1883, (2007).

36 Konda, V. R., Desai, A., Darland, G., Bland, J. S. & Tripp, M. L. META060 inhibits osteoclastogenesis and matrix metalloproteinases in vitro and reduces bone and cartilage degradation in a mouse model of rheumatoid arthritis. *Arthritis Rheum* **62**, 1683-1692, (2010).

37 Miner, J. N. *et al.* Antiinflammatory glucocorticoid receptor ligand with reduced side effects exhibits an altered protein-protein interaction profile. *Proceedings of the National Academy of Sciences of the United States of America* **104**, 19244-19249, (2007).

38 Montalban, A. G. *et al.* KR-003048, a potent, orally active inhibitor of p38 mitogen-activated protein kinase. *Eur J Pharmacol* **632**, 93-102, (2010).

39 Colville-Nash, P. & Lawrence, T. Air-pouch models of inflammation and modifications for the study of granuloma-mediated cartilage degradation. *Methods Mol Biol* **225**, 181-189, (2003).

40 Cronstein, B. N., Montesinos, M. C. & Weissmann, G. Salicylates and sulfasalazine, but not glucocorticoids, inhibit leukocyte accumulation by an adenosine-dependent mechanism that is independent of inhibition of prostaglandin synthesis and p105 of NFkappaB. *Proceedings of the National Academy of Sciences of the United States of America* **96**, 6377-6381 (1999).

41 Edwards, J. C., Sedgwick, A. D. & Willoughby, D. A. The formation of a structure with the features of synovial lining by subcutaneous injection of air: an in vivo tissue culture system. *J Pathol* **134**, 147-156, (1981).

CHAPTER 4

TARGETING VEGFR ENDOCYTOSIS TO TREAT DIABETIC RETINOPATHY

Abstract

Vascular Endothelial Growth Factor (VEGF) is important for endothelial cell proliferation and migration and signals through cognate cell surface receptor tyrosine kinases (VEGFRs). VEGF-induced VEGFR internalization is essential for signal amplification, yet the mechanisms coordinating the trafficking and intracellular signaling of VEGFR remain unknown. We show VEGF signals to VEGFR to activate ADP-Ribosylation Factor 6 (ARF6). ARF6 promotes binding of VEGFR to its co-receptor, neuropilin, internalization of the receptor, and amplification of receptor tyrosine kinase (RTK) signaling cascades. We demonstrate that endothelial specific knockout of ARF6 as well as small molecule inhibition of ARF6 dampens signaling to multiple downstream cascades including MARCKS and ERK, and mutes pathologic endothelial hyperpermeability in mouse models of diabetic retinopathy. This work demonstrates a VEGFR-neuropilin-ARF6 pathway controls VEGFR internalization and signaling and suggests a therapeutic strategy for inhibiting RTK activity by interfering with receptor endocytosis.

Introduction

Vascular Endothelial Growth Factor (VEGF) is essential to the genesis and maintenance of the vascular endothelium[1]. VEGF binding to its most recognized receptor, Vascular Endothelial Growth Factor Receptor 2 (VEGFR2), promotes endothelial cell growth and migration, driving vessel development[2]. VEGFR2 is a receptor tyrosine kinase (RTK) that upon ligand binding, dimerizes, trans-phosphorylates multiple intracellular residues[3], and triggers downstream pathways including PKC-MARCKS and RAF1-MEK1-ERK[2,4-6]. RTK signal amplification depends on receptor internalization and intracellular trafficking[7], highlighted by recent studies on the interaction between VEGFR2 and co-receptors including Neuropilin 1 (NRP1)[8-10]. Notably, loss of the cytoplasmic domain of NRP1 impairs VEGFR2 phosphorylation, and VEGFR2/NRP1 complexes formed in trans inhibit VEGFR2 internalization[11,12]. How VEGFR2 activation controls its own internalization, and thus signal amplification, is not understood.

We and others have shown that proangiogenic signaling through VEGFR2 depends upon the activity of the small GTPase, ARF6[13,14]. ARF6, like RAB and other members of the RAS superfamily, modulates the trafficking of proteins from the plasma membrane and within intracellular compartments[15,16]. Previous work from our laboratory defined a role for ARF6 in trafficking of cadherins and catenins to and from the cell surface[17,18] and led us to ask what role(s), if any, ARF6 plays in VEGFR2-coreceptor internalization and signal amplification.

RTK autoregulation of trafficking is of enormous interest to biology and medicine[19]. The pharmaceuticals, erlotinib and lapatinib, inhibit epidermal growth factor

receptors and are prescribed to treat breast cancer; bevacizumab and sunitinib, used to treat colon cancer, inhibit VEGF-mediated signaling[20,21]. The discovery that VEGF levels are elevated in vascular eye diseases informed the use of anti-VEGF agents to treat age-related macular degeneration and diabetic retinopathy. These anti-VEGF drugs block ligand and receptor interactions at the cell surface (bevacizumab) or poison RTK activity (sunitinib)[22]. Our elucidation of a pathway controlling VEGF receptor and co-receptor internalization presents a new target to interfere with RTK signaling.

Results

Human retinal microvascular endothelial cells (HRECs) grown *in vitro* respond to VEGF stimulation with phosphorylation of VEGFR2 and a two-fold increase in activated ARF6, ARF6-GTP (Fig. 4.1A, quantified in Fig. 4.S1A), as well as an increase in cell migration (a surrogate measure of angiogenesis). This migratory response can be inhibited by siRNA-mediated suppression of ARF6 expression (Fig. 4.1B and Fig. 4.S1B). ARF6 knockdown also reduces the phosphorylation of VEGFR2, MARCKS, and ERK (Fig. 4.1C, quantified in Fig. 4.S1, C to E). MARKS and ERK are important components of two divergent arms of VEGF signaling and the ability of ARF6 knockdown to affect these 2 pathways places ARF6 proximal to both.

Early steps in VEGF signaling include internalization of VEGFR2 and binding of VEGFR2 to co-receptors. The reduction of VEGF-induced VEGFR2, ERK, and MARCKS activation seen by siRNA inhibition of ARF6 were mimicked by inhibition of clathrin-dependent endocytosis (Fig. 4.1D, quantified in Fig. 4.S1, F to H), leading us to hypothesize that ARF6 is necessary for VEGFR2 internalization. Indeed, knockdown of

ARF6 in HRECs inhibited VEGF-induced VEGFR2 internalization (Fig. 4.1E).

The activation of small GTPases such as ARF6 relies upon guanine-nucleotide exchange factors (GEFs). One such GEF, GEP100, is known to be involved in RTK signaling and has been shown to bind to VEGFR2[13]. To probe its role in VEGF signaling we used siRNA to knockdown GEP100 in HRECs. Such treatment predictably decreased VEGF-induced ARF6 activation and HREC migration (Fig. 4.1, F and G, quantified in Fig. 4.S2, A and B), but also inhibited VEGFR2 internalization, as well as VEGFR2, ERK and MARCKS phosphorylation (Fig. 4.1, H and I, quantified in Fig. 4.S2, C to E).

Surprisingly we found that VEGFR2 co-immunoprecipitated with GEP100, independent of ligand binding (Fig. 4.1J). To determine the GEP100 domain required for binding to VEGFR2, individual domains to VEGFR2 was assessed by co-immunoprecipitation. The Pleckstrin Homology (PH) domain was found to be necessary for binding (Fig. 4.S2, F and G). Overexpression of this domain outcompeted endogenous GEP100 and blunted ARF6 activation, VEGF-induced VEGFR2 phosphorylation, ERK activation, and MARCKS activation in HRECs (Fig. 4.1, K and L, quantified in Fig. 4.S2, H to K). Together, these data identify the PH domain of GEP100 as a critical mediator of ARF6-induced VEGFR2 internalization and subsequent signaling.

Receptor trafficking is often enhanced through the interaction of receptors with co-receptors, and VEGFR2 has been demonstrated to utilize NRP1 in this fashion[8,10,12,23]. Knockdown of NRP1 in HRECs inhibited VEGF-stimulated migration, VEGFR2 phosphorylation, ERK activation, MARCKS activation, and VEGFR2 internalization (Fig. 4.2, A to C, quantified in Fig. 4.S3, A to D). Moreover, VEGFR2 was co-

immunoprecipitated with NRP1, an interaction that was inhibited by the knockdown of ARF6 (Fig. 4.2D, quantified in Fig. 4.S3E). These results show that NRP1 association and VEGFR2 internalization is dependent on ARF6 activation.

Excessive VEGF signaling drives aberrant angiogenesis and pathological vascular leak in eye diseases such as age-related macular degeneration and diabetic retinopathy[24]. To determine if ARF6 plays a role in these pathways *in vivo*, we examined the consequences of pathologic VEGF signaling in mice lacking *Arf6*. We first repeated the report that mice homozygous for a null-allele in *Arf6* (*Arf6* $^{-/-}$) died in utero (26), reaffirming that *Arf6* is essential to embryonic viability. We next created a conditional-null (floxed) *Arf6* allele (*Arf6*^{fl}), allowing us to generate compound heterozygous mice (*Arf6*$^{fl/-}$) carrying an endothelial specific cre driver (Tie2cre) (Fig. 4.S4A). These mice had no detectable ARF6 in aortic endothelial cells, yet appeared normal by criteria of size, fertility and behavior, showed no indication of embryonic lethality, or aberrant vessel development, and their retinal vasculature appeared normal throughout life (Fig. 4.S4B). ARF6$^{fl/-}$;Tie2Cre and control mice were given intraocular injections of saline or VEGF, and Evans blue dye extravasation from retinal vessels was quantified. As predicted, ARF6 endothelial knockout mice were less susceptible to VEGF-induced retinal vasopermeability (Fig. 4.3A).

To examine VEGF signaling in a disease state, we induced diabetic retinopathy in mice with streptozocin (STZ). Eyes from STZ-induced wildtype mice demonstrate an increase in GTP-bound ARF6 (Fig. 4.3B), corresponding to increased retinal permeability as assessed by Evans blue extravasation (Fig. 4.S4C). The collection and storage process of human samples does not permit detection of ARF6-GTP, but we were

able to assess total ARF6 protein levels in human tissue. Eyes from chronic diabetic patients showed higher levels of ARF6 than eyes from nondiabetic patients (Fig. 4.3C).

Together, these mouse and human data led us to the hypothesis that inhibition of ARF6 may provide an effective pharmacologic target for treating VEGF-mediated vascular diseases. To test this hypothesis we induced diabetes in our endothelial specific ARF6 knockouts. Mice showing glucose levels above 300 mg/dL were assessed for Evans blue dye extravasation, and as we predicted, endothelial ARF6 knockout mice were less susceptible to diabetic edema (Fig. 4.3D).

To further probe if inhibition of ARF6 activation is an effective treatment strategy for VEGF-mediated diseases, we made use of a chemically tractable, direct, reversible, and allosteric inhibitor of ARF6, NAV-2729 (Fig. 4.S4D). Treatment of cultured HRECs with NAV-2729 resulted in a reduction in the intracellular levels of the active, GTP-bound form of ARF6 (Fig. 4.3E), blocked VEGF-induced VEGFR2 auto phosphorylation (Fig. 4.3F), and inhibited VEGF-induced migration of HRECs (Fig. 4.3G).

To test the utility of using NAV-2729 to inhibit VEGF-induced retinal hyperpermeability *in vivo,* we first gave intraocular injections of saline+DMSO or VEGF+DMSO and measured Evans blue dye extravasation from retinal vessels. VEGF treatment caused a 3-fold increase in dye extravasation that was completely abolished by the clinically used VEGF-inhibitor, Avastin. NAV-2729 similarly reduced VEGF-induced permeability, while the negative control, DMSO did not (Fig. 4.3H). These data strongly suggest that NAV-2729 is an effective inhibitor of VEGF signaling *in vivo*.

To examine VEGF signaling in a disease state, we again induced diabetic retinopathy with STZ. Diabetic mice were treated with intraocular injections of DMSO,

NAV-2729, or SU4312 (a receptor tyrosine kinase inhibitor). Mice treated with DMSO demonstrated vessel hyperpermeability, and this response was blunted in animals treated with SU4312 or NAV-2729 (Fig. 4.3I).

Discussion

The internalization and subsequent trafficking of cell-surface receptors is well documented as a modulator of signal transduction. Although first characterized as a means of signal attenuation, current research, focused especially on the VEGFR, has shown the importance of receptor endocytosis in signal amplification[25,26]. In this manuscript we have identified a key mediator of this process, the small GTPase, ARF6. Using biochemical and cell biological assays, small molecule inhibition, and mouse genetics, we have demonstrated that VEGF activates VEGFR internalization and signaling via a VEGFR-neuropilin-GEP-100-ARF6 protein interaction cascade. Our study showing the efficacy of targeting this cascade in an animal model of diabetic retinopathy not only provides support for this signaling model, but also identifies a potential therapeutic strategy for blunting RTK signaling in disease.

Though this study is framed around VEGFR and the treatment of diabetic retinopathy, it should be viewed in a wider context. Other members of the RAS superfamily linked to pathways in which receptor internalization is important for signal amplification deserve investigation, as do other diseases where inhibition of RTK has been shown to have therapeutic promise. The use of retinal endothelial cells was fundamental for studying VEGF signaling in retinal vascular disease, but this new pathway needs to be explored in the context of other cell types [20,21]. Perhaps this

discrepancy in cell type is why we did not find ERK phosphorylation to be independent of ARF6 as previously reported [13,27].

The genetic and small molecule probes we have generated can be similarly used to interrogate other signaling pathways characterized by receptor internalization. Should Arf6 be involved in EGF signaling, for example, these tools could help resolve the controversy over whether EGFR internalization results in signal amplification or receptor down regulation[25,28-30]. Furthermore, given the benefits of RTK-inhibition in cancer therapy, the relevance of our model in oncogenesis should also be probed. The tools described here--a tissue-specific null allele of Arf6 and a high-affinity reversible inhibitor of ARF-- will be critical for these future studies. In addition, though we believe our chemical probe, NAV-2729, targets endothelial ARF6, as demonstrated by similar reductions in STZ-induced retinal vasopermeability using compounds and using conditional knockout mice, NAV-2729 may also target other cells and other pathways. Further investigation into the global role of ARF6 is thus needed especially using genetic ablation postembryonically.

The identification of ARF6 and its role in early stages of intracellular signaling unites our understanding of the inherent role of ARF6 in intracellular trafficking with the discovery that receptor endocytosis is essential for signal amplification. Though further work is required to advance our understanding of both receptor-mediated endocytosis and ARF6 itself, we demonstrate a pathway and a therapeutic strategy for inhibiting RTK activity by interfering with receptor endocytosis.

Materials and Methods

Reagents: Human Retinal Endothelial Cells (HRECs) at passage 0 from Cell Systems were cultured with EGM-2 MV (Endothelial Cell Basal medium-2 supplied with EGM®-2 MV SingleQuotes®, Lonza). Rabbit anti-p-ERK1/2 antibody, rabbit anti-VEGFR2 antibody, rabbit anti-VEGFR2 pY1175, rabbit anti-pMARCKS, rabbit anti-Caveolin, rabbit anti-Clathrin rabbit anti-MARCKS, rabbit anti-VEGFR 2 antibody (Sepharose Bead® Conjugate), and mouse anti-ERK were from Cell Signaling. Mouse anti-ARF6 antibody was from Millipore or Cell Biolabs, mouse anti-VEGFR2 was from R&D, goat anti-NRP1 antibody was from Santa Cruz, and rabbit anti-GEP100 antibodies were from Sigma. siRNA were from Qiagen. ARF6-GTP pull-down kits were from Thermo Scientific, VEGF-165 were from R&D, and the ChemoTx system for monitoring cell migration were from Neuroprobe. Standard molecular biology and cell culture reagents were primarily from Life Technologies and NAV-2729 was from Navigen LLC.

Human Samples: Human donor eyes were purchased from the Lions Eye Bank at the University of Utah. Tissue from 10 different donors was analyzed. The donor ages varied between 52 and 84. The interval between death and tissue processing varied between 6 and 12 hours. The records received from the eye bank stated the donor eyes as diabetic and nondiabetic. The western analysis is exempt of IRB approval.

Transfection and siRNAs: siRNAs were diluted in 12.5% HiPerFect Transfection Reagent (Qiagen) in Optimem (Invitrogen) and incubated 10-20 minutes at room temperature. Passage 3-4 HREC cells were resuspended in EGM2-MV and combined with siRNAs such that the final concentration of siRNA was 30 nM (all targets). The cells were plated, allowed to grow overnight, and then the growth media was replaced.

Three days after the initial transfection, the cells were transfected a second time using the same HiPerFect/siRNA concentrations as above.

The following is a list of all siRNAs used, their catalogue numbers and sequences: Allstars Negative Control siRNA, SI02757286 (CAACGTGGAGACGGTGACTTA), SI03019408 (CTGAAGGGTAGCAGTAATGAA), SI00057114 (CAGATTATCCTTG-CTCTGGAA). All siRNAs were purchased from Qiagen. We have used most of these previously in another publication[18]. The average knockdown was observed by western blot and quantified in Supplementary Figures 4.1 and 4.2.

Protein Expression Constructs: The coding sequences of each functional domain or full-length GEP100 (BC010267) were amplified from an IMAGE cDNA clone by PCR. The PCR products were ligated into pcDNA3.1 vector after Acc65I and NotI enzyme digestion. Constructs were confirmed by DNA sequencing. All constructs were fused at the C-terminus with the HA epitope.

ARF6-GTP Pull-Down Assay: ARF6-GTP pull-down assays were performed as described[18]. Briefly, HREC cells were untreated or transfected with siRNA as described above. Cells were treated with VEGF (20ng/ml) for 5-minutes 72 hours after the second siRNA transfection for 5 minutes. For assessing the effects of small molecule compounds on the intracellular levels of active ARF6, HRECs were grown on EGM2-MV medium in 6-well tissue culture plates to 80-90% confluency and exposed to test compounds (25μM) in basal EBM-2 medium supplemented with 1% FBS for 3.5 hours. After treatment, media was aspirated and cells were rinsed with chilled Ultrasaline (Lonza). Dishes were frozen on dry ice. Following thawing, ARF6 pull-down lysis buffer [Tris-HCL] 50mM, NaCl 100mM, $MgCl_2$ 1mM, NP-40 1% glycerol 10% protease inhibitors (Roche) and

phosphatase inhibitors (Sigma)] was added to cells. Lysates were centrifuged and supernatants were added to GGA3-conjugated beads (Cell Biolabs, sta-40706), and agitated at 4°C for 60 minutes. Beads were washed in ARF6 pull-down lysis buffer and resuspended in 2X Laemmli buffer prior to loading on 15% SDS-PAGE gels. A fraction of the cell lysate was withheld for use as a measure of total ARF6 in each sample.

Migration Assay: HREC cells were grown under standard conditions with EGM-2 MV and incubated in EBM-2 with 0.1% fatty acid-free BSA (Equitech-Bio, Inc) overnight. Cells were then harvested with Trypsin/EDTA (PromoCell) and resuspended at 0.6 x 10^5 cells / ml. 20ng/ml VEGF was placed in the lower wells of a 48-well chemotaxis chamber (Neuroprobe). A fibronectin-coated (overnight at 4°C) polycarbonate membrane (10 mm; Neuroprobe) was placed between the chemo attractant and the cells. HREC cells (50 µl, 30,000 cells) were added to the upper wells. After incubating at 37°C for 2 hours, cells on the top surface of the filter were removed with q-tips and cells that had migrated through the filter onto the undersurface were fixed and stained using Diff-Quik stain set (Dade Behring). Migrated cells in five high-power fields were counted and migration was expressed as the percent of cells migrated relative to cells migrated toward EBM-2 media containing 0.1% fatty acid-free BSA and no VEGF. Data are presented as s.e.m. of at least three independent experiments.

Chemotactic Cell Migration Assay: Pharmacologic effects on VEGF-induced motile activity of HRECs was assessed using 96-well-based ChemoTx system (NeuroProbe) designed for monitoring migration of cells across a polycarbonate membrane along a gradient of chemoattractant[31] The basal medium EBM-2 used for this test was supplemented with ascorbic acid (1 µg/ml) and hydrocortisone (0.2 µg/ml). Both

polycarbonate membrane filters (pore size of 8 μm) and wells of the bottom (cell collector) plates were precoated with fibronectin. The 45-μl aliquots of a suspension of serum-starved cells in EBM-2 containing 0.1% BSA ($8x10^5$ cells per ml) were pipetted on the top of the membrane filter, which was assembled on the top of collector plate. The wells of the latter were filled with EBM-2 supplemented with 0.9% FBS (30 μl per well). Each test compound at a desired concentration or DMSO control was added to the matched samples on top of the membrane and in the bottom plate. Each fully assembled ChemoTx system was incubated in a tissue culture incubator overnight followed by aspiration of media from top of the membrane, cell staining on both sides of the membrane using CyQUANT dye (Life Technologies), and removal of nonmigrated cells from the top of the membrane by wiping and rinsing. Finally, the stained migrated cells were quantified fluorometrically using a Synergy 4 plate reader with the excitation and emission wavelength settings of 485 nm and 528 nm, respectively.

Internalization Assay: VEGFR2 internalization assay was performed as previously described[18,32,33]. Briefly, HRECs were transfected with siRNA as described above and seeded onto 8-well chambered coverglass at 3 x 10^4cells/coverglass. The cells were immediately re-transfected with siRNA for 24 hours. Before assaying, the cells were serum-starved for 4 hours in EBM-2 + 0.1%fatty acid-free BSA (Equitech) and blocked in 2% FAF BSA+4% normal donkey serum, prepared in Assay Buffer (EBM-2+0.25mM HEPES, pH7.8) for 10 minutes. Purified VEGFR2 antibodies were then fed at 8μg/ml in warmed Assay Buffer for 20 minutes. The monolayers were washed twice in warmed HBSS+Ca+Mg and then stimulated in Assay Buffer with 20ng/ml VEGF165 for 1 minute at 37˚C and 5% CO2 in the presence of 0.6mM Primaquine (Sigma).

Monolayers were then washed 3 times over 7 minutes with ice-cold Hank's Balanced Salt Solution (HBSS, Invitrogen) + 50mM Glycine + 3% BSA, pH 2.7 to remove surface VEGFR2. Monolayers were subsequently fixed in 4% paraformaldehyde for 10 minutes. VEGFR2 was detected using 10 μg/ml Donkey anti-mouse IgG Alexa 488 (VEGFR2) applied for 1 hour at room temperature. Wells were washed 3x in HBSS+Ca+Mg, and mounted in 1 μg/ml DAPI in Glycerol + 0. 25μg DABCO, 0.02% sodium azide. 15 Z-stacked images were collected per condition (5 images/well x 2 wells/treatement) at 1200x oil immersion on an Olympus FV1000 confocal laser microscope. VEGFR2 internalization was scored by taking the percentage of VEGFR2 vesicle-positive cells present per frame of cells imaged. Internalization was specifically defined by the presence of 10 or more Alexa 488-labeled vesicles per cell.

Immunoprecipitation: Immunoprecipitation assays were performed as described[33]. Briefly, HREC cells were treated with 20ng/ml VEGF for 1 or 5 minutes. Cells were then washed with ice-cold PBS and lysed with ice-cold lysis buffer (Tris-HCL 50mM, NaCl 250mM, NP-40 1%, glycerol 10% with protease and phosphatase inhibitors (Thermo Science). Cell lysates were centrifuged for 15 minutes at 13,000g and the supernatants saved. BCA assays (Pierce) were used to determine protein concentrations. Lysates were precleaned with protein A/G-Sepharose (Santa Cruz Biotechnology) for 2 hour at 4˚C. Precleaned lysates were incubated with 8 mg of the indicated antibody and protein A/G-Sepharose (Santa Cruz Biotechnology) for 1 hour at 4˚C. Beads were then washed 5x in lysis buffer. The immunoprecipitates were assayed by western blot analysis using Peroxidase-conjugated AffiniPure Light Chain Specific secondary antibody for signal detection.

Animals: The Institutional Animal Care and Use Committee at the University of Utah approved the mouse studies (IACUC nos. 14-09002 and 11-12007). The Arf6 gene was mutated by homologous recombination in mouse embryo-derived stem(ES) cells. Two alleles were generated. The conditional (fl) allele contains one loxP site 5' of the Arf6 gene at position 69,371,642 (UCSC genome browser) on Chromosome 12, and a second loxP site 3' of the Arf6 open reading frame at position 67,373,928. The null (-) allele was generated by deleting the sequences between the two loxP sites by Cre-mediated recombination using HPRTcre (Jackson). Endothelial specific knockout of ARF6 was achieved by crossing $ARF6^{fl/fl}$ mice with Tie2cre mice (Jackson).

Retinal Permeability: Retinal permeability was assessed as previously described[34-36]. In brief, 8-10-week-old mice were anesthetized with ketamine-xylazine (0.2 mg/g) and then given intraocular injections of 1μl of 50ng VEGF-165 (R&D Systems) with 50ng SU4312 or NAV-2729. An equivalent volume of VEGF in 100% DMSO was injected into the eyes of control animals. Half an hour later, 50μl of 60mg/ml Evans blue solution (Sigma) in Ultrasaline was administered into the tail vein. After 5 hours, mice were killed and eyes were enucleated and retinas dissected. Dye was eluted in 0.4 ml formamide for 18 h at 70℃. The extract was centrifuged for 14,000rpm for 5 min. Absorbance at 620 nm was measured. Background absorbance was measured at 740 nm and subtracted out. Data are presented as mean ± s.e.m. of 2-4 mice per genotype.

STZ-induced Diabetic Retinopathy. Diabetic retinopathy was induced as previously described[34]. Briefly, for five consecutive days, 6-8 week old CD1 mice (Charles River) were fasted for 4 hours and then injected I.P. with either 75 mg/kg of streptazocin (Sigma-Aldrich) in sodium citrate buffer or sodium citrate buffer control. After 4 weeks,

tail-snip blood glucose was determined by glucometer (Aviva) to verify hyperglycemia (blood glucose concentrations greater than 300 mg/dL) in the STZ-treated animals. The animals were then divided into treatment groups such that body weight and blood glucose were distributed similarly among groups. Retinal permeability was assessed as explained above.

Statistical Analysis: All quantifications for western blots are in the supplementary materials. For the majority of data, one-way ANOVA (analysis of variance) with Tukey's post-hoc test was used to assess statistical significance. A Student's t-test was used when the experiment was only composed of two groups. Welch's ANOVA with Games-Howell multiple comparison test was used to assess statistical significance for data down in Figure 4.4B. A P-value of less than 0.05 was considered statistically significant. Unless otherwise noted, P-values of less than 0.05 are denoted with a single asterisk (i.e. *); P-values less than 0.01 are denoted with two asterisks (i.e. **); P-values less than 0.001 are denoted with three asterisks (i.e. ***); P-values less than 0.0001 are denoted with four asterisks (i.e. ****).

References

1. Coultas, L., Chawengsaksophak, K. & Rossant, J. Endothelial cells and VEGF in vascular development. *Nature* **438**, 937-945 (2005).

2. Olsson, A.K., Dimberg, A., Kreuger, J. & Claesson-Welsh, L. VEGF receptor signalling - in control of vascular function. *Nature reviews. Molecular cell biology* **7**, 359-371 (2006).

3. Lemmon, M.A. & Schlessinger, J. Cell signaling by receptor tyrosine kinases. *Cell* **141**, 1117-1134 (2010).

4. Veikkola, T., Karkkainen, M., Claesson-Welsh, L. & Alitalo, K. Regulation of angiogenesis via vascular endothelial growth factor receptors. *Cancer research*

60, 203-212 (2000).

5. Ferrara, N. Vascular endothelial growth factor: basic science and clinical progress. *Endocrine reviews* **25**, 581-611 (2004).

6. Meyer, R.D., Sacks, D.B. & Rahimi, N. IQGAP1-dependent signaling pathway regulates endothelial cell proliferation and angiogenesis. *PloS one* **3**, e3848 (2008).

7. Lanahan, A.A.*, et al.* VEGF receptor 2 endocytic trafficking regulates arterial morphogenesis. *Developmental cell* **18**, 713-724 (2010).

8. Evans, I.M.*, et al.* Neuropilin-1 signaling through p130Cas tyrosine phosphorylation is essential for growth factor-dependent migration of glioma and endothelial cells. *Molecular and cellular biology* **31**, 1174-1185 (2011).

9. Beck, B.*, et al.* A vascular niche and a VEGF-Nrp1 loop regulate the initiation and stemness of skin tumours. *Nature* **478**, 399-403 (2011).

10. Herzog, B., Pellet-Many, C., Britton, G., Hartzoulakis, B. & Zachary, I.C. VEGF binding to NRP1 is essential for VEGF stimulation of endothelial cell migration, complex formation between NRP1 and VEGFR2, and signaling via FAK Tyr407 phosphorylation. *Molecular biology of the cell* **22**, 2766-2776 (2011).

11. Lanahan, A.*, et al.* The neuropilin 1 cytoplasmic domain is required for VEGF-A-dependent arteriogenesis. *Developmental cell* **25**, 156-168 (2013).

12. Koch, S.*, et al.* NRP1 presented in trans to the endothelium arrests VEGFR2 endocytosis, preventing angiogenic signaling and tumor initiation. *Developmental cell* **28**, 633-646 (2014).

13. Hashimoto, A.*, et al.* GEP100-Arf6-AMAP1-cortactin pathway frequently used in cancer invasion is activated by VEGFR2 to promote angiogenesis. *PloS one* **6**, e23359 (2011).

14. Jones, C.A.*, et al.* Slit2-Robo4 signalling promotes vascular stability by blocking Arf6 activity. *Nature cell biology* **11**, 1325-1331 (2009).

15. Molendijk, A.J., Ruperti, B. & Palme, K. Small GTPases in vesicle trafficking. *Current opinion in plant biology* **7**, 694-700 (2004).

16. Schweitzer, J.K., Sedgwick, A.E. & D'Souza-Schorey, C. ARF6-mediated endocytic recycling impacts cell movement, cell division and lipid homeostasis. *Seminars in cell & developmental biology* **22**, 39-47 (2011).

17. Grossmann, A.H.*, et al.* The small GTPase ARF6 stimulates beta-catenin

transcriptional activity during WNT5A-mediated melanoma invasion and metastasis. *Science signaling* **6**, ra14 (2013).

18. Zhu, W.*, et al.* Interleukin receptor activates a MYD88-ARNO-ARF6 cascade to disrupt vascular stability. *Nature* **492**, 252-255 (2012).

19. Brunelleschi, S., Penengo, L., Santoro, M.M. & Gaudino, G. Receptor tyrosine kinases as target for anti-cancer therapy. *Current pharmaceutical design* **8**, 1959-1972 (2002).

20. Flynn, J.F., Wong, C. & Wu, J.M. Anti-EGFR Therapy: Mechanism and Advances in Clinical Efficacy in Breast Cancer. *Journal of oncology* **2009**, 526963 (2009).

21. Ortega, J., Vigil, C.E. & Chodkiewicz, C. Current progress in targeted therapy for colorectal cancer. *Cancer control : journal of the Moffitt Cancer Center* **17**, 7-15 (2010).

22. Alfaro, C.*, et al.* Influence of bevacizumab, sunitinib and sorafenib as single agents or in combination on the inhibitory effects of VEGF on human dendritic cell differentiation from monocytes. *British journal of cancer* **100**, 1111-1119 (2009).

23. Ballmer-Hofer, K., Andersson, A.E., Ratcliffe, L.E. & Berger, P. Neuropilin-1 promotes VEGFR-2 trafficking through Rab11 vesicles thereby specifying signal output. *Blood* **118**, 816-826 (2011).

24. Penn, J.S.*, et al.* Vascular endothelial growth factor in eye disease. *Progress in retinal and eye research* **27**, 331-371 (2008).

25. Miaczynska, M., Pelkmans, L. & Zerial, M. Not just a sink: endosomes in control of signal transduction. *Current opinion in cell biology* **16**, 400-406 (2004).

26. Simons, M. An inside view: VEGF receptor trafficking and signaling. *Physiology* **27**, 213-222 (2012).

27. Ikeda, S.*, et al.* Novel role of ARF6 in vascular endothelial growth factor-induced signaling and angiogenesis. *Circulation research* **96**, 467-475 (2005).

28. Cosker, K.E. & Segal, R.A. Neuronal signaling through endocytosis. *Cold Spring Harbor perspectives in biology* **6**(2014).

29. Hsu, H., Baldwin, C.L. & Telfer, J.C. The Endocytosis and Signaling of the gammadelta T Cell Coreceptor WC1 Are Regulated by a Dileucine Motif. *Journal of immunology* (2015).

30. Sousa, L.P.*, et al.* Suppression of EGFR endocytosis by dynamin depletion reveals that EGFR signaling occurs primarily at the plasma membrane. *Proceedings of the National Academy of Sciences of the United States of America* **109**, 4419-4424 (2012).

31. Frevert, C.W., Wong, V.A., Goodman, R.B., Goodwin, R. & Martin, T.R. Rapid fluorescence-based measurement of neutrophil migration in vitro. *Journal of immunological methods* **213**, 41-52 (1998).

32. Sawamiphak, S.*, et al.* Ephrin-B2 regulates VEGFR2 function in developmental and tumour angiogenesis. *Nature* **465**, 487-491 (2010).

33. London, N.R.*, et al.* Targeting Robo4-dependent Slit signaling to survive the cytokine storm in sepsis and influenza. *Science translational medicine* **2**, 23ra19 (2010).

34. Scheppke, L.*, et al.* Retinal vascular permeability suppression by topical application of a novel VEGFR2/Src kinase inhibitor in mice and rabbits. *The Journal of clinical investigation* **118**, 2337-2346 (2008).

35. Maharjan, S.*, et al.* Sac-0601 prevents retinal vascular leakage in a mouse model of diabetic retinopathy. *European journal of pharmacology* **657**, 35-40 (2011).

36. Kim, J.H., Kim, J.H., Yu, Y.S., Cho, C.S. & Kim, K.W. Blockade of angiotensin II attenuates VEGF-mediated blood-retinal barrier breakdown in diabetic retinopathy. *Journal of cerebral blood flow and metabolism : official journal of the International Society of Cerebral Blood Flow and Metabolism* **29**, 621-628 (2009).

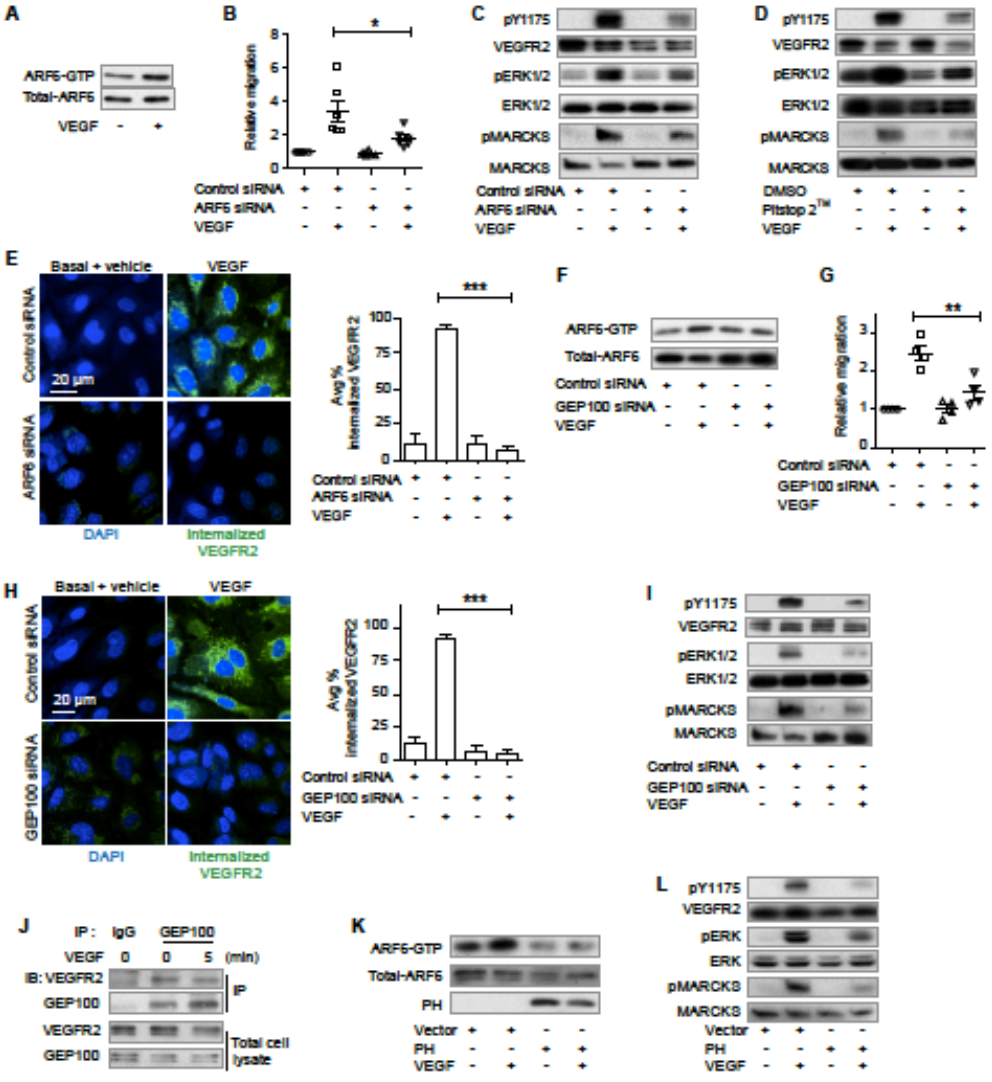

Fig. 4.1. Immediate VEGF signaling is ARF6 dependent. (**A)** VEGF-treated HREC assayed for ARF6-GTP**.** (**B to C**), ARF6-siRNA-treated HRECs assayed for migration (**B**), and VEGFR2, ERK1/2, MARCKS phosphorylation (**C**). (**D**) Pitstop2™-treated HRECs assayed for VEGFR2, ERK1/2, and MARCKS phosphorylation. (**E**)**,** Immunofluorescent localization of internalized VEGFR2 in ARF6-siRNA-treated HRECs. (**F to I**), GEP100-siRNA-treated HRECs assayed for ARF6-GTP levels (**F**), migration (**G**), internalized VEGFR2 (**H**), and VEGFR2, ERK1/2, and MARCKS phosphorylation (**I**). (**J**) HREC cell lysates immunoprecipitated with anti-GEP100 and immunoblotted with anti-VEGFR2 and anti-GEP100. (**K to L**), HRECs transfected with GEP100 PH domain and assayed for ARF6-GTP levels (**K**), and VEGFR2, ERK1/2, and MARCKS phosphorylation (**L**). $n \geq 3$; error bars represent s.e.m. *$P<0.05$, **$P<0.01$, ***$P<0.0001$. Quantifications of blots shown in panels A, C, D, F, G, I, J, K, and L are in Supplementary Figure 1.

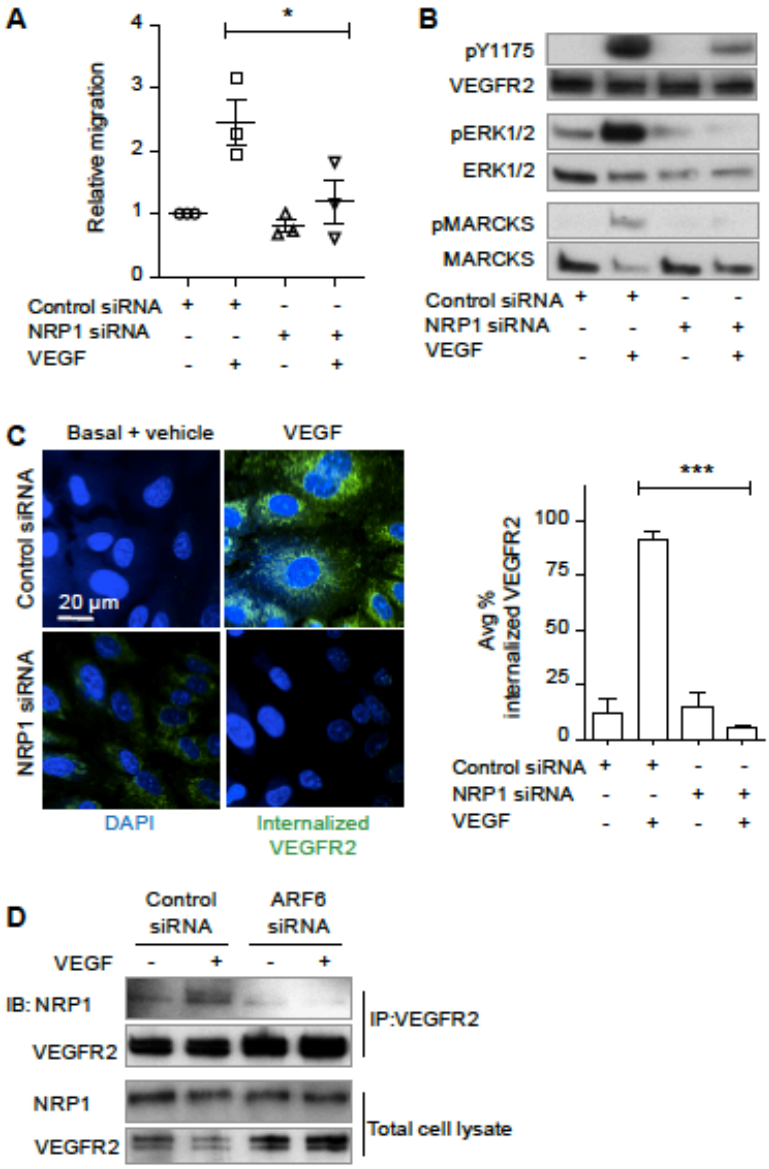

Fig. 4.2. VEGFR/NRP1 binding is ARF6 dependent and is necessary for internalization. (**A to C**) NRP1-siRNA-treated HRECs assayed for migration (**A**), VEGFR2, ERK1/2, and MARCKS phosphorylation (**B**), and internalized VEGFR2 (**C**). (**D**) VEGFR2 precipitation and NRP1 immunoblotting with control or ARF6 siRNA. $n \geq 3$; error bars represent s.e.m. *$P<0.05$, **$P<0.01$, ***$P<0.0001$. Quantifications of blots shown in panels B are in Supplementary Figure 2.

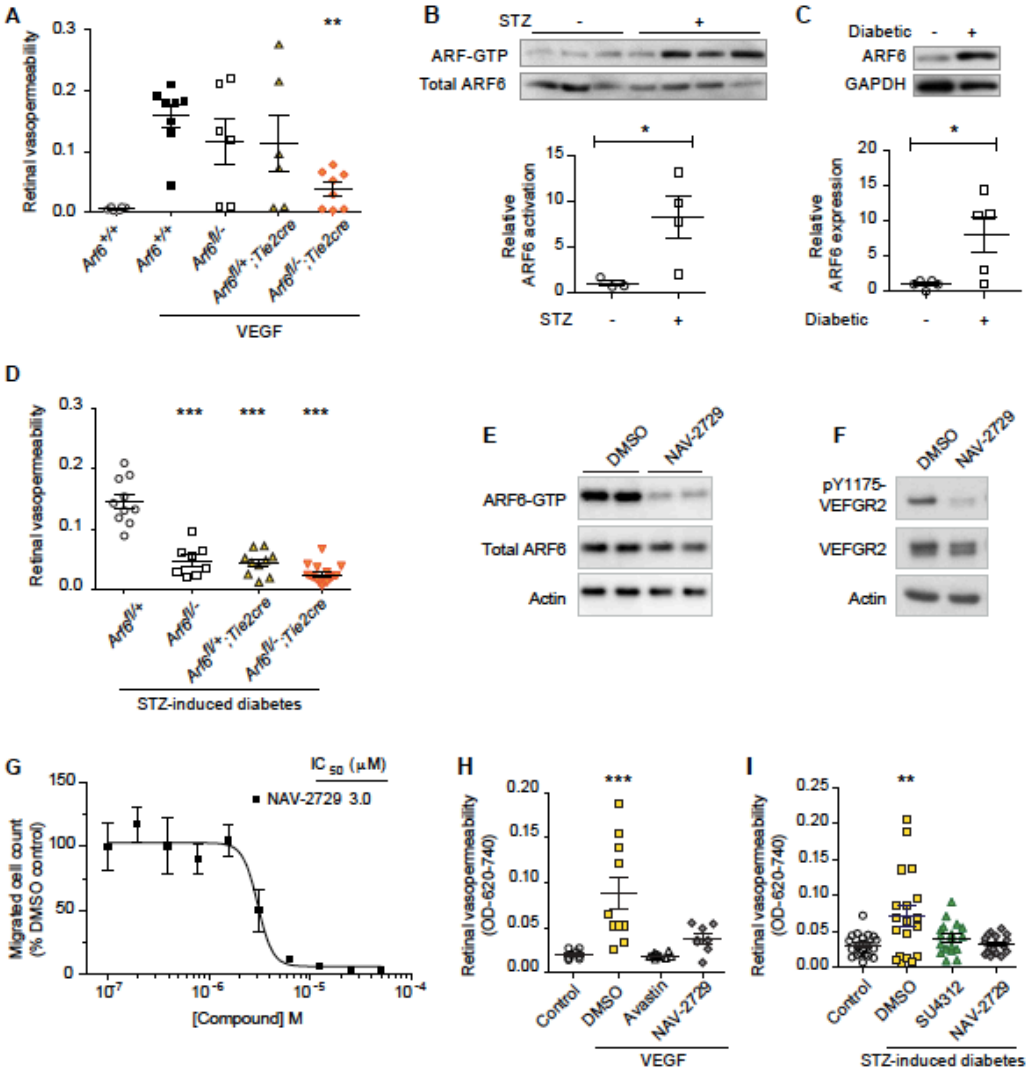

Fig. 4.3. Genetic and drug inhibition of ARF6 is protective against hyperpermability in diabetic retinopathy. (**A**) VEGF-induced retinal permeability in endothelial knockout mice compared to littermate controls. (**B**) Diabetic mouse eye lysates immunoblotted for ARF6 and ARF6-GTP. (**C**) Diabetic human eye lysates immunoblotted for ARF6. (**D**) STZ-induced diabetic permeability in endothelial knockout mice compared to littermate controls. (**E to G**) Effects of NAV-2729 on VEGF-induced ARF6-GTP levels in HRECs. (**E**), VEGFR2 phosphorylation (**F**), and migration of HRECs (**G**). (**H**) Intraocular VEGF-induced retinal permeability as assessed by Evans blue dye extravasation in mice treated with DMSO, SU4312, or NAV-2729. (**I**) STZ-induced diabetic permeability in mice treated with DMSO, SU4312, or NAV-2729. $n \geq 6$ animals; error bars represent s.e.m. *$P<0.05$, **$P<0.01$, ***$P<0.0001$ relative to control.

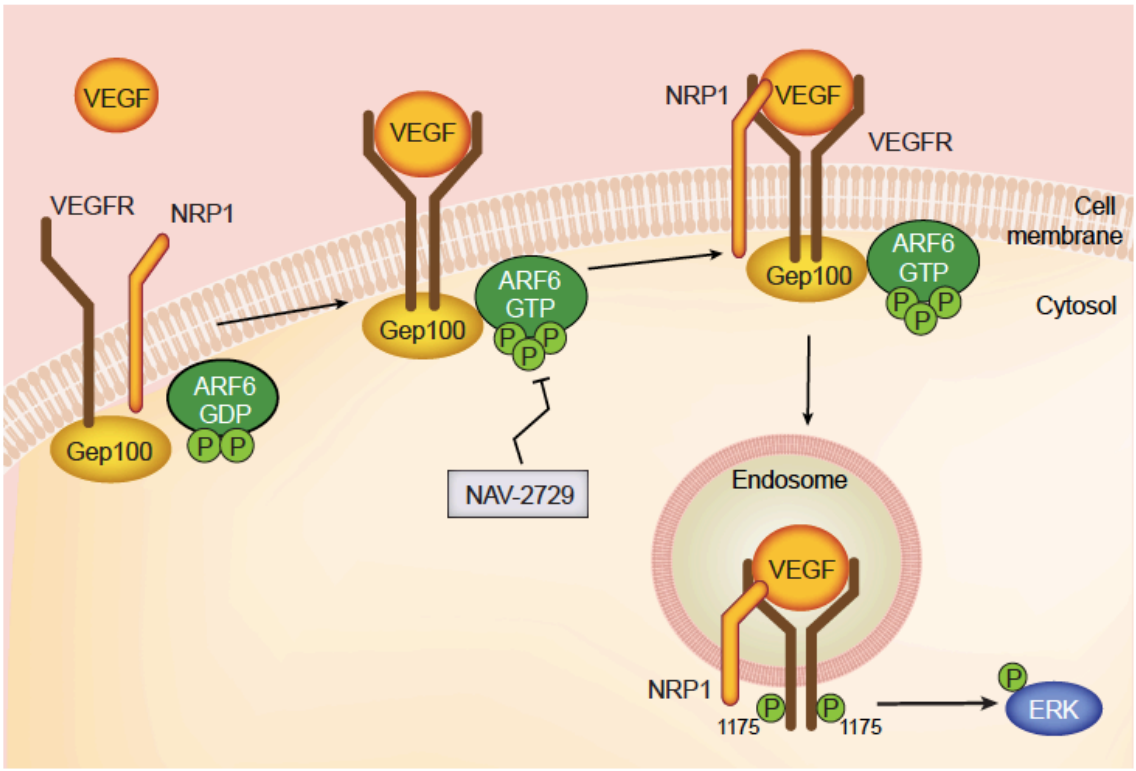

Fig. 4.4. Proposed model of the VEGF-NRP1-GEP100-ARF6 signaling pathway.

Supplementary Figures:

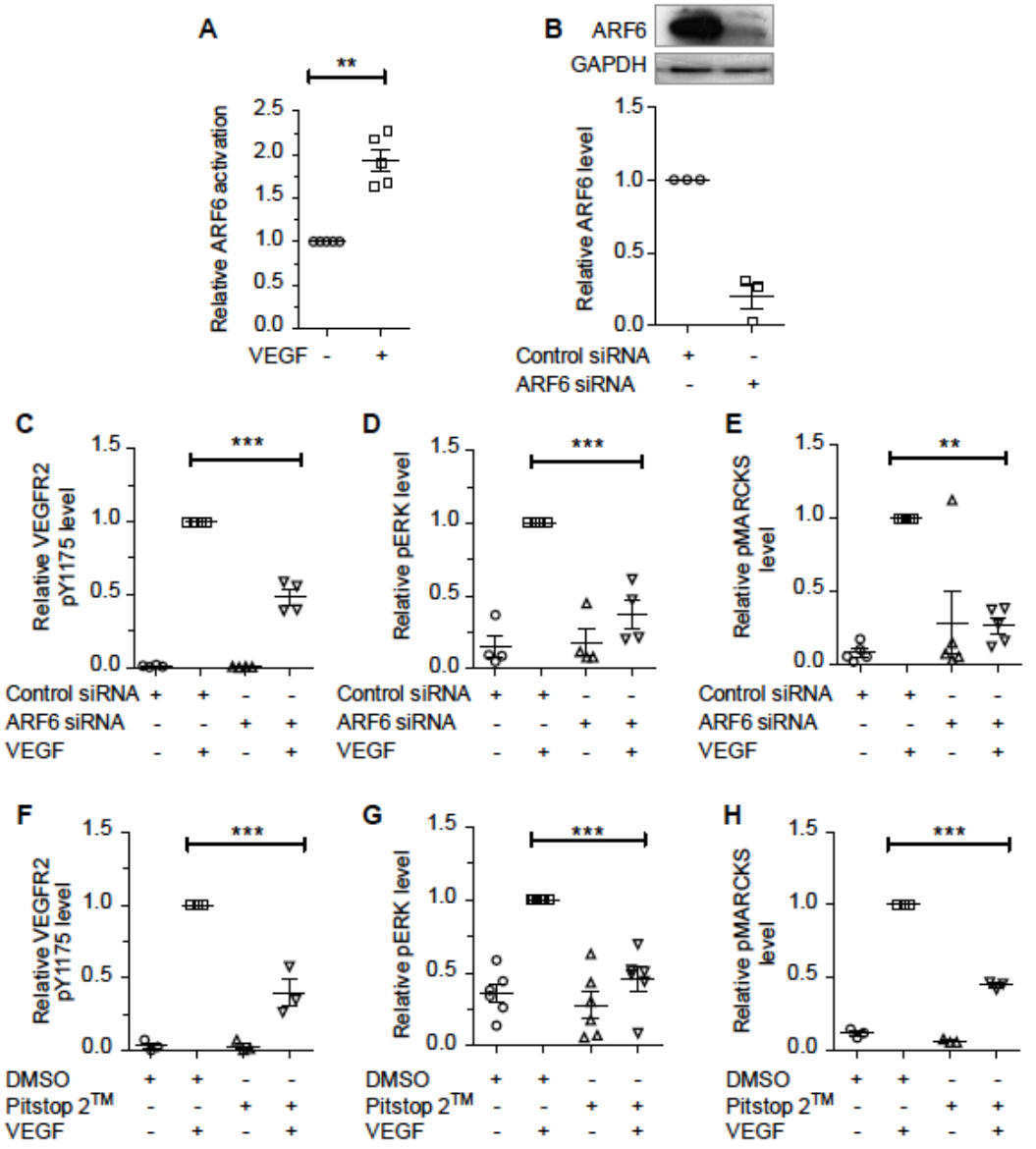

Fig. 4.S1. Supporting data and quantification of immunoblots in Fig. 1, A to E. (**A**) Quantification of ARF6-GTP levels in HRECs treated with VEGF. (**B**) Cell lysates from HRECs transfected with control siRNA or ARF6 siRNA immunoblotted with anti-ARF6 antibody to confirm knockdown. (**C to E**) Quantification of immunoblots represented in Fig. 1C. (**F to H**) Quantification of immunoblots represented in Fig. 1D.

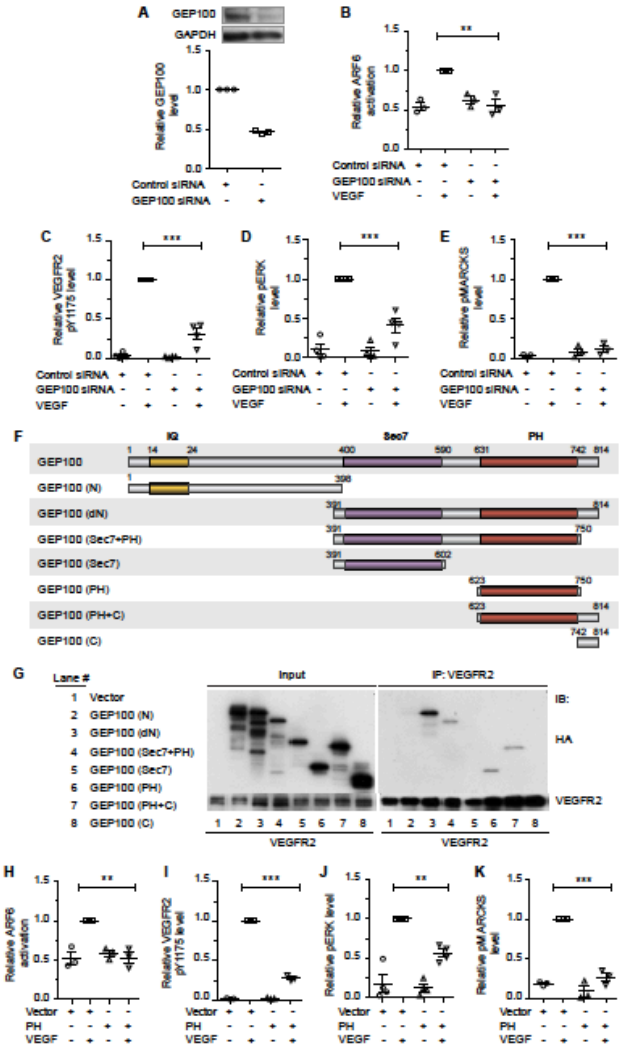

Fig. 4.S2. Supporting data and quantification of immunoblots in Fig. 1, F to L. (**A**) Cell lysates from HRECs transfected with control siRNA or GEP100 siRNA immunoblotted with anti-GEP100 antibody to confirm knockdown. (**B**) Quantification of immunoblots represented in Fig. 1F. (**C to E**) Quantification of immunoblots represented in Fig. 1I. (**F**) Schematic representation of GEP100 (full) and serial fragment constructs (N, dN, Sec7+PH, Sec7, PH, PH+C, C) *All GEP100 fragments* represent HA fusion (HA-tag) constructs containing the specified fragments of GEP100. (**G**) IP with anti-VEGFR2 antibody and immunoblotting with anti-VEGFR2 and anti-HA antibodies in HEK293T cells ectopically expressing each serial fragment of GEP100. (**H**) Quantifications of immunoblots represented in Fig. 1K. (**I to K**). Quantifications of immunoblots represented in Fig. 1L.

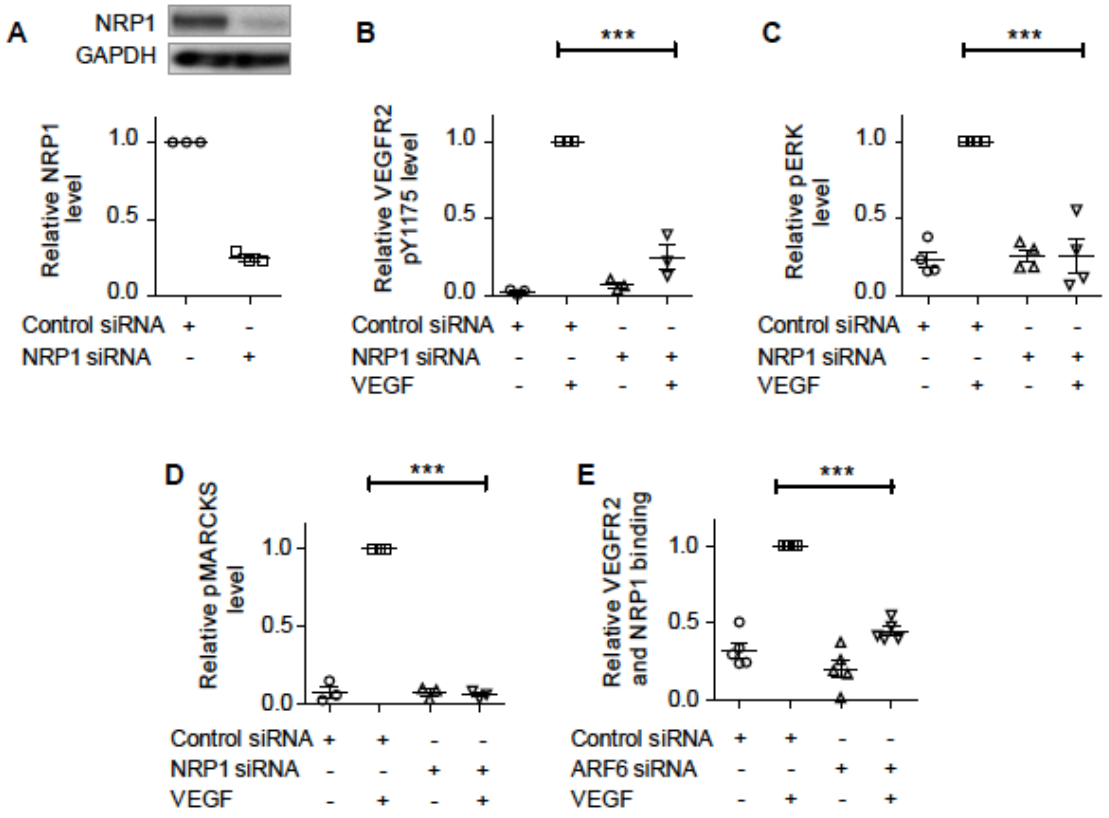

Fig. 4.S3. Supporting data and quantification of immunoblots in Fig. 2. (**A**) Cell lysates from HRECs transfected with control siRNA or NRP1 siRNA immunoblotted with anti-NRP1 antibody to confirm knockdown. (**B to E**) Quantification of immunoblots represented in Fig. 2B.

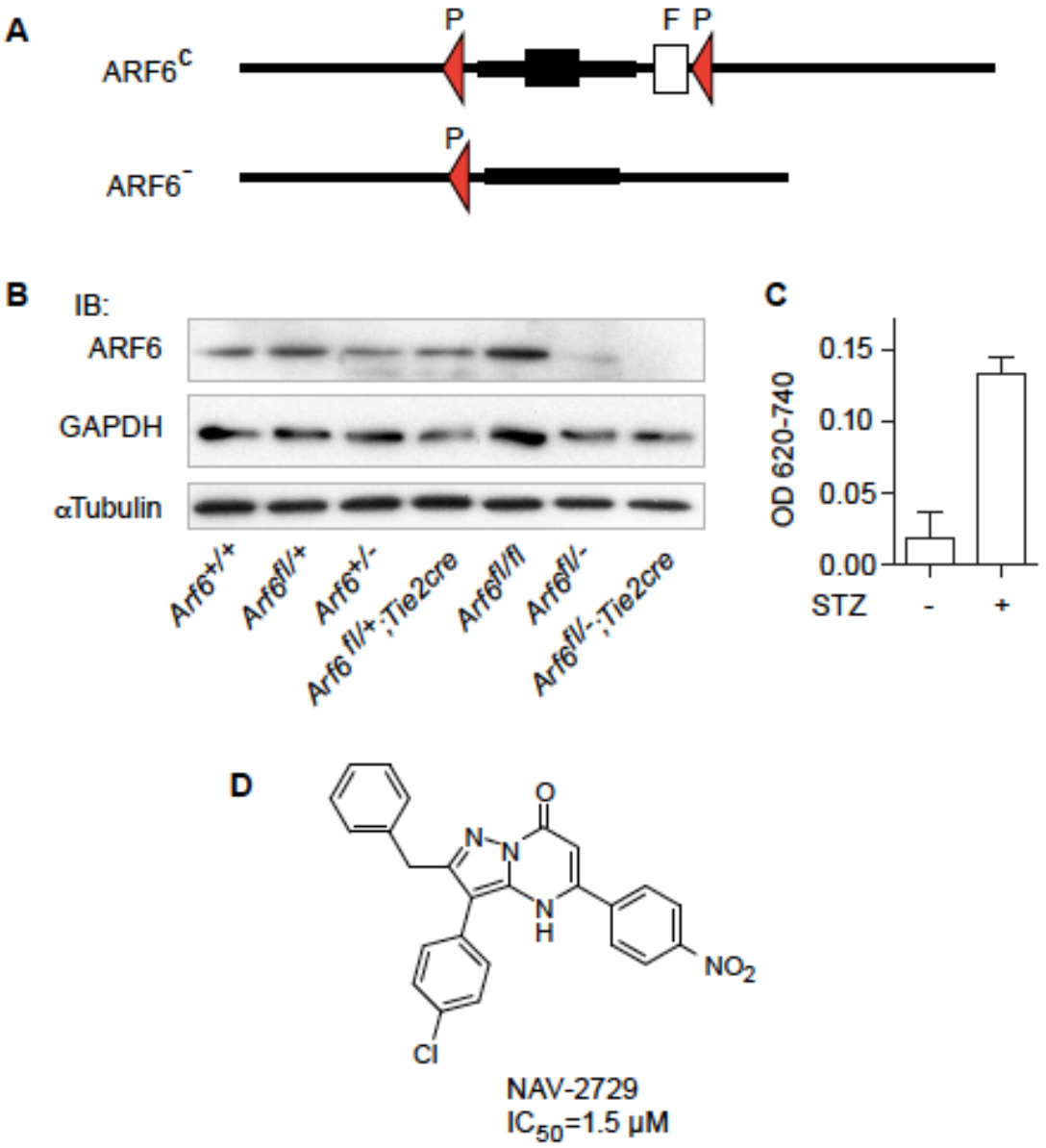

Fig. 4.S4. Generation and validation of ARF6 endothelial knockout mice. (**A**) Schematic of ARF6 knockout mice. (**B**) Validation of ARF6 knockout from lysates of aortic endothelial cells. (**C**) Evans blue permeability in mice treated with Saline or STZ. (**D**) Structure of NAV-2729

CHAPTER 5

CONCLUDING REMARKS

The findings presented in this dissertation add two major contributions. First is proof of principle that the proteasome is necessary for proplatelet formation. Loss or inhibition of the proteasome does not affect megakaryocyte maturation but does blunt platelet production to the extent that mice succumbed to multi-organ hemorrhage. Contrary to the prevailing hypothesis, the failure to form proplatelets under bortezomib treated conditions stems from over activation of RhoA signaling rather then an inhibition of NFκB[1,2]. This alters and adds to our understanding of what drives the final stages of megakaryocyte maturation and the beginning of proplatelet formation.

It is clear that platelets are important to the maintenance of the vascular endothelium and are crucial to inflammatory response[3,4]. However, it is not well understood how these platelets are formed. Though our findings solve the question of how one drug (bortezomib) causes thrombocytopenia, it leaves open the question of how megakaryocytes signal for their own morphogenesis into proplatelets and subsequently platelets[5]. By creating a mouse that has normal megakaryocyte maturation but impaired proplatelet formation (Psmc f/f; PF4cre), we have provided a useful tool for dissecting this latter question. To this extent, we have performed mass spectrometry using CLICK-IT to track the proteins generated in the final hours of megakaryocyte maturation.

Comparing proteasome knockout megakaryoctyes with WT, we have generated a list of potential proteins that may influence this crucial process. It is in this manner that we hope to begin to piece together the signaling pathways that are involved in thrombocytopoiesis.

The second contribution of this work is towards our understanding of signaling events downstream of proinflammatory and proangiogenic signals, specifically IL-1b and VEGF. Our work places the small GTPase, ARF6 as a rheostat in both signaling pathways, modulating endothelial cell permeability and signal amplification, respectively. Current medical therapies to prevent diseases of excessive cytokine signaling involve targeting one cytokine at a time. Though effective, this is often inefficient. Our increasing understanding of ARF6 as a modulator of multiple inflammatory signaling pathways may provide a unified way of muting all inflammatory pathways.

Though we uncovered that ARF6 may be involved in VEGFR2 endocytosis and signal amplification, the exact mechanism still needs to be elucidated. It is unclear at which endosomal compartments signal amplifications occur and how ARF6 regulates the temporal and spatial relationships of VEGFR2, NRP1, and VE-Cadherin. Future work using specific inhibitors at different VEGFR2 phosphorylation sites in the presence and absence of ARF6 knockdown may solve some of these questions. In addition, staining for these membrane proteins in conjunction with Rab5, Rab7, and Rab 11 markers may also help to better define the role of ARF6. Work on the role of ARF6 in VEGF signaling is ongoing.

References

1. Lonial, S.*, et al.* Risk factors and kinetics of thrombocytopenia associated with bortezomib for relapsed, refractory multiple myeloma. *Blood* **106**, 3777-3784 (2005).

2. McConkey, D.J. Bortezomib paradigm shift in myeloma. *Blood* **114**, 931-932 (2009).

3. von Hundelshausen, P. & Weber, C. Platelets as immune cells: bridging inflammation and cardiovascular disease. *Circulation research* **100**, 27-40 (2007).

4. Morrell, C.N., Aggrey, A.A., Chapman, L.M. & Modjeski, K.L. Emerging roles for platelets as immune and inflammatory cells. *Blood* **123**, 2759-2767 (2014).

5. Machlus, K.R. & Italiano, J.E., Jr. The incredible journey: From megakaryocyte development to platelet formation. *The Journal of cell biology* **201**, 785-796 (2013).